University of Cincinnati

Date: 7/10/2024

I, Mohammad Saleem, hereby submit this original work as part of the requirements for the degree of Doctor of Philosophy in Aerospace Engineering.

It is entitled:

Hydrodynamic and Acoustic Waves from Vortex Generators Noise Reduction for Supersonic Jets

Student's name: **Mohammad Saleem**

This work and its defense approved by:

Committee chair: Ephraim Gutmark, Ph.D.

Committee member: Paul Orkwis, Ph.D.

Committee member: Shaaban Abdallah, Ph.D.

Committee member: Junhui Liu, Ph.D.

48261

Hydrodynamic and Acoustic Waves from Vortex Generators

Noise Reduction for Supersonic Jets

by

Mohammad Saleem, B.S., M.S.

Dissertation

Presented to the Faculty of the Graduate School of The University of Cincinnati in Partial Fulfillment of the Requirements for the Degree of

Doctor of Philosophy in Aerospace Engineering & Engineering Mechanics

Dissertation Committee

Dr. Ephraim Gutmark, (Advisor/ Chair)

Dr. Paul Orkwis

Dr. Shaaban Abdallah

Dr. Junhui Liu

University of Cincinnati

August 2024

Abstract

Hydrodynamic and Acoustic Waves from Vortex Generators Noise Reduction for Supersonic Jets

Mohammad Saleem, PhD

University of Cincinnati, 2024

PhD Advisor & Committee Chair: Ephraim Gutmark / B.S., M.S., PhD

An experimental investigation into the wave sources responsible for the noise generation mechanisms of supersonic jet noise and their mitigation using MVG nozzles is presented. Flow field measurements using PIV revealed that MVGs mitigate noise through two mechanisms; they generate internal oblique shock waves that weakens the shock cell, and they substantially increase the shear layer mixing and its entrainment of ambient fluid which reduces the length scales and velocities of the convecting coherent structures. In addition, time-resolved Schlieren visualizations were spectrally analyzed to decompose and reconstruct the hydrodynamic waves in the flow field and the generation process of the acoustic wave emission directly from the jet providing insights into the noise generation mechanism and their suppression by inducing the peak wave instabilities to shift to larger wavenumber values to reduce their acoustic emission efficiencies, which were confirmed by acoustic measurements. The findings from this investigation show direct visualization of the acoustic wave emission from the sources in the flow field. These waves have downstream components that are emitted from the modulation of the shear layer inducing spatial coherence of the turbulent vortical structures. This modulation is induced by the passing of the upstream acoustic waves along the shear layer from all shock cells synchronized as a phased array with regions of constructive and destructive interference patterns which steers the emitted acoustic radiation beams. The intense acoustic beam perturbs the shear layer and induces the formation of the internal trapped waves with phase velocities propagating upstream of the supersonic jet flow. Based on these findings, new noise generation mechanisms are proposed that cover various aspects of the physical mechanisms of jet noise components for the turbulent mixing noise, the broadband shock associated noise and the screech resonance tone, along with reduction and suppression mechanisms.

This work, effort, and time is dedicated to God. And I ask for his blessings to be bestowed upon my parents for everything they have done for me and for their efforts, upon my wife and children, upon my teachers and professors whom sparked in me the love for science, upon my family, and upon me. Praises and thanks be to God, and prayers and peace be upon his Messenger and family.

Acknowledgment

I would like to thank my professor and adviser Dr. Ephraim Gutmark for giving me the opportunity to work on this project and in his lab. His guidance throughout my time as a graduate student for over six years has allowed me to grow as a researcher, and I appreciate the commitment he has shown to me. I am grateful and it has been an honor to work with and learn from one of the biggest names in the field, a world-renowned researcher, a distinguished professor, and an Ohio eminent scholar. I would also like to extend my gratitude to my dissertation defense committee; Dr. Paul Orkwis, Dr. Shaaban Abdallah, and Dr. Junhui Liu. I would especially like to thank Dr. Junhui Liu for the many discussions and guidance while working on the SERDP and ONR collaboration between the NRL and UC on this project.

I appreciate the camaraderie of the members of the GDPL throughout my tenure in the lab. I would like to thank our senior research associates; Russel Dimicco, and Curtis Fox for the mentoring regarding design, test rig setup, and execution of experiments. Their help in building and maintaining our facilities has enabled my research and allowed me to continue making progress. Thanks to Dr. Daniel Cuppoletti, Dr. Rodrigo Villalva, and Dr. Charles de Luzan for the enlightening discussions and guidance on experiments and measurement techniques. I would also like to thank the countless others whom I have worked with over the years. Thanks to my fellow graduate students Omar Lopez, Aatresh Karnam, Mohammad Arshad, Kaurab Gautam, Vincent Onoja, James Cramer, Kranthi Yellugari, Mohammed Gulam, Yuvi Nanda, Shyam Muralidharan, Rachel Wiggins, Tyler Pritschau, and many others.

Finally, I would like to thank my family for all of the support and encouragement throughout this process, especially both of my parents, for instilling in me the joy of learning at an early age. And I would like to acknowledge my sincere debt to my wife and children, without them I couldn't have made it to this point.   Above all, praises and thanks to God at the beginning and at the end.

Table of Contents

List of Tables

List of Figures

Chapter 1: Introduction and Background

RESEARCH MOTIVATION

Supersonic jet noise has adverse health effects on personnel working in the vicinity of high-performance aircrafts, especially on crew members on aircraft carrier decks. Also, another health hazard is community noise in residential zones near air bases. For crew members exposed to supersonic jet noise, the health impact can lead to hearing loss even with the use of hearing protective gear. Lawsuits and hearing disability claims cost the DOD over $4.2 Billion[1]. With the ever-increasing need for more powerful engines for newer generation high-performance aircrafts, the problem of supersonic jet noise become even worse. Thus, there is an urgent need to develop new effective noise-reduction technologies for supersonic jets.

There have been numerous research conducted on jet noise reduction and new technologies have emerged but with limited noise reduction gains especially at takeoff conditions. This is because most of the noise reduction devices are generally implemented at the edge of the nozzle exit which have limited interaction with the nozzle flow due to the flow separating from the nozzle wall at overexpanded operating conditions, where the flow bypasses these devices rendering them ineffective [2]. Such devices include tabs[2] and chevrons [3–5].

Vortex generators placed inside the nozzle have the advantage of avoiding the flow separation region near the nozzle exit and can maintain strong interaction with the nozzle flow. This leads to a more effective generation of streamwise counter-rotating vortices responsible for shear layer mixing and dissipation leading to reduced turbulent mixing noise and is similar to the vortices mixing mechanisms observed in chevron [3,6,7]. Vortex generators placed inside the supersonic nozzle flow generate internal oblique shock waves that interact with shocks in the jet plume[8,9], and can lead to reductions of shock noise components of these jets [10]. An additional advantage of vortex generators is that their design space has more parameters than other devices which allows for more effective design optimization efforts.

Since the development of new noise reduction technologies requires an extensive parametric study to assess their noise reduction gains, the experimental development stage would take many years due to the slow turnaround time for incremental performance gains. This is rooted in the development method being an inverse problem where the changes in design parameters are assessed by the acoustic noise performance in a trial-and-error method before committing to in depth experimental campaigns to study all aspects of the flow field, and the acoustic fields. A more robust design approach can be adopted for rapid performance evaluation of varying the parameter space of these devices by simultaneously probing the flow field and the emitted acoustic field using high-speed Schlieren visualizations where the flow fluctuations and the acoustic waves are captured in every imaging frame and can be analyzed using spectral methods to study the noise generation mechanism at the source and their modifications. In this way the noise reduction performance of these devices and their acoustic wave emissions are firstly evaluated at the flow sources rather than at the receiving far-field microphones and can influence the design process by targeting specific flow modifications to produce the desired acoustic wave emissions that eventually propagate as jet noise into the microphones at the acoustic far-field. In addition, this approach allows for the investigation of the noise generation mechanisms and uncover new physical mechanisms which are enabled by the new experimental measurements and data processing techniques.

SUPERSONIC JET FLOW

A jet flow is driven by a pressure gradient across the nozzle and is typically defined by the ratio of nozzle plenum stagnation pressure to the ambient pressure called the Nozzle Pressure Ratio (NPR). As the NPR increases above a critical value, the jet flow turns sonic at the exit plane for converging nozzles. However, for converging diverging (C-D) nozzles, as the flow passes past the nozzle throat, the flow is expanded in the diverging nozzle section and accelerates to supersonic velocities which values depend on the level of nozzle flow expansion. After that the flow exits the nozzle into the ambient and depending on the NPR values the flow can shocked and turn back to subsonic, or for large enough NPRs the level of expansion can be overexpanded, perfectly expanded, or underexpanded. The current study is concerned about the overexpanded flow conditions as they are related to takeoff operating conditions. As the flow of an overexpanded jet issues into the ambient the pressure at the nozzle exit plane is lower than the ambient pressure, hence a shock wave is formed to allow the flow to adjust to the ambient pressure. The strength of the formed shock waves depends on the pressure jump and can induce a strong normal shock in the form of a Mach disk or a weaker oblique shock wave. The Mach disk forms a triple point as it intersects with the oblique shock from the nozzle lip and a slipstream is generated at the triple point. Either of these shock waves are initiated at the nozzle lip causing the jet flow to turn radially inwards to the jet centerline, and then the flow corrects itself in a successive fashion radially outwards and inwards through a system of expansion fans and shock waves, respectively. As the generated oblique shocks reach the shear layer they reflect as expansion fan that propagate to the opposite shear layer, and the expansion fan reflects off the shear layer as compression waves that coalesce to form shock waves. This pattern keeps repeating and gives rise to the formation of shock cell structures in the supersonic jet core, where the flow keeps adjusting itself until it approaches pressure equilibrium. The system of shock waves and expansion fan are bounded by the sonic line, which demarks flow regions with local velocity equals the local speed of sound. As the flow travels to the downstream, the shock cell radial size decreases due to mixing and viscous dissipation from the shear layer, and eventually the flow reaches the end of the supersonic core and the shock cells terminate.

The jet exhibits many flow features which are shown in Figure 1.1. As the flow exits the nozzle into the ambient air, a mixing shear layer develops around the periphery of the jet and is driven by the velocity gradient between the jet flow in the inner shear layer and the almost stagnant ambient air on the outer shear layer across the shear layer thickness. This shear layer thickness grows in the downstream direction in both inward and outward radial directions. This growth continues until both upper and lower shear layers merge at the end of the irrotational jet core, this region is known as the initial mixing layer. The turbulence and viscous stresses of the merged shear layer mix with the jet core causing dissipation and reduction in jet centerline velocity as the flow transitions into a turbulent flow, this region is known as the transition zone. Beyond that, the jet flow becomes fully turbulent, and its energy dissipates. In this region the jet becomes self-similar and is denoted as a fully developed region. In supersonic jets, a shock cell system is present in the jet core due to non-ideal flow expansion. The shocks extend beyond the potential core and are maintained in the supersonic flow regions bordered by the sonic line.

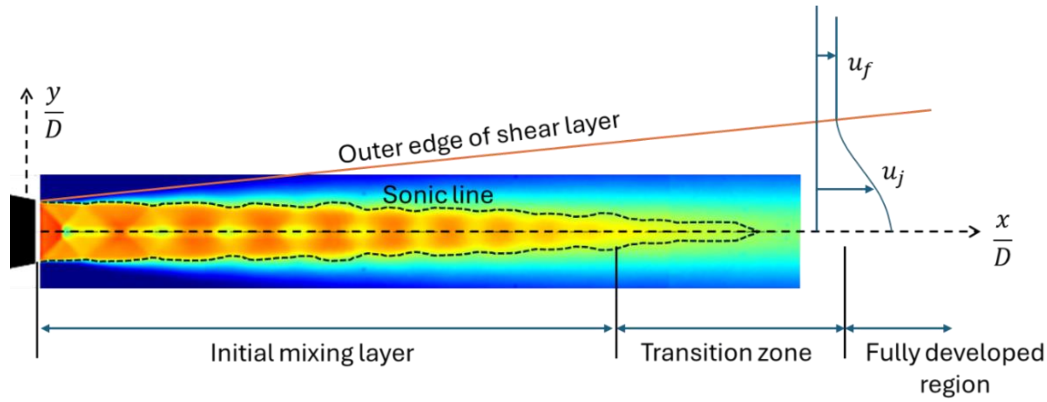

Figure 1.1: Example of supersonic jet showing plume features and mixing zones.

JET SHEAR LAYER INSTABILITIES

Free shear layers are mixing zones between two fluid streams of different densities or velocities. Due to Bernoulli's effect, the interface between the two streams is perturbed with pressure variation that triggers Kelvin-Helmholtz (K-H) instability. This instability tends to grow and amplify with a preferential mode frequency. As these instabilities grow, they perturb the shear layer and lead to roll-up to form vortical structures that convect along the mixing layer[11]. Winant and Browand[12] showed that the growth of the convecting coherent structures were due to vortex pairing inducing entrainment and leading to shear layer growth. The energy of the coherent vortical structures is linked to the momentum of the structures and is a function of the convection velocity and convective Mach number in compressible flows. Papamoschou[13] studied compressible mixing layer and formulated an equation for the convective Mach number as:

$$M_c = \frac{u_c}{c_\infty} = \frac{u_j}{c_j + c_\infty}$$

Where; u_c: is the convective velocity, u_j: is the jet velocity, c_j: is the speed of sound in the jet, and c_∞: is the ambient speed of sound. These parameters influence the growth mechanism of the compressible coherent structures and entrainment and are schematically shown in Figure 1.2.

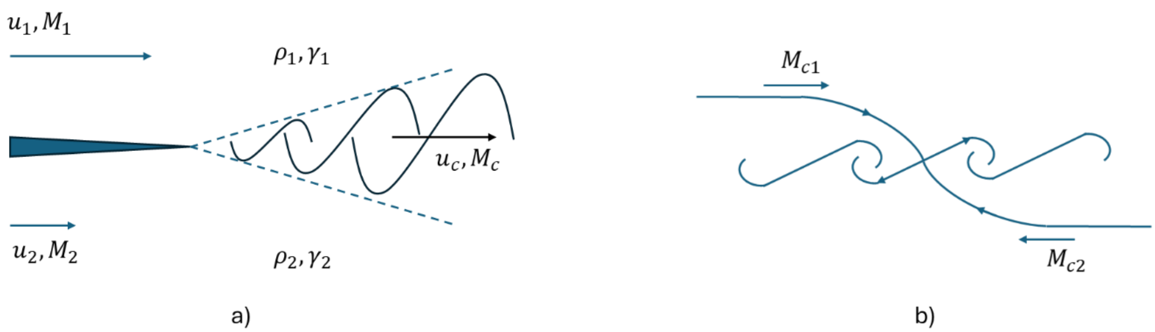

Figure 1.2: Development of coherent structures in mixing layer showing, a) parameters influencing growth rate, and b) streamlines of entrainment driving growth rate.

Jet flows also have a mixing layer that is axisymmetric around the jet axis, and the formation of coherent vortical structures in shear layers are similar to those of two-dimensional mixing layers and they form in both subsonic and supersonic jet flows. Yu, Gutmark, and Shadow[14] observed coherent structures in a supersonic jet and showed that the turbulence coherence of the convecting structures was influenced by the lip thickness wake region and the convective Mach number of the shear flow. Thurow et al.[15] showed than in supersonic jets, the coherent structures undergo a tilt-stretch-tear-pair mechanism, which contributes to the intense noise radiation of large scale turbulent mixing noise.

The convective turbulent coherent structures play an essential role in the generation mechanism of supersonic jet noise. They give rise to the large scale-mixing noise, as well as the generation of screech and BBSAN that result from the interaction of the turbulent structures with the shock cells in imperfectly expanded supersonic jets[16].

SUPERSONIC JET NOISE COMPONENTS

The different flow features present in the supersonic jet give rise to the various acoustic jet noise components and are categorized into three main groups[16]; the turbulent mixing noise[17], the Broadband Shock Associated Noise (BBSAN)[18], and for resonating jets a screech tone peak [19,20]. Both BBSAN and screech are considered shock noise, and they are produced in imperfectly expanded supersonic jets that contain a quasiperiodic shock cell structure, which interacts with the convective turbulent structures to produce shock noise. The various jet noise components can be observed in far-field microphone measurements. The Figure 1.3 shows an example of acoustic spectra for shock containing jets, the spectra indicates the spectral energy in sound pressure level SPL as a function of frequency. Where, the turbulent mixing noise have a low frequency component with high amplitude, and the BBSAN show a wider peak with high intensity levels at higher frequencies[16]. In addition, the screech forms a prominent peak at a single frequency to the left of BBSAN. When the jet undergoes intense screech, higher screech harmonics can be observed in the spectra. Noise intensities can be reduced using noise reduction devices, which can target various noise components of the acoustic spectra as seen in the green curve.

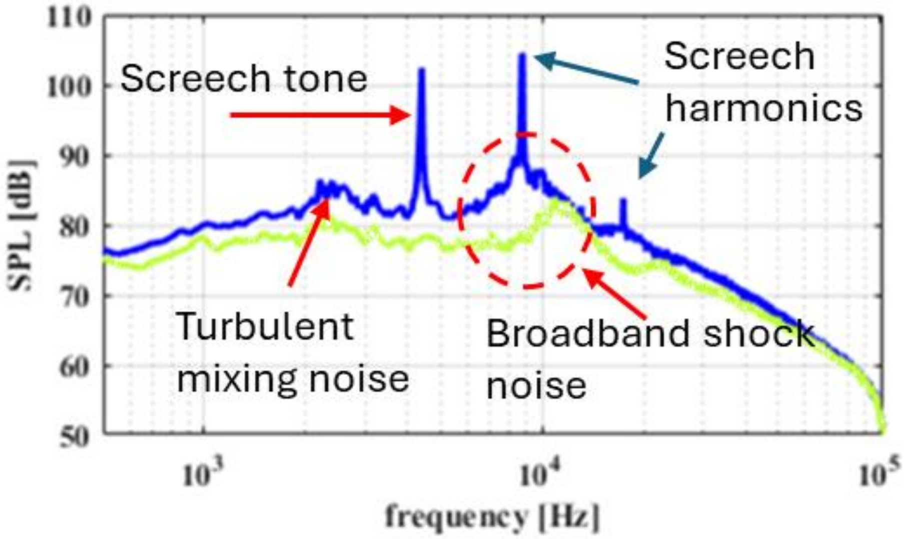

Figure 1.3: Examples of Far-field Sound Pressure Level (SPL) spectra of shock containing supersonic jets for a sideline observer.

Turbulent mixing noise

The turbulent mixing noise consists of both large-scale turbulence mixing noise and fine-scale turbulence mixing noise. The former is generated by large turbulent structures convecting along the shear layer resulting from the shear layer mixing with the ambient air, and the latter is generated by the dissipation of the small turbulent structures in the shear layer and flow (Tam[21]).

The acoustic radiation directivity of the fine-scale turbulence mixing noise is present in all observation angles making it a background turbulence noise. However, the large-scale turbulence mixing noise presents higher noise levels and dominates the downstream observation angles (Seiner[22]). In supersonic jets the dominant turbulent mixing noise component is generated from the large-scale turbulent structures which can grow into larger coherent structures.

The turbulent mixing noise is mainly due to the growth of shear layer instability that is driven by Kelvin-Helmholtz (K-H) instabilities. These instabilities grow along the shear layer causing the formation of conveting turbulent structures and vortices and can lead to the formation of internal waves inside the supersonic jet. The generation of the internal waves were studied experimentally by Oertel[23], and Mathematically modeled by Tam[24] using vortex sheet model where they showed upstream internal wave propagation can be sustained in supersonic jets. Additionally, the formation and growth of the coherent structures were found to depend on the convective Mach number, and the nozzle lip wake region[25]. The formed convecting structures caused the formation of intense acoustic waves that propagated primarily in the downstream direction and were observed as wave packets[26–29]. The strength of the generated acoustics depended also on the size and growth of the convecting structures[30–34], these growth mechanisms are due to "collective interaction[35]" where shear layer forcing causes the smaller vortices to merge and form larger vortices and can interact with vortices from the other side of the shear layer at the collapsing end of the potential core emitting intense mixing noise.

In addition, the turbulent mixing noise from the convecting structures emit noise radiation with downstream directivity as seen in the example in Figure 1.4. Tam[24] modeled these structures as instability waves with supersonic phase velocities propagating in the downstream direction and used a wavy wall analogy to explain its acoustic radiation using Mach wave radiation schematically shown in Figure 1.5. The radiation angle is found using the Mach angle relation. This emission produces a single radiation angle for a given frequency, and for a fixed amplitude wave it has only one wavenumber value. However, for the turbulent convecting structures, their amplification grows in the downstream direction until it reaches a peak and then dissipates. This growth and decay of the turbulent structures was applied to the wavy wall analogy by Tam and Burton [36,37]. This varying wave will have a broadband spectra of wavenumbers, with a range of both subsonic and supersonic wave propagation speed even when the convecting structures are subsonic, hence they produce a range of waves having various radiation angles that are predominantly directed to the downstream direction. However, since the Mach wave radiation is driven by supersonic phase velocities of the instability waves, the acoustic radiation efficiency is reduced with reduction in phase velocities and vanishes when they turn into subsonic phase velocities. In addition, the turbulent structures not only have a single oscillation frequency, but rather a broad range of frequencies, all of which emit their noise radiation with varying frequencies and intensities.

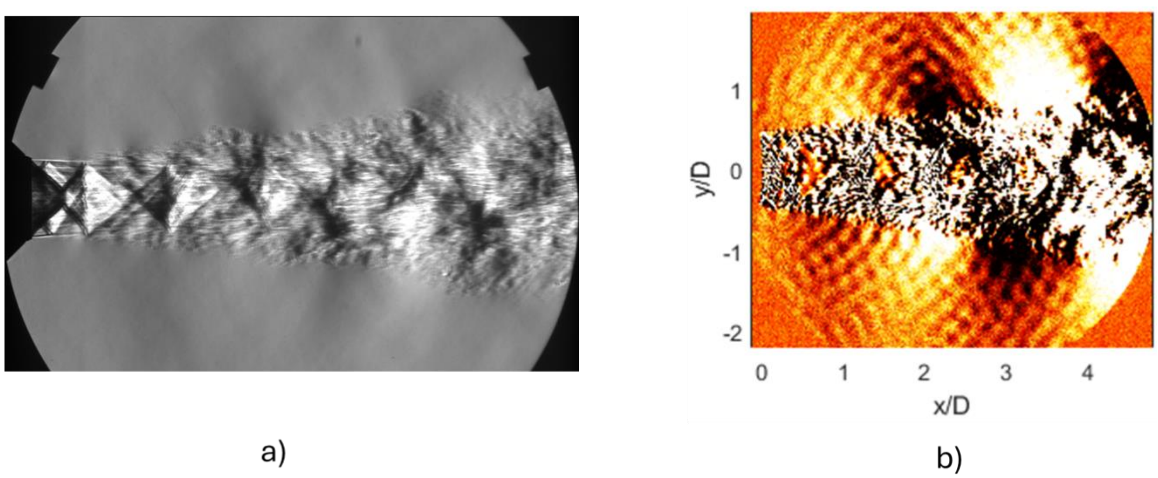

Figure 1.4: Examples of low frequency mixing noise emissions from convecting coherent structures in a supersonic jet, a) Schlieren visualization of flow filed, b) low frequency SPOD Schlieren.

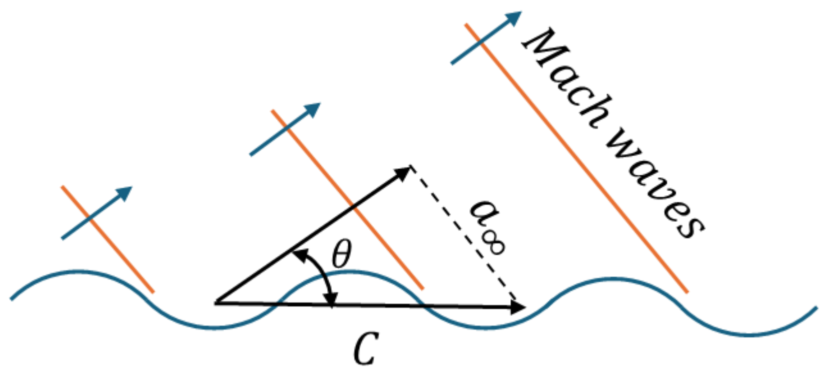

Figure 1.5: Schematic of Mach wave radiation emissions from a wavy wall traveling at supersonic phase velocity C.

Screech

In addition to mixing noise, imperfectly expanded supersonic jets produce shock noise[38–40]. Where imperfectly expanded jets will form shock cells in the jet plume consisting of shock waves and expansion waves that interact with the shear layer turbulent and coherent structures. These interactions lead to the rise of shock noise consisting of a discrete frequency peak known as jet screech and a broader frequency high-intensity component known as Broad Band Shock Associated Noise (BBSAN)[41]. The seminal work of Powel[19] identified screech as a jet resonance phenomenon that was sustained by an acoustic feedback loop, and attributed its generation mechanism to downstream convecting shear layer disturbances that grow large enough to interact with downstream shock cells that triggers a strong acoustic wave emission. This acoustic wave travels back to the nozzle exit, and further perturbs the sensitive thin shear layer near the nozzle exit, thus closing the feedback loop. He developed a prediction model for the screech frequency based on the assumption that the shock tips were equally spaced monopole sources. His model was based on the observations that the screech frequency varied with the shock cell spacing which is a function of the operating condition. Changes in the operating conditions cause changes in the jet velocity and its convective velocity of the turbulent structures traveling along the shear layer. He modeled screech acoustic sources as monopoles equally spaced at the shock cell tips intersection with the shear layer and formulated a screech frequency prediction model as:

$$f = \frac{U_c}{L_s(1 + M_c)}$$

where f is the frequency, L_s is the shock cell spacing, U_c and M_c are the convective velocity and Mach number, respectively.

However, Powell's screech prediction model has its limitation, as it does not account for sudden changes in the screech tone frequency when the operating condition is changed slowly, this change is known as staging. An important development in screech research was from the experimental studies of Panda[42–44], where he identified the existence of standing wave patterns in screeching jets and found that they are formed by superposition of downstream hydrodynamic shear layer instability and upstream propagating acoustic waves, and suggested that an accurate length scale for screech prediction was the spacing of standing waves instead of the shock cell spacing thus modifying the screech prediction model to be:

$$f = \frac{U_c}{\lambda_{sw}(1 + M_c)}$$

where λ_{sw} is the wavelength of the standing wave. Such standing wave patterns can be observed in Schlieren visualizations of screeching jets, an example is shown in Figure 1.6.

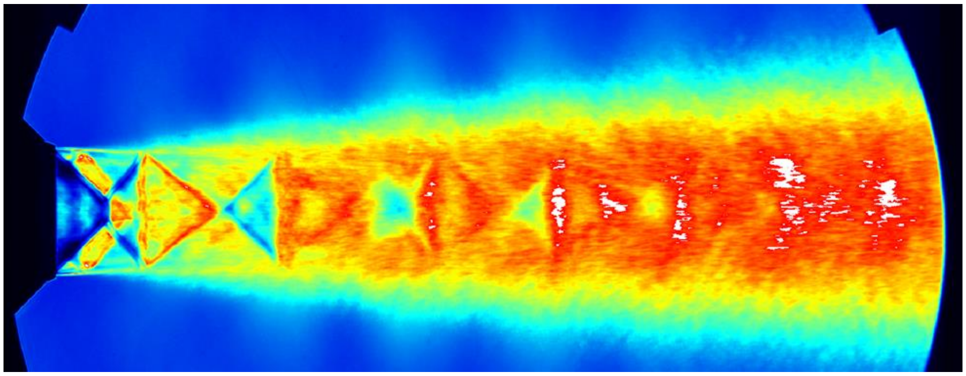

Figure 1.6: Example of standard deviation of Schlieren imaging showing the shear layer undulations and the accompanying standing wave pattern for a screeching jet.

The work on screech was further extended by various researchers[20,45,46]. Tam[24,40] mathematically modeled the shear layer as vortex sheet interacting with shock cells and identified an internal upstream propagating waves Guided Jet Mode G-JM[47–49]. These internal waves were confirmed numerically[50] and experimentally[46,51,52]. The discovery of these internal trapped waves and G-JM showed that it can also be a mechanism for closing the screech feedback loop and was able to explain screech staging.

Trapped internal waves are observed in high subsonic and supersonic jets which exhibit a system of instability waves that propagate internally inside the jet in both upstream and downstream directions. These waves have been found to influence the pressure fluctuations outside the jet that generate acoustic noise. These internal trapped waves were also identified to drive jet flow resonance. Some of the earlier studies showing the existence of the various wave systems are those conducted by Oertel [53–55], where different types of waves are formed including Mach wave radiation, Kelvin-Helmholtz type instability, and internal trapped wave instability. Tam and Hu [24], analytically studied these trapped waves' internal instabilities of the jet and found that their phase have subsonic propagation speeds within supersonic jets.

These internal trapped waves have gained increased attention recently. Schmidt et al.[28] showed that the interaction of upstream and downstream propagation of the trapped waves causes a resonance of pressure fluctuations with distinct peaks and these peaks were also found in the near acoustic region of the jets. Zaman et al.[56] conducted near-field microphone pressure measurements and also showed that indeed the acoustic fluctuations are related to the trapped waves. In that study, the influence of the internal trapped waves was found to have an imprint on the acoustic spectral content in the jet vicinity that decays as the measurement point moves radially away from the jet.

The screech noise generation mechanism was investigated by a series of numerical studies by Maning & Lele[57] Suzuki & Lele[50], and they identified a shock-vortex interaction that they proposed as a "shock leakage" mechanism which is due to the interaction of the shear layer vortices with the tip of the shock cells. They conducted Direct Numerical Simulations (DNS) on a model problem that includes an impinging shock wave simulated as a compression wave on a forced mixing layer that produced organized convecting vortical structures. They found that the interaction of the convecting vortical structures interacted with the shock tip and generated acoustic emissions in the shock leakage mechanism. This mechanism was also observed experimentally by Edgington-Mitchell[51].

Broadband shock associated noise

The Broadband shock-associated noise (BBSAN) is generated from the interaction of the turbulence in the shear layer with the shock cell structures in the jet flow. This noise component produces high noise intensities in the upstream observation angles and gradually decreases in the downstream observation direction.

Harper-Bourne and Fisher[41] first proposed that the BBSAN noise generation was due to the interaction of the shear layer turbulent structures with the shock cell tips and modeled the shock tips as source locations, however, their model had some limitations. Tam & Tannah[40] suggested that BBSAN generation was due to the weak interaction between the large-scale structures and the shock cells and they developed a stochastic model for its noise prediction. Additionally, Tam[16] showed a model for BBSAN noise generation mechanism, based on the weak interaction model, the shear layer disturbance is modeled as the real part of a traveling wave

$$u_t = Re\left[Ae^{i(kx-\omega t)}\right]$$

where u_t is the turbulence convection velocity, A is a Fourier mode amplitude, k is the wavenumber, ω is the radial frequency, x and t are the space and time variables. The shock cell disturbances were also modeled as a wave fluctuation

$$u_s = \frac{B}{2}\left(e^{ikx} + e^{-ikx}\right)$$

And showed that due to the wavy wall analogy the interaction of these two wave models they produced sound wave radiation and derived a peak frequency prediction equation as a function of observation angle

$$f = \frac{u_c}{L_i\left(1 + u_c \cos\left(\frac{\theta}{a_\infty}\right)\right)}$$

This equation models the BBSAN radiation directivity of the various BBSAN frequency content. The BBSAN directivity can be observed in the far-field SPL spectra as shown in is shown in Figure 1.7, where the peak BBSAN high intensity hump shifts to higher frequencies for downstream observation angles.

Later on, Lele[58] demonstrated that the phase coherence of the turbulent structures was necessary to improve prediction accuracy as the phase delay between the interactions of successive shock cells can lead to constructive or destructive interference and impact the generated noise intensity and directivity. However, it is not well understood how turbulent coherence is maintained along large axial distances from the nozzle exit to the various shock cell locations as turbulence generally loses coherence at shorter distances[59]. An explanation of the spatial shear layer turbulence coherence could be due to its modulation from the formation of standing wave patterns along the shear layer, the experiments conducted by Panda[43,44] measured the shock vortex interaction of under expanded jets using Rayleigh scattering and explained that the standing wave patterns along the jet drives the amplitude modulation of the shear layer's convecting instability waves. This led to the formation of organized vortices that interacted with the shock train and produced compression and rarefaction parts of the generated sound waves.

Due to the observations of shock noise generation mechanisms being linked to convecting vortical[38,60,61] and turbulent structures in shear layers interacting with shock waves, a better understanding of these flow types is needed. Numerical simulations were conducted as a "modeling problem" of a single shock cell interacting with a mixing layer to gain a better understanding of the flow physics and the noise generation mechanisms.

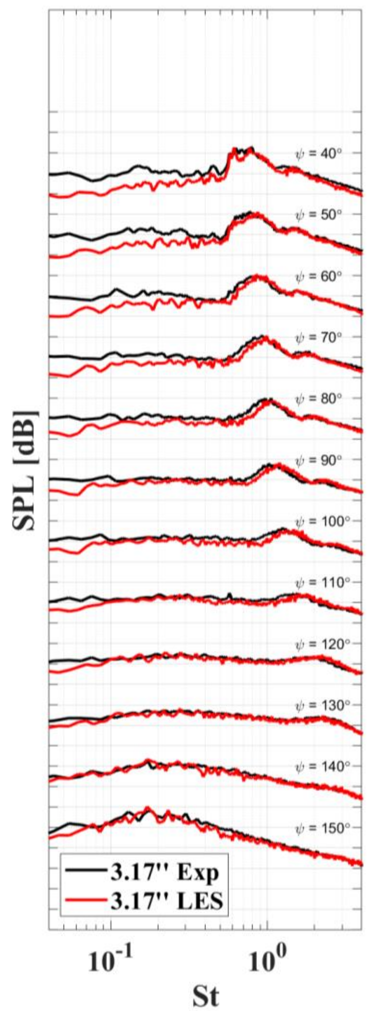

Figure 1.7: Example of broadband shock noise SPL spectra at various observation angles.

These simplified models were studied by Maning & Lele were they simulated a vortex laden shear layer interacting with a shock cell and observed acoustic emission near the interaction point and interpreted the mechanism as "shock leakage" mechanism. Later, Lui & Lele[62] studied the shear layer turbulence interaction with the shock tip and found that the shock tip reacts to the local incoming turbulence velocity fluctuations and moves downstream and then "recoils" upstream leading to noise generation, they also revisited the shock leakage mechanism and found that it also reacts to larger amplitude velocity fluctuations leading to larger motions of the shock tips. These studies have some limitations due to the simplifications applied to their simulations. However, studies utilizing the full Navier Stokes equations were solved using Direct Numerical Simulations (DNS) for the supersonic-subsonic mixing layer interacting with a shock wave and incorporated a spatially developing turbulent shear layer were conducted by Schaupp et al.[63] and Shi et al.[64]. These studies showed that the noise generation is due to interaction of shear layer vortices and shock waves which have a mixing noise component in the downstream direction and a shock noise component with a preferential upstream direction. When the shear layer was forced at a specific frequency it generated organized vortices with spatial coherence and emitted strong upstream acoustic waves at the interaction frequency. In addition, the study by Shi et al.[64] identified two noise generation mechanisms for the shock turbulent shear layer interaction, first the turbulence influences the movement of the shock waves, and second the turbulent structures are compressed reducing their scales and increasing pressure fluctuations, these lead to shock noise emissions. In addition, Ren et al.[65] carried out numerical studies of oblique shock waves interacting with the supersonic mixing layers and showed the time evolution of the interaction revealing the formation of transmitted, reflected, and refracted shocks. The complex nature of the shock vortex interaction highlights the importance of understanding its underlying flow physics.

SHOCK VORTEX INTERACTION AND SOUND GENERATION

The studies in the previous discussion on shock turbulent shear layer interaction have a common fundamental simple flow problem of shock vortex interaction and its sound generation mechanisms. An understanding of this type of simplified interaction is necessary for a better understanding of the underlying physical processes of shock noise generation in jets and is a component of a shock turbulence interaction. The isolate shock vortex interaction has been researched extensively through experimental studies by Dosainjh et al.[66] and Weeks et al.[67], theoretical analysis by Ribner[68], and numerical simulations by Zangh et al.[69] and Inoue & Hatorri[67]. In the simulations conducted by Inoue & Hatorri[67], the study revealed that the sound generation of shock vortex interaction was closely related to the generation of reflected shock waves. This sequence of events and the quadrupolar source development are schematically shown in Figure 1.8.

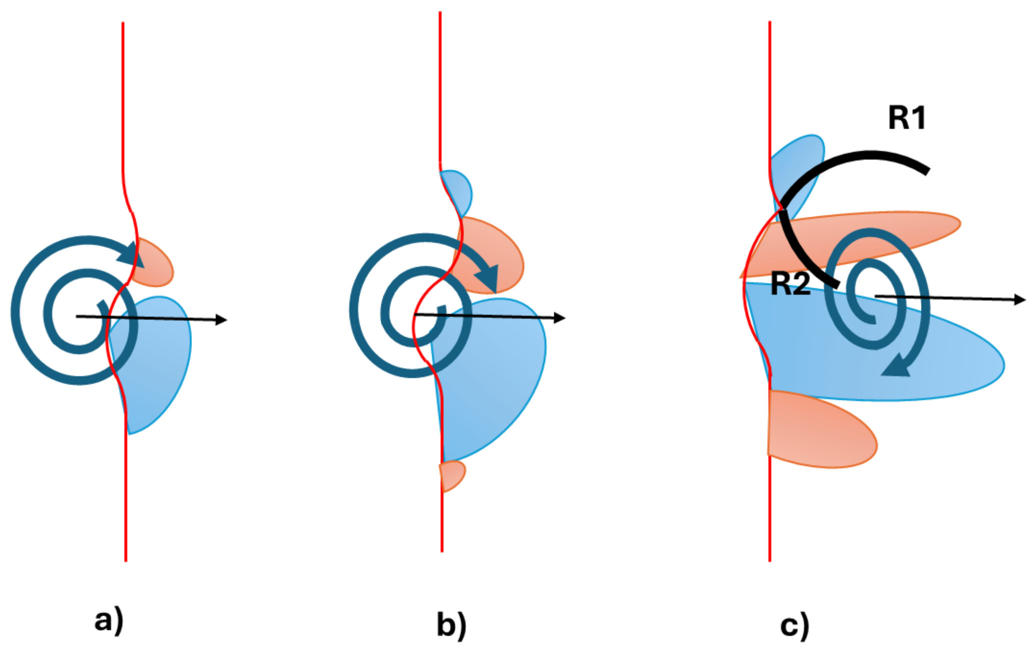

Figure 1.8: Sequence of events showing pressure field for sound generation of shock vortex interaction red shaded regions (positive pressure), blue shade (negative pressure), R1 and R2 are reflected shocks.

As the vortical structure passes by the shock wave it causes it to deform and give rise to regions with higher and lower pressures with azimuthal variation and inducing the generation of sound from quadrupolar type sources. Chatterjee & Vijayaraj[70] conducted DNS simulations with a larger computational domain of the shock vortex interaction where an initially circular vortex would deform into an elliptical vortex due to its interaction with the shock wave. The simulations captured the generation of multiple sound waves being emitted from the quadrupolar nature of the rotating elliptical vortex.

Since shock vortex interactions form the basis for shock noise generation in supersonic jets, understanding their physical mechanisms and methods of controlling them are necessary to control shock containing supersonic jet noise emissions.

NOISE REDUCTION DEVICES

There have been numerous studies conducted on jet noise reduction, and many technologies have been developed. This encompasses both passive and active techniques. Examples of passive noise reduction devices include tabs[71], ejector mixers[2], corrugated nozzle surfaces[72],and chevrons[73–76]. Fluidic injection[75,77,78] has been developed as an active noise reduction method with the ability to turn it on as required but with the added complexity of fluid delivery to the nozzle. A common trend in the implementation of passive noise reduction devices is placing geometric elements at the nozzle exit. They showed limited noise reduction gains, particularly for takeoff conditions. This is due to the fact that the nozzle operates in the overexpanded flow regime where flow separation can occur before the jet plume exits the nozzle, leading to reduced interaction of the flow with such devices. In full-scale testing, chevrons have been reported to achieve overall sound pressure level (OASPL) noise reduction of 2-3dB [79]. The objective of this study is to maximize noise reduction at take-off condition within an acceptable minimal thrust loss range. Since the generation of jet noise is closely linked to the flow field of the jet, any noise mitigation approach would need to influence the flow field and modify it. This can be achieved by various methods under the category of flow control. The interest in this research is using vortex generators as flow control devices for applications in supersonic jet noise reduction.

Flow control and vortex generators

Vortex generators (VG) are aerodynamic devices that generate streamwise vortices which are induced by a pressure gradient across the upstream and downstream surfaces of the device and causing the incoming flow to swirl and acquire and angular momentum component, this mechanism is schematically shown in Figure 1.9. VGs are used to control the flow of boundary layer separation on airfoils[80,81] by energizing the boundary layer's momentum to overcome the adverse pressure gradient in its flow path leading to flow attachment and increased aerodynamic efficiency. VGs are also used to control and reduce the formation of large vortical structures that develop from shear flows and mixing layers. Where the stream-wise rotating vortices breakdown the coherent structure formation leading to noise reduction benefits for the large-scale mixing noise component of the jet flow. In supersonic flows, VGs have been implemented as hypermixer fuel injectors enabling convective mixing. In addition, VGs placed in supersonic flows induce the formation of oblique shock [82,83] which can be beneficial for controlling shock turbulence interactions as well as reducing the shock strength in shock containing jets.

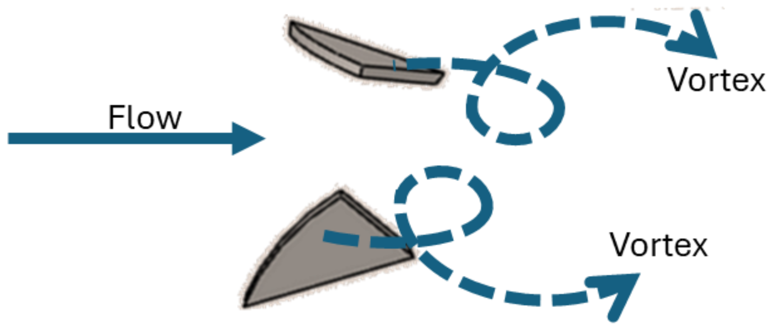

Figure 1.9: Incoming flow interacting with VG surfaces to produce counter-rotating vortices.

MVG nozzles

A new noise reduction technology for supersonic jets explored in previous studies[8–10,84,85], showed substantial noise reduction gains, where vortex generator blades were placed inside the supersonic nozzle. This technology is referred to as Micro Vortex Generators (MVGs), since the height of the vortex generator blades is much smaller compared to the nozzle exit diameter.

The advantage of MVGs is that they can be placed inside the nozzle to avoid the flow separation regions when the jets are overexpanded. This allows them to have a more effective interaction with the nozzle flow. Also, the parameter space of MVG nozzles is larger than most of the other noise reduction devices, this allows the designer to tailor MVGs to achieve a desired noise reduction profile for specific operating conditions. For example, the axial location of MVG placement inside the nozzle can be selected in such a way that the induced oblique shock waves generated by the MVG blades can interact with the shock cells originating from the nozzle throat, causing destructive interference to weaken the shock cells. This reduces the broadband shock-associated noise (BBSN) of the jet flow[85]. When the MVG devices are placed inside the nozzle, where their interaction with the flow is more effective, it allows the generation of much stronger counter-rotating streamwise vortices that mix and disperse the shear layer[8]. These strong streamwise vortices are essential for mitigating the low-frequency large-amplitude turbulent mixing noise, because they can interrupt the formation and development of coherent structures in the early stages as the flow travels along the jet shear layer. More specifically, the aim of tailoring these strong streamwise vortices is to inhibit or minimize the mechanisms of the formation of large coherent structures convecting along the shear layer. The formation of these structures is responsible for the generation of the high-intensity turbulent mixing noise, this constitutes a large component of the supersonic jet noise and has a directivity dominating the downstream observation angles 120º-135º from the nozzle inlet axis[16]. These large turbulent structures that appear in supersonic shear layers, have their development and length scales tied to the convection Mach number and the wake resulting from nozzle lip thickness[25]. Also, a "tilt-stretch-tear-pair" mechanism of the shear layer structures was identified by Thurow[15] and was linked to the noise generation of turbulent mixing noise in the work of Hileman[86]. Karami[45] studied the growth of shear layer structures in underexpanded impinging jets and observed that the turbulent structures growth exhibited a roll up and pairing mechanism similar to that proposed by Winant and Browand[12]. Where consecutive vortices roll around each other and coalesce to form a larger vortex. Thus, using MVGs as a noise reduction approach impacts the development of large turbulent structures and shock cells strength. This approach to jet noise reduction becomes effective because the two largest components of noise sources of supersonic jets; turbulent mixing noise, and shock noise[61,87], are being targeted for high noise reduction gains.

Like chevrons and tabs, MVGs are capable of suppressing screech tones as well as reducing BBSN in jets due to the impact of counter-rotating stream-wise vortices on the formation of coherent structures in the shear layer that interact with the shock cells. The added benefit of MVGs is the generation of internal oblique shocks impacting the strengths of the shock cells, this can provide an opportunity to understand the interaction mechanisms responsible for the generation of these noise components, as well as the jet instability modes, and can aid in understanding how the internal trapped waves can be influenced and controlled. Recently, the jet noise community has seen increased research activity in jet instabilities, shock leakage[46], guided jet modes G-JM (trapped waves), and acoustic radiation of wave packets[28]. The internal trapped waves were found to be linked to the near field pressure fluctuations and jet instabilities and are inherent in high subsonic and supersonic jets [56], and has also been found to interact and excite the shear layer instabilities[88,89].

Modifications of the nozzle exit geometry was found to have a large influence on the jet instability characteristics, the screech closure mechanism[90], and on the internal upstream propagating waves to drive the jet instability. The guided jet modes G-JM were observed to be generated by the interaction of the Kelvin-Helmholtz structures (K-H waves) traveling along the shear layer and interacting with the shock cells[47]. Some of these aspects of the jet instabilities, the K-H waves, and internal trapped waves can highlight the relevance of MVG nozzles in understanding their underlying mechanisms, where MVGs can be used because they allow the control of the interaction of the shear layer turbulence levels with variation of the jet's shock cell strengths and could directly influence the internal trapped waves of the jet instability modes, and the BBSN acoustic radiation.

RESEARCH OBJECTIVES AND CONTRIBUTIONS

The objective of this dissertation is to study the fundamental noise generation processes and how noise reduction devices impact these mechanisms. This will provide insights that enable the development of effective supersonic jet noise reduction devices, and a method to assess various configurations' impact on the jet flow and its emitted noise. As mentioned in the previous paragraphs, the previous studies examined various supersonic noise-generation mechanisms from different aspects of the flow field primarily the interaction of shear layer vortices and the shock cells and the associated internal and external waves. However, there is a lack of a comprehensive understanding of the complete noise generation mechanism from acoustic sources within the flow field and how acoustic waves are emitted and propagated from the jet into the acoustic near-field and eventually to the acoustic far-field. In addition, a better understanding of the fundamental mechanisms responsible for reducing the acoustic noise emissions of jets with noise reduction devices is needed.

The contributions of the research presented in this dissertation include extensive investigations using various experimental methods and numerical simulations, which are utilized to study the noise reduction mechanisms of MVG nozzles. In addition, high speed schlieren visualization is utilized to examine the flow field and the generated internal waves and external acoustic wave emission. Since the captured data is time-resolved, spectral methods utilizing Fourier transformation can be applied to examine the temporal frequency and the spatial wavenumber content to characterize the flow field and the acoustic emissions. Furthermore, a reconstruction of the flow field using only the propagation acoustic wavenumbers is carried out to reveal the associated waves and the generated sound. The reconstructed wave fields are examined in relation to the acoustic near-field and far–field microphone measurements. On the other hand, the shock noise generation mechanism is analyzed from the interaction of the shear layer vortices with the shock cells, and a noise generation model is proposed. Finally, the developed analysis methods are used to evaluate noise reduction devices based on their impact on the noise generation mechanisms leading to a comprehensive understanding of noise component reduction and suppression observed in the acoustic emissions.

Chapter 2: Experimental and numerical approach

JET RIG FACILITIES

Experiments were conducted in two jet rig facilities the Aeroacoustics Test Facility (ATF) and the Heated Jet Noise Facility (HJNF) both facilities are located at the Gas Dynamics and Propulsion Laboratory (GDPL) at the University of Cincinnati. The ATF houses a jet rig in an anechoic chamber measuring 25 ft × 23 ft × 11 ft, the walls, ceiling and floor of the ATF are acoustically treated for a frequency cutoff of 500 Hz. A schematic of the chamber is shown in Figure 2.1(a) The ATF facility has instrumentation in the chamber measuring ambient conditions as well as flow conditions inside the jet test rig. The HJNF is another anechoic chamber measuring 15 ft × 11 ft × 10 ft that is acoustically treated for a low cutoff frequency of 350 Hz and also houses an instrumented jet rig. However, the HJNF can be heated for high temperature jet experiments. The use of both facilities provided the flexibility of setting different measurement techniques at the same time, for example one rig for acoustic measurements, while the other was setup for flow visualization and velocity measurements and can switch between them when needed. Instrumentation in both rigs included pressure and temperature transducers for the plenum and the ambient, while relative humidity measurement was for the ambient. The jet rigs can be operated by a control panel to set the jet operating conditions, which were recorded by a computer using LabVIEW. Air flow into the HJNF passed through two inline flange heaters with a rating of 72kW followed by a 96kW that can be operated to heat the jet up to a nozzle temperature ratio NTR=2.5 for the small nozzle size used in this study.

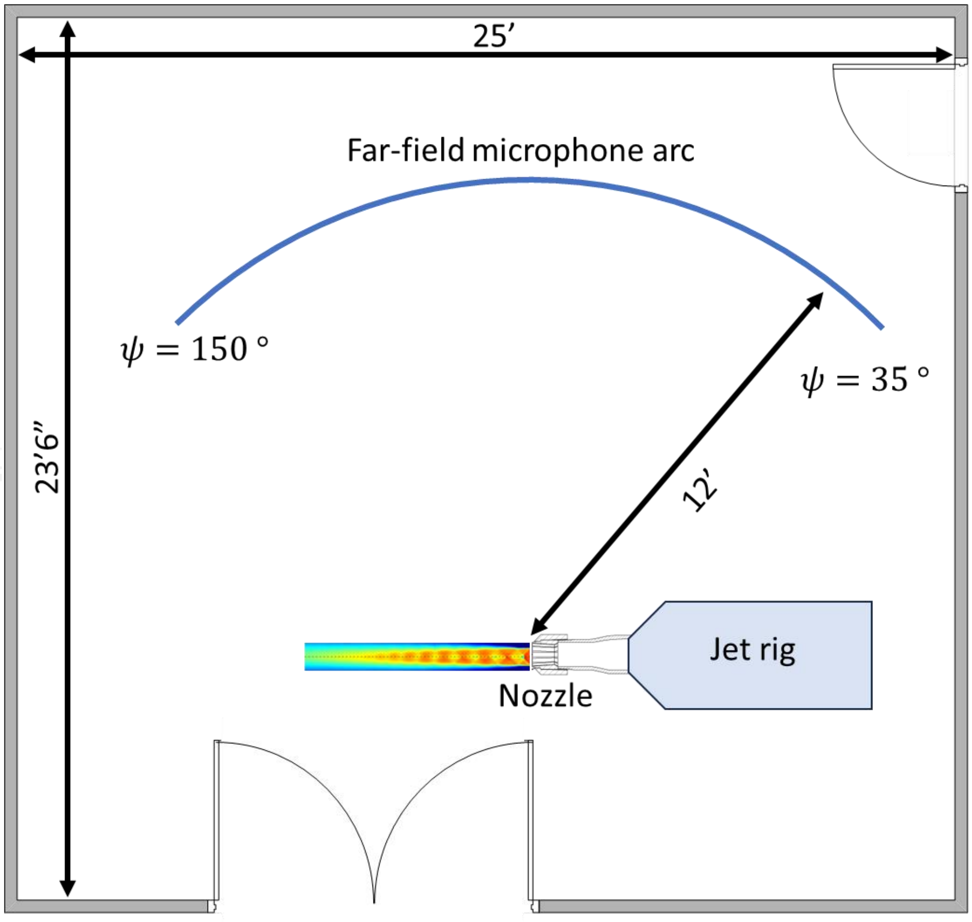

Figure 2.1: ATF anechoic chamber schematic.

The air supply for both facilities is supplied by both a low-pressure air system and a high-pressure air system. The low-pressure air system Figure 2.2 consists of an Atlas Copco screw compressor providing a pressure supply of 150 psi, this compressed air passes through a dryer to remove moisture before filling the low-pressure tank. An isolation valve V1 followed by a pressure regulator R1 feeds supply air into a main header line that passes through the entire lab supplying all experimental test rigs. A secondary set of valves (V2 and V3) and regulators (R2 and R3) supplies air from the main header into the jet rigs in both facilities independently. The secondary regulators R2 and R3 are used to control the jet rig plenum pressure for the experiments. The high-pressure air system has a Worthington HB3 piston compressor and can supply high pressure air at 1500 psi through a similar setup to the low-pressure system and feed air to the a main high-pressure header running along the lab. A detailed description of the facility can be found in a previous work[91].

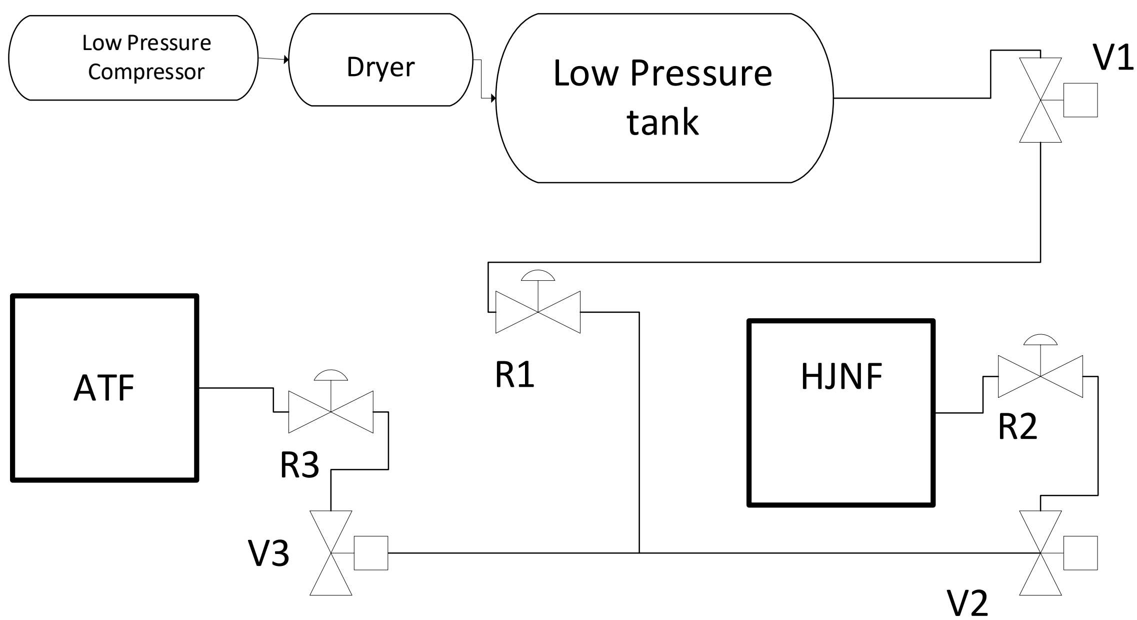

Figure 2.2: GDPL air supply system for ATF and HJNF.

PARTICLE IMAGE VELOCIMETRY (PIV)

PIV was conducted at the heated jet facility with a slightly higher Nozzle Temperature Ratio NTR=1.05 to minimize condensation from contaminating the measurement field. The laser used was an Evergreen double pulsed Nd:YAG laser with a wavelength of 532nm, operating at a pulse rate of 5 Hz with a 0.5-microsecond inter-pulse delay. Two LaVision imager intense CCD cameras were used with a resolution of 1376 × 1040 pixels fitted with Nikkor 50 mm lenses, with a magnification of 12.55 pixels/mm. The entire PIV system was placed on a traverse system to capture flow data along the jet axial direction covering a distance of up to X=15D of the small nozzle. The timing and acquisition were controlled using LaVison's time control electronics and the vector computations of the velocity fields were computed in Davis 8.4. PIV cross-correlation calculations were performed on an initial interrogation window size of 128 × 128 pixels and a final interrogation window size of 32 × 32 pixels with the resulting vector field contained 174 × 132 vectors for each camera and the total field of view with the camera overlap resulted in a vector field of 888 × 132 vectors with a spatial resolution of 0.61mm or 0.0167D. A total of 1200 image pairs were captured for computing statistical quantities. The PIV field of view shows a cross-section with the laser sheet passing through the jet centerline and the midpoint of the nozzle seal flat surfaces (also the midpoint in between MVG blade pairs) as indicated in the nozzle schematic in Figure 2.3, hence the PIV results only show the MVG impact on the flow field in this plane. Examples of the instantaneous raw images, instantaneous vector field, and the mean average of the vector field is shown in Figure 2.4. The core flow was seeded using Aluminum Oxide tracer particles with a nominal diameter of 0.3 micrometers. The particles were heated in an oven to remove moisture and reduce agglomeration. The seeding unit consists of a fluidized bed and a cyclone separator to ensure a uniform distribution of seed particles with minimal agglomeration. The ambient flow was seeded using a water based fog machine providing fog particles with manufacturer's specified nominal diameter of 1 micrometers.

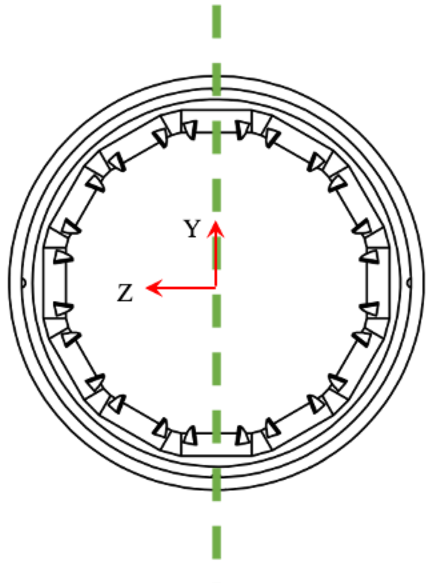

Figure 2.3: PIV laser sheet orientation (green dashed line) relative to the nozzle. Nozzle view from exit plane into the nozzle.

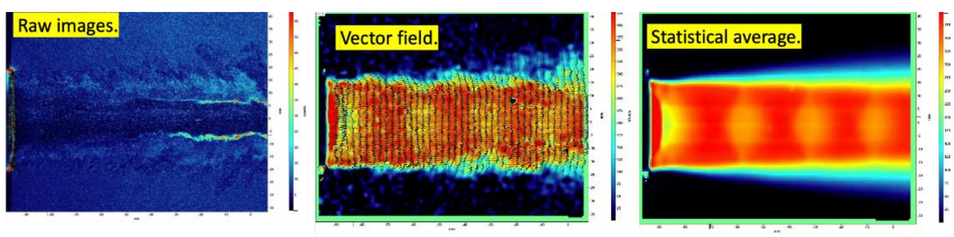

Figure 2.4: PIV processing example showing an instantaneous raw image, instantaneous vector field, and mean vector field

Uncertainty quantification PIV

The working principle of PIV measurement is to capture the motion of tracer particles that are seeded into the flow. This is achieved by capturing a double frame image separated by a time delay ΔT, which allows a cross-correlation algorithm to track particle motion through pixel shift. The relation between the pixel shift and the displacement measurement is established by an image calibration procedure, which maps the physical space onto the pixels of the imaging sensor. The various elements of the system and the measurement procedures introduce many sources of uncertainty to the PIV measurement technique which needs to be quantified.

The selection of traces particles needs to address certain requirements to deliver accurate results. The particle characteristics should be able to follow the fluid path with negligible particle lag. This depends on the particle diameter size and density. For accurate supersonic flow results, the particles should have Stoke's number less than 0.2 which leads to velocity errors less than 2% (Samimy and Lele 1991[92]). The particles should have a minimal time constant for its frequency response in dynamic flows, the method outlined by Tavoularis[93] is used to obtain some estimates on the particle behavior used in this study.

For Aluminum Oxide tracers, the particle diameter and density are $d_p = 0.3\mu m$ and $\rho_p = 3950\ kg/m^3$. Both the viscosity and kinematic viscosity values are assumed to be at standard temperature and pressure for the estimates. $\mu_f = 1.849 \times 10^{-5} \frac{kg}{m\,s}$ $\nu_f = 1.5 \times 10^{-5} \frac{m}{s}$ For seed particles much denser than the carrying fluid, a Stokes flow analysis can be used for the seed particle response with the criteria:

$$\gamma = \frac{density\ particle}{density\ fluid}$$

$\gamma \gg 1$ where $\gamma$is the density ratio. And the time constant for particle response is given by:

$$\tau_p = \frac{\rho_p \, d_p^2}{18\mu_f} \approx 1\mu s$$

The steady state frequency response for a particle is given by:

$$\eta = \frac{1}{\left(1 + \omega^2 \tau_p^2\right)^{0.5}}$$

where η: is the amplitude ratio, and ω: is the frequency fluctuation. This shows that particles would behave as a first-order low-pass filter, having a 3dB a cut-off frequency of:

$$\omega_c = \frac{1}{\tau_p}$$

and a Stoke's number of:

$$Stk = \left(\frac{\omega d_p^2}{8\nu_f}\right)^{1/2} \approx 0.03 < 0.2$$

The obtained Stoke's value is within the constraint for accuracy in supersonic flows with velocity errors less than 2% hence, the selected particles are adequate for the current measurements.

In addition to the uncertainty introduced by the particle lag, the statistical quantities of the measured flow velocities also introduce a sampling error due to the number of samples. The uncertainty of the mean velocity from the sampling error is given by:

$$\delta\overline{U} = t\frac{u_{rms}}{\sqrt{N}}$$

Where N is the number of samples, and t is given by the student's t-distribution for a chosen confidence interval. The computed sampling uncertainty values of the mean velocity components for the current PIV measurements are shown in Figure 2.5 (a-c) for a 95% confidence interval. The distribution contours show high uncertainties within the shear layer that peaks around 1% for the axial mean uncertainty normalized by the jet velocity for a sample size N=1200. Figure 2.5(c) shows the peak uncertainty variation of mean axial and transvers velocities as a function of sample size showing an asymptotic approach indicating that the number of samples in this study (N=1200) is sufficient.

To quantify the PIV uncertainty the following uncertainty propagation analysis is carried out. The instantaneous data subpixel accuracy of the processing algorithm is:

$$\delta x = 0.1\, pixel$$

And the calibrated PIV image has a mapping with a pixel scaling of:

$$120mm \approx 1200pixels$$

Based on the flow field velocity and the time delay between the double frame images, the convecting particles in the flow field would a distance between the frames which is the pixel shift $\approx 8 - 12\, pixels \ \approx 10\, pixels$. This leads to a pixel uncertainty:

$$\delta U_{pixel} = \frac{0.1}{10} * \frac{1}{\Delta T} * pixel\ scale \approx 2\, m/s$$

$$\frac{\delta U_{pixel}}{u_j} \approx 0.5\%$$

In addition, the sample size of the data set introduces additional sampling uncertainty for average statistical quantities: u_{mean}, the sampling uncertainty is given by:

$$\delta u_{mean} = 2\sigma_m = \frac{2\sigma}{\sqrt{N}} = \frac{2u_{rms}}{\sqrt{N}}$$

And the maximum RMS values are found to reach $\frac{u_{rms}}{u_j} \approx 0.2\frac{u_{rms}}{u_j} \approx 0.2$. In order to maintain a reasonable velocity uncertainty, it is desirable to have enough samples to keep the velocity uncertainty to around $\delta u_{mean} \approx 1\%$.

The minimum required samples to achieve data convergence is N=1000N > 1000 samples and the total contributions from the various uncertainties is given by:

$$Total\ Uncertainty = \sqrt{\left(\delta U_{pixel}\right)^2 + (\delta u_{mean})^2 + (\delta seed\ particle)^2}$$

$$\approx \sqrt{(1\%)^2 + (0.5\%)^2 + (1)^2} < 3\%$$

These calculations indicate that in order to obtain a total uncertainty below 3%, the number of samples should be greater than 1000, which is satisfied in this PIV measurements.

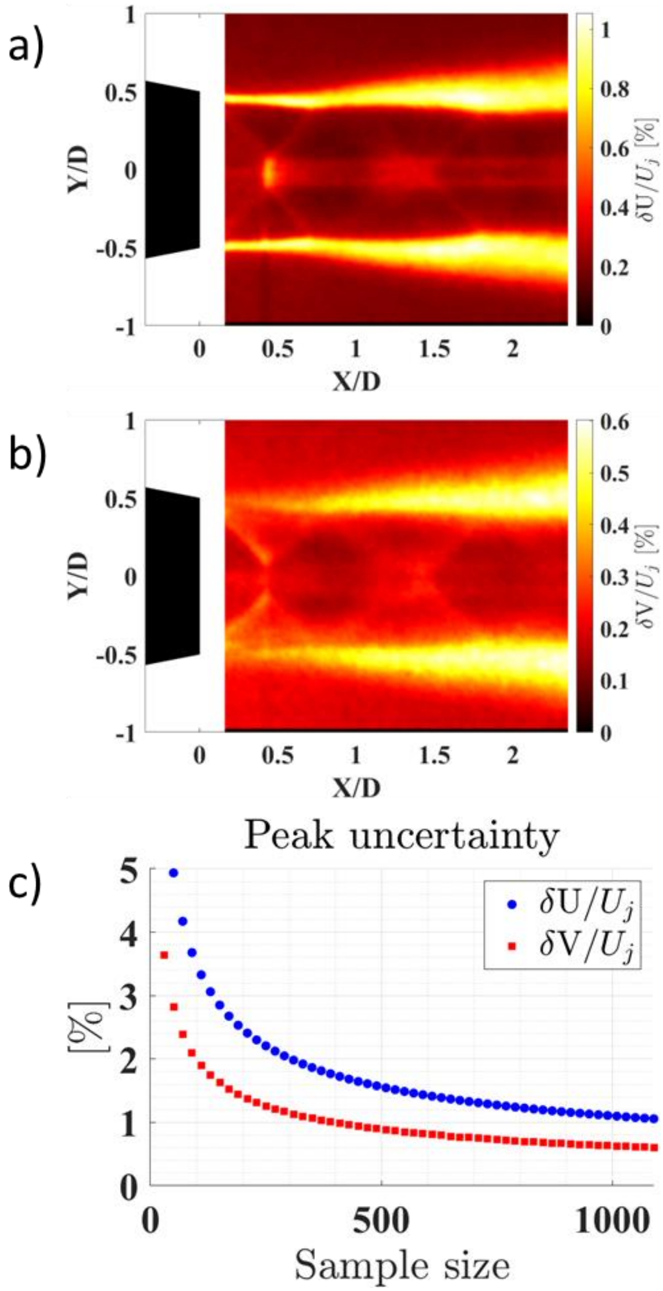

Figure 2.5: Distributions of PIV uncertainties with 95% confidence interval of the mean velocity field for, a) axial velocity, b) transverse velocity, and c) peak uncertainty as a function of sample size. The velocity uncertainty is normalized by the jet exit velocity and given as percentages. The nozzle operating condition is for NPR=3.5.

SCHLIEREN VISUALIZATION

Schlieren visualization is an optical measurement technique that visualizes the density variation in the flow field, where light beam passing through a medium with density gradients causes light refraction[94]. The beam is then focused to a point on a knife edge and the translation of refracted portion of the beam is magnified at the focal point and is either blocked by the knife edge or passes by it. This appears in the image as darker or brighter regions, respectively.

Two schlieren setup were used in this study, a single mirror coincident Schlieren arrangement, and a two mirror Z-type Schlieren arrangement. The light source is an Oriel mercury arc lamp, the light beam passes through optical elements before reflecting off a parabolic mirror. The mirror is a first surface reflective mirror with diameter of 12" and has a focal length of 72". The knife edge orientation is perpendicular to the jet flow to reveal density vitiations in the jet along its axial direction with light intensity cutoff of 50%. The images are acquired by a high-speed Phantom v1610 camera with sampling rate 204.8 kHz with a total of 5000 images.

Schlieren Analysis

The flow field from Schlieren imaging is processed using a peak detection algorithm to identify light intensity peak locations. This information is used to measure the mean shock cell location and compute its spacing. Since schlieren is acquired at high frame rates, the light intensity time series signal can be extracted for further time series analysis using Fast Fourier Transform (FFT), which decomposes the temporal signal into a frequency spectrum. The schlieren image sequence is processes in the frequency domain to isolate flow dynamics and its resulting acoustic waves at specific frequencies of interest which is computed by:

$$I(x, y, t) = \hat{a} \sum_{\omega} e^{-i\omega t}$$

Where I: is the image intensity, $\hat{a}$: is the Fourier coefficient, and ω: is the angular frequency.

The FFT is also conducted in both time and axial space directions leading to a spectra in frequency-wavenumber (f-k) domain. This is conducted on the extracted time history along axial lines revealing wave patterns convecting along them. The wavenumber is defined as:

$$k = \frac{2\pi}{\lambda}$$

Where k: is the wavenumber, and λ: is the wavelength. The wave propagation speed is defined as:

$$u_p = \frac{2\pi f}{k}$$

A frequency based cross-correlation is computed in the frequency domain and then transformed back into the time domain resulting in spacetime correlations of the convecting turbulent structures along the nozzle lip-line. The slopes of the correlation peaks are then extracted to compute turbulent structures convection velocities.

Flow features propagating in the downstream direction and waves propagating in the upstream direction are separated from the raw schlieren images to visualize the dynamics of each feature. This is achieved by applying a filter on the wavenumber content. Where positive wave number is downstream propagation direction, and negative wavenumber is upstream propagation direction. The decomposition is given by:

$$I(x, y, t) = \sum_{k} \sum_{\omega} \hat{I}_{k,\omega}\, e^{ikx} e^{-i\omega t}$$

$$k < 0: \mathit{upstream\ propagation}\ \ , k > 0: \mathit{downstream\ propagation}$$

To evaluate the wavenumber content of the entire measurement field at a specific frequency, the frequency dependent axial wavenumber distribution is computed by:

$$I(x, y, t) = \hat{a}e^{-i\omega_0 t}e^{ik_0 x}$$

FLUORESCENCE SURFACE OIL FLOW VISUALIZATION

Fluorescence surface oil flow visualization was conducted by applying a mixture of oil and fluorescent pigments with equal volume ratios to maintain a suitable viscosity to trace the nozzle flow features. A UV lamp was utilized for illumination and images were captured by a photographic camera.

ACOUSTIC MEASUREMENTS

Acoustic measurements were acquired using model 4954 Bruel and Kjaer ¼ inch free-field condenser microphones with a frequency response of 100kHz. The microphones are installed on an arc array with 12 microphones covering observation angles from $\psi = 40°$ up to $\psi = 150°$ in $10°$ increments, with the flow direction defined at $180°$. The measurements were sampled at 204.8 kHz for a duration of 5 seconds with a National Instruments PXI sound and vibration module. For the near-field data, the measurements were taken using 15 microphones that were traversed covering an axial distance of X=25D and radial distance of R=10D of the small nozzle with data collected at more than 3000 grid point locations for each test case. The instrumentation and data acquisition are identical to those used for the far-field measurements. Figure 2.6 and Figure 2.7 show the microphone setup for acoustic far-field and near-field measurements relative to the nozzle.

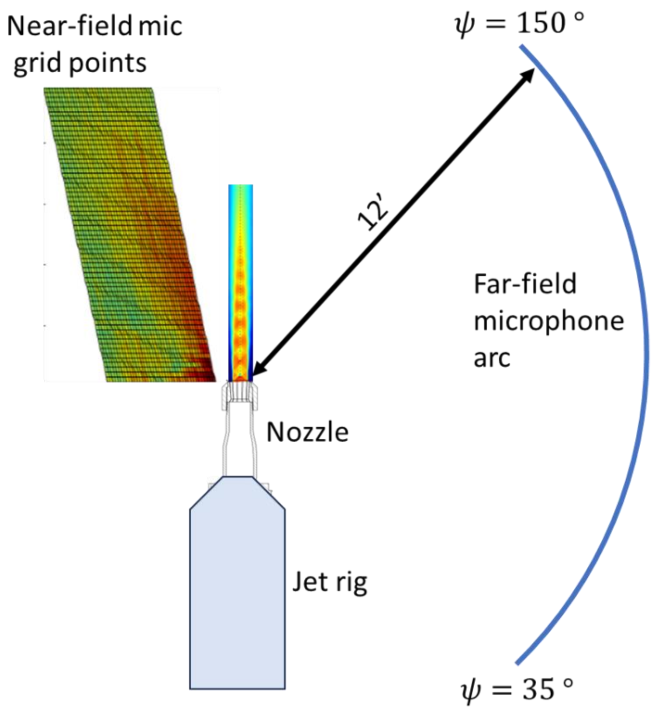

Figure 2.6: Schematic of microphone setup for acoustic far-field and near-field measurements.

Figure 2.7: Far-field and Near-field microphone arrangements

Acoustics: SPL, OASPL, and Atmospheric corrections

The time series pressure data of the microphone measurements is processed using a Fourier transformation to obtain its spectral contents. This is done by computing the narrow band sound pressure level (SPL) for a given frequency band range of $\left[f - \frac{\Delta f}{2}\ ,\ f + \frac{\Delta f}{2}\right]$ and is given by:

$$SPL_n = 10\,Log_{10}\left(\frac{2S(f)\Delta f}{P_{ref}^2}\right)$$

Where P_{ref}: is the reference pressure for hearing threshold, Δf: is the frequency resolution, and $S(f)$: is the power spectral density and is given by

$$S(f) = \frac{\left(\frac{F(f)}{N}\right)^2}{\Delta f}$$

The Overall Sound Pressure Level (OASPL) over the entire frequency range is computed by:

$$OASPL = 10Log_{10}\left(\sum_{k=0}^{N-1} \frac{2S(f)\Delta f}{P_{ref}^2}\right)$$

The processing procedure for the far-field acoustics requires an extra step to account for losses caused by atmospheric attenuation of acoustic waves traveling the large distance to the far-field microphone locations especially the higher frequency noise components, this is not an issue for the Near-field measurement because the attenuation across the shorter distance of the near-field is negligible. To account for the frequency dependent attenuation, a correction factor is applied to the noise spectra. The correction factor is computed using the method outlined by Bass et al.[95,96]. Figure 2.8 shows a plot of the correction factor variation with frequency and relative humidity (RH), and sample results of the SPL and OASPL are shown in Figure 2.9 with and without atmospheric attenuation corrections.

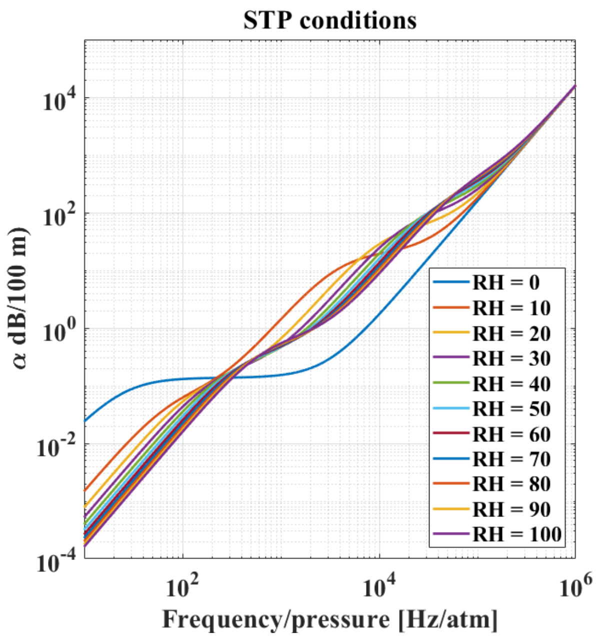

Figure 2.8: Atmospheric attenuation correction factor at standard temperature and pressure for various relative humidity (RH) values

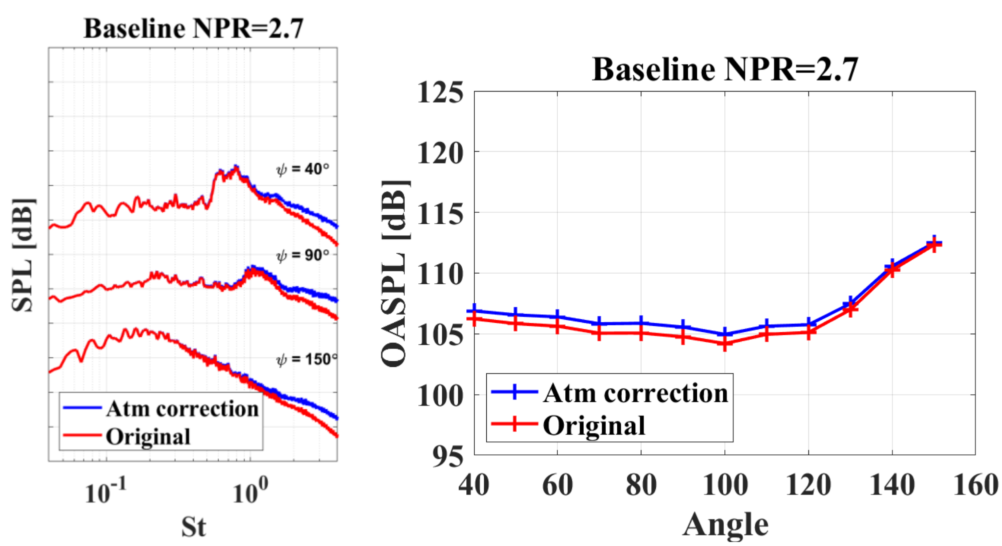

Figure 2.9: Narrowband SPL (left), and OASPL (right). Red curves show original results with no atmospheric attenuation corrections, blue curves show results including atmospheric attenuation corrections

NUMERICAL METHODOLOGY AND SETUP

Numerical simulations were provided by the collaborators from the Naval Research Laboratory and were computed using the JENRE® Multiphysics Framework. For the jet flow and acoustics simulations, a nodal Taylor-Galerkin finite element flow solver with a flux-corrected transport method was utilized on a tetrahedral mesh. Also, they used a development version of the JENRE® Multiphysics Framework extended to implement an equilibrium wall-model method to capture boundary layer effects on the nozzle wall[97,98]. The computational domain is shown in Figure 2.10, showing markings of the control points indicating the cell size distribution outside the nozzle and is summarized in Table 2-1, which is similar to our previous practices [8,85,99].

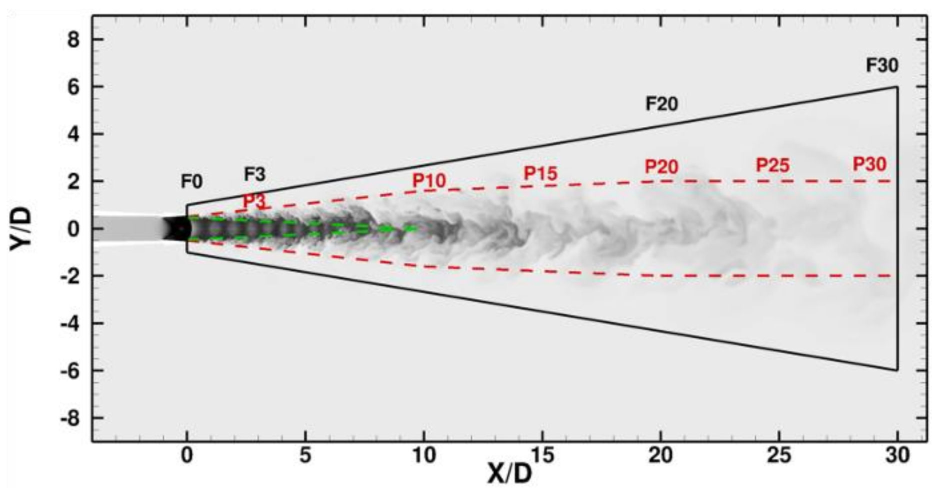

Figure 2.10: Locations of the control points in the computational domain. the cell size distributions are specified at the control points P3 to P30 and F0 to F30 for the jet plume and near-filed. The FW-H surface is indicated by the black lines and are used for the far-field acoustic prediction. The control points specifications are provided in Table 2-1, (LES computational domain from Liu et. al.[8])

Table 2-1: Control points specifications for mesh generation (from Liu et. al.[8]).

Control points	**P3**	**P10**	**P15**	**P20**	**P25**	**P30**	**F0**	**F20**	**F30**
Cell sizes	D/150	D/30	D/25	D/20	D/15	D/5	D/40	D/10	D/5
Radius	0.7D	1.6D	1.8D	2.0D	2.0D	2.0D	1.0D	4.3D	6.0D
Axial location	3D	10D	15D	20D	25D	30D	0D	20D	30D

The cell size follows a linear distribution in the axial direction, and a logarithmic distribution in the radial direction. To capture the flow inside the nozzle, a finer cell size distribution is used in the near nozzle wall region. At every control point the cell size is D/300, whereas the cell size at the nozzle core is D/160. On the nozzle wall, a much smaller cell size is used with D/1200. Upstream of the nozzle throat, a larger cell size of D/300 is used. The total number of nodes ranges from 56M up to 70M for the baseline nozzle, and the increased number of nodes is for MVG nozzles, here "M" stands for one million. For further information on the numerical setup, the reader is referred to previous work [99].

Throughout this paper, comparisons are drawn between the laboratory experiments and numerical simulations of the flow field and its related acoustic field for the various nozzle configurations. The numerical simulations allow for a wealth of information and insight into the flow and noise reduction mechanisms in effect, including intricacies of internal flow details that are obscured from the experimental measurements. Even though it might be implied, it is worth noting that another important outcome of this approach is the validation of the noise reduction effectiveness of MVGs using two independent methods of experimental measurements and numerical simulations. An extensive discussion on the flow field and acoustic characteristics of the baseline nozzle from experimental and simulation perspectives has already been conducted[99,100]. The current work expands on the far-field acoustic studies performed on the MVG configurations[8–10,85] by adding new results from flow analysis and near-field acoustic measurements.

BASELINE SUPERSONIC NOZZLE

The baseline nozzle is a model scale of a GE F404 engine nozzle. The nozzle is a faceted biconical converging-diverging supersonic nozzle with an area ratio of 1.32 with a design Mach number of 1.68 at a fully expanded NPR=4.8. The nozzle geometry design is based on ground test point conducted by Ennix 1993 [101]. Two model sizes were used in this study, a large nozzle with an exit diameter of 3.166 inches, and a small nozzle with an equivalent exit diameter of 1.457 inches and experimental results from both are compared to LES simulations conducted for the larger nozzle. The baseline faceted nozzle of both sizes is shown in Figure 2.11 and only the small nozzle in Figure 2.12 (a). The nozzle operating conditions encompass the overexpanded regime relevant to takeoff conditions and include NPR = 2.7, 3.0, and 3.5 at the Nozzle Temperature Ratio (NTR) = 1. NPR = 2.7 was the nozzle pressure ratio taken from the aforementioned NASA[101] ground test.

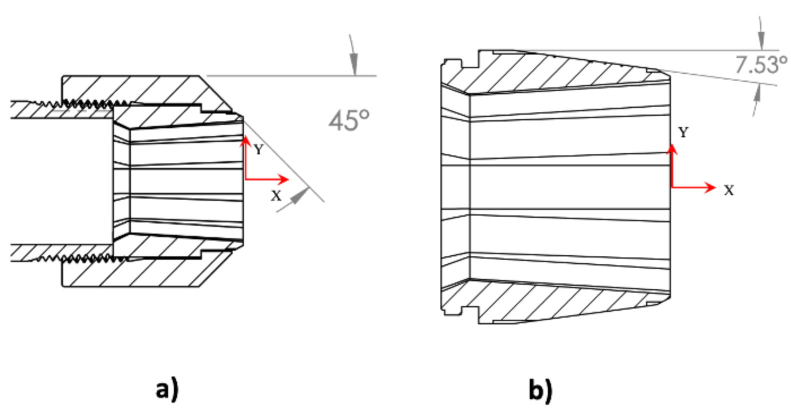

Figure 2.11: External nozzle geometry a) small, b) large nozzle.

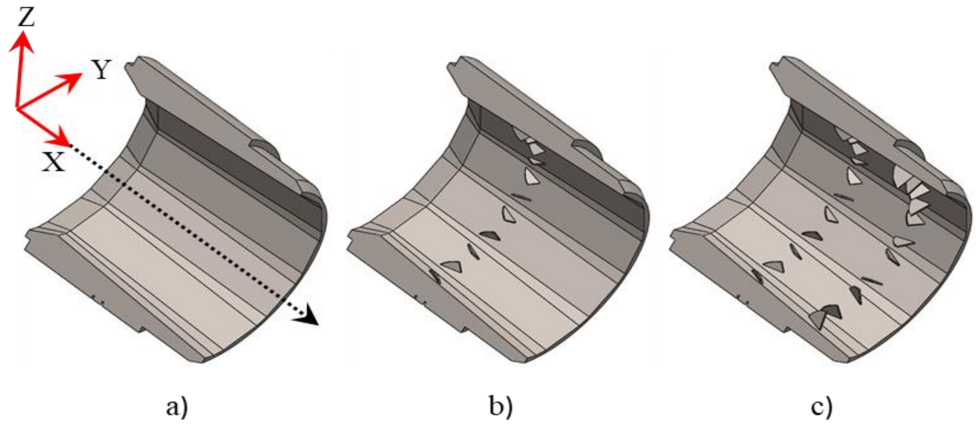

Figure 2.12: Nozzle configurations. a) Baseline nozzle. b) Single Array MVG. c) Double Array MVG. Arrow indicates flow direction.

MVG NOZZLE GEOMETRY CONFIGURATIONS

The vortex generators are based on an altered triangular profile as shown in Figure 2.13, with the following design parameters; α: fin angle perpendicular to the seal surface, β: angle between two fins in the flow direction. h/D: height of fin. x/D: fin axial location, and z/D: spacing between fins at their trailing edge. All length scales are normalized by the nozzle exit diameter, D. The MVG configurations included in this research are a single array MVG nozzle and a double array MVG nozzle shown in Figure 2.12 (b) and (c). The parameter values of the single array MVG nozzles are presented in Table 2-2. The design parameter values for the optimal noise reduction at takeoff conditions for single array MVG and double MVG nozzles are presented in Table 2-3.

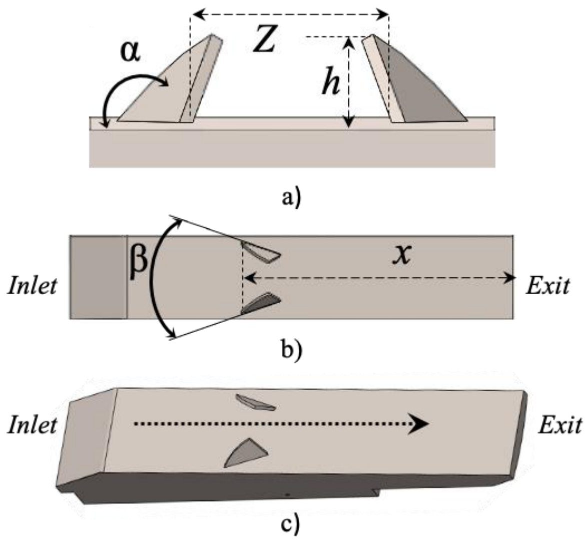

Figure 2.13: MVG parameter definitions. a) Surface angle (α), blade separation (Z), and height (h). b) Intra-blade angle (β) and axial placement (x). c) Perspective view with flow direction.

Table 2-2: Single array MVG parameter range

MVG parameter definition	*Parameter Label*	*Range of values*
Surface to blade angle	α	$60^0 - 120^o$
Blade-to-blade angle	β	$20^0 - 44^o$
Blade height	h/D	$0.025 - 0.10$
Axial location	x/D	$0.10 - 0.85$
Separation distance	z/D	$0.07 - 0.10$
Number of MVG arrays	#	$0 - 2$

Table 2-3: Design parameters of optimal Single and double array MVG nozzles

Label	**MVG location**	$\boldsymbol{\alpha}$	$\boldsymbol{\beta}$	$\boldsymbol{h/D}$	$\boldsymbol{x/D}$	$\boldsymbol{z/D}$
Single array MVG		90^o	36^o	0.05	-0.65	0.11
Double array MVG	upstream	120^o	36^o	0.05	-0.65	0.11
	downstream	90^o	36^o	0.10	-0.65	0.11

Chapter 3: Flow and Acoustic Fields Investigation of Noise Reduction by Micro Vortex Generators in Supersonic Nozzles

The role of Micro-vortex generators (MVGs) in supersonic jet noise reduction is investigated. Studies are performed to understand the noise reduction mechanisms of these devices. MVGs are implemented on a scale model representative of GE-F404 nozzles. Configurations consisting of single and dual arrays of MVGs were tested for pressure ratios relevant to take-off operating conditions. A combination of laboratory measurements and Large-Eddy Simulations (LES) are used. Particle Image Velocimetry (PIV) reveals that MVGs placed inside the nozzle form oblique shocks that interact with the jet plume's shock cell structure and greatly modify the shock-cell structure issued from the nozzle throat. This modification can weaken the jet plume shock-cell structure and even reduce the jet core velocities. Convective velocities estimated from the high-speed Schlieren imaging showed a significant reduction in magnitude caused by MVGs. When compared to the baseline design, the MVG nozzles showed noise reduction up to 10dB in the upstream direction and near 5dB in the peak downstream radiation angle at cold jet conditions. Near-field acoustic measurements showed a significant reduction of low-frequency turbulent mixing noise. Scaling analysis showed that MVGs are capable of delivering the same noise reduction performance across different model scales.

MVG CONFIGURATIONS

For highly overexpanded jets, the nozzle lip separation occurs upstream of the nozzle exit plane in the baseline nozzle[99]. Placing MVGs close to the nozzle exit plane renders them ineffective for noise reduction as the separated flow bypasses the MVGs. On the other hand, when MVGs are placed inside the nozzle at axial locations upstream of the separation region, a more effective interaction with the flow occurs and strong streamwise vortices can be generated. This depends on adjusting the different MVG parameters such as axial location, height, angle to the incoming flow, and blade-to-blade separation distances, among other parameters. In the early stages of the research, an extensive parametric study was carried out previously[85] to find an optimal MVG parameter configuration to operate at the highly overexpanded jet condition. It has been observed that the axial location of the MVGs inside the nozzle has a large effect on the flow field and the acoustic field. Another finding from these studies was that the interaction of the MVG devices with the supersonic nozzle flow generated additional oblique shocks forming inside the nozzle. These shocks interacted with both the internal and external nozzle flows, affecting the Mach disk formed immediately downstream of the nozzle exit and the shock cell structure in the jet plume. The Mach disk is a normal shock formed by the oblique expansion waves converging near the nozzle exit. These interactions depend on the MVG axial location and they could lead to either weakening the Mach disk and strengthening the jet's shock cell structures or could lead to strengthening the Mach disk and weakening the downstream shock cell structures and leading to a shorter jet core length with a slower jet core velocity. These two different effects would impact the far-field acoustics in very different ways. The optimal MVG configuration for takeoff related conditions from the earlier study[10,85] was found to have an axial location of x/D= 0.65 upstream of the nozzle exit plane, a blade height of h/D=0.05, a blade-to-blade angle of 36 degree, and a blade-to-blade spacing of Z/D = 0.11. The blade-to-blade angle of 36 degree showed optimal drag reduction in the application of airfoil flow separation at high angle of attack[80] and it also produces a favorable noise reduction results. In addition, the blade-to-blade distance should be placed as further apart as possible to prevent the newly formed streamwise vortex pairs from merging early on. The blade height needs to be sufficiently tall to enable the formation of strong vortices capable of shear layer mixing and dissipation with the lowest possible area blockage to minimize thrust losses. It was found earlier that shorter blades had limited impact on the noise reduction performance[85], whereas much taller blade heights did not produce significant noise reduction gains that justify the increased thrust losses when compared to the optimal blade height of h/D=0.05.

To assess the practicality of MVGs for engineering applications, the thrust loss is computed for the MVG configurations of this study by applying the integration of

$$Thrust = \oiint (p - P_\infty + \dot{m}u)\, ds$$

to the LES data at the nozzle exit plane. For this integration, p is the instantaneous static pressure, P_∞, and $\dot{m}$ is the instantaneous flow rate ρu, where ρ is the density and u is the axial velocity. The thrust is averaged over time and the thrust loss coefficient for a given MVG nozzle is computed as

$$C_{Thrust} = \frac{Thrust_{MVG} - Thrust_{baseline}}{Thrust_{baseline}}$$

and is shown in Table 3-1 for the overexpanded conditions NPR=2.7, 3.0, and 3.5, and for the design condition (NPR=4.8). It can be seen that the MVG nozzles thrust loss coefficient is somewhat stable for NPR = 3.0 - 4.8. The thrust losses induced by the single-array MVGs is within 1.5% at the design or cruise condition, which thrust performance is most critical. However, the thrust losses of the double-array MVGs are much higher and thrust performance improvement is needed.

Table 3-1: MVG thrust loss coefficient.

MVG \ NPR	2.7	3.0	3.5	4.8
Single Array MVG	-2.38%	-1.52%	-1.64%	-1.48%
Double Array MVG	-6.5%	-5.5%	-5.3%	-4.4%

Baseline nozzle internal flow

Figure 3.1 shows fluorescence surface oil flow visualization of the internal nozzle flow and LES contours of axial velocity of a cross-section Z-Y plane at the nozzle exit plane and the instantaneous Mach number contours in X-Y plane containing the nozzle centerline and the middle of a seal surface at NPR=2.7 for baseline nozzle Figure 3.1(a) and single array MVG nozzle Figure 3.1(b). The surface oil flow visualization highlights the surface imprint of the flow topography and features. Due to the slow response time of oil flow compared to the nozzle flow dynamics, the patterns observed are qualitative representations of the internal nozzle surface mean flow features. In Figure 3.1(a), the oil flow indicates a recirculation region forming on every seal surface towards the baseline nozzle lip. This separated region can also be seen in the Z-Y plane cross-sectional contour plot and the instantaneous LES flow field at the X-Y plane. A clear flow separation from the nozzle wall upstream of the nozzle lip can be seen, and this consequently generates an oblique shock initiated upstream of the nozzle lip along with the separated flow region. This reverse flow region indicates flow separation as the incoming flow encounters adverse pressure gradients of the expanding flow where the forces exerted by the ambient pressure near the nozzle exit is higher than the local flow momentum and pressure at the separation point.

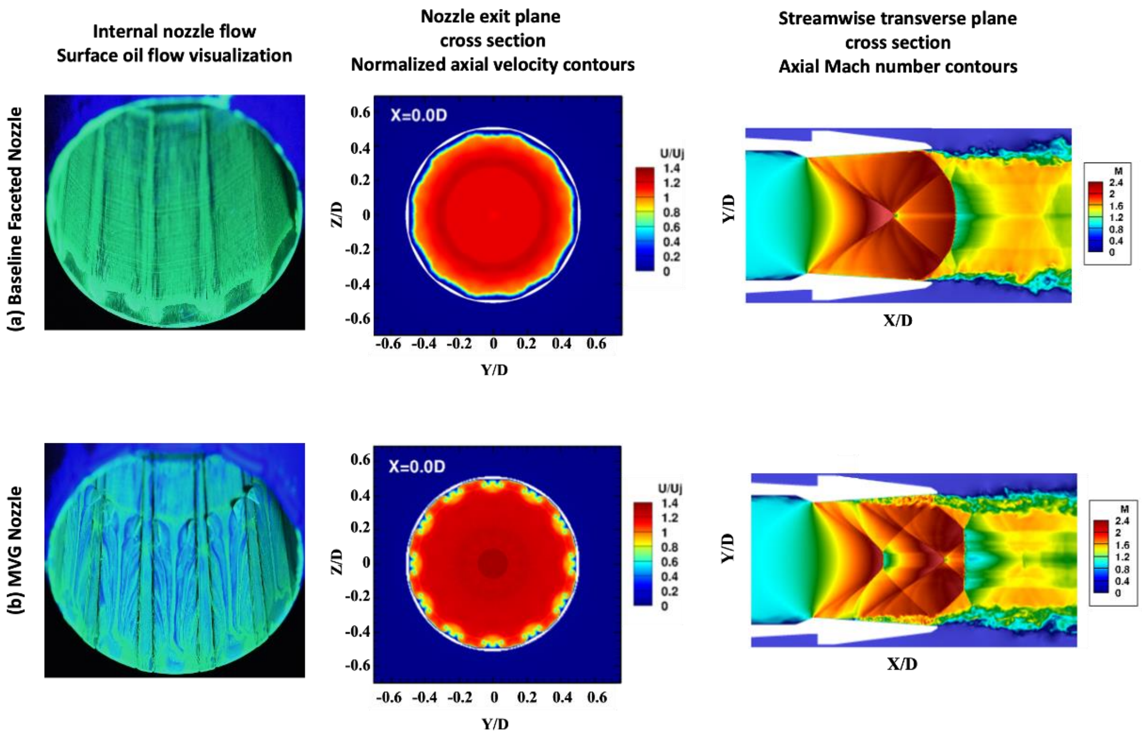

Figure 3.1: Fluorescence surface oil flow visualization giving qualitative information of flow imprint on wall resulting from flow exerting wall shear stresses (left column), LES axial velocity contours in Y-Z cross section at nozzle exit plane (middle column), and axial Mach number contours in X-Y plane (right column). The operating condition is NPR=2.7 for: a) Baseline Faceted (top row), b) Single array MVGs (bottom row). Oil visualization and LES are used to demonstrate the impact of MVGs on the Nozzle lip separation size, the generation of oblique shocks and the generation of streamwise counter-rotating vortices. (LES contours from Liu et. al.[9]).

Impact of MVGs on the nozzle internal flow

The surface oil flow visualization of the optimal single array MVG nozzle configuration is shown in Figure 3.1(b) and the corresponding mean axial velocity contour in Z-Y plane at the nozzle exit and the instantaneous LES Mach number at the X-Y plane passing through the nozzle centerline and the midplane between two MVG blades. This figure clearly shows how MVGs change the internal nozzle flow and internal shock waves. The oblique shock waves generated at the MVG blades interact with the throat shock waves and cause a large Mach disk inside the nozzle at X/D=-0.4. This forms a triple point of a lambda shock system where the trailing shock impinges and reflects off the nozzle wall and forms a strong and large Mach disk slightly downstream of the nozzle exit. This strong and large Mach disk reduces the jet core flow velocity and weakens shock cell structures in the jet plume, this in turn impacts the shock-associated noise radiation component of the far-field acoustics. Additionally, as the formed counter-rotating vortices convect in the downstream direction, they interact with the shear layer and impact the initiation and formation of the large turbulent structures, and eventually affect the turbulent mixing noise component radiating to the downstream direction of the far-field acoustics as will be discussed later. Figure 3.2 shows comparisons of the internal surface flow and a closeup view of the flow features for single array MVG Figure 3.2(a) and (b) and for double array MVG nozzles Figure 3.2 (c) and (d). The leading edges of the MVG blade pairs interact with the incoming flow and generate oblique shocks due to double fin interaction with supersonic flow Figure 3.2 (b), this results in shock wave turbulent boundary layer interactions that cause flow separation upstream of the fins and originating at the fin root leading point. The foot of the oblique shock wave of the MVG fin flow separation can be seen from the surface flow originating at the root of the MVG blades in the upstream incoming flow. As the flow approaches the fin blades of the MVGs, a pressure gradient is formed between the upstream and downstream blade surfaces, this induces the flow to swirl around the MVG blades and introduces angular momentum on the flow causing the formation of two counter-rotating streamwise vortices that convect in the downstream direction. The region depleted of oil Figure 3.2 (b) indicates the interaction of the lower portion of these newly formed counter-rotating vortices with the nozzle wall that can be seen in the surface oil flow visualization forming at the trailing edge of the fin blades, causing a swirl motion of the nozzle surface flow convecting in the downstream direction and energizing the wall boundary layer as the newly formed vortices transfer momentum from the high-speed nozzle flow regions to the nozzle wall flow regions. This increase in boundary layer flow energy allows the flow to delay the nozzle lip separation point and reduces the size of the separation region at the nozzle lip. This observation is also confirmed in the Z-Y plane cross-section axial velocity contour plot at the nozzle exit plane shown in Figure 3.1(b), where the flow separation region near the nozzle wall is diminished. On each seal surface of the nozzle wall, an upwash flow region can be seen forming at the center between two MVG blade pairs, and a downwash flow region forming in the region between two neighboring MVG pairs on different seal surfaces, Figure 3.2(a). The downwash flow inside the nozzle is responsible for energizing the boundary layer and delaying flow separation as can be seen in the streaks formed on the oil flow visualization.

One of the benefits of adding MVGs inside the nozzle is the momentum transfer into the nozzle wall boundary layer causing a substantial reduction in the nozzle lip separation region. This effect could be utilized to add a second row of larger MVGs to introduce much stronger and larger streamwise vortices with the goal of enhanced shear layer mixing and accelerated jet flow dissipation outside the nozzle. The second array of MVGs can also introduce additional oblique shock waves that interact with the Mach disk and shock cell structure which can reduce the jet core velocity even further, having additional noise reduction benefits. Since the separation region is reduced due to the upstream row of the MVGs, the second row of MVGs could be placed downstream up to the nozzle lip. Due to the complex interaction of both upstream and downstream MVG arrays with the nozzle flow, another parametric study was carried out for two array MVG configurations (not shown) for operating conditions relevant to overexpanded jet flows at takeoff conditions, and it was found that the optimal location for the second row of MVGs is X/D= 0.3 upstream of the nozzle's exit plane. We present here only the configuration with the optimal noise reduction gains for the relevant operating conditions. The surface oil flow visualization of the two-array MVG nozzle is shown in Figure 3.2(c) and (d) showing similar trends observed for the single-array MVGs discussed earlier, but with the added benefit of stronger vortices and a much smaller flow separation region near the nozzle lip.

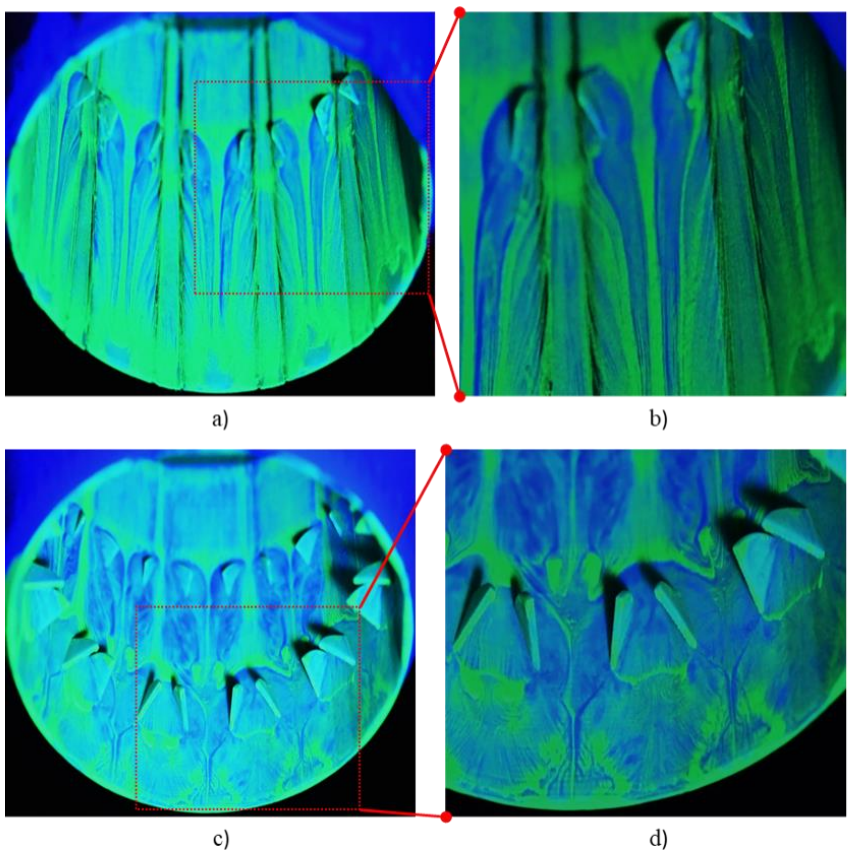

Figure 3.2: Fluorescence surface oil flow visualization at NPR=2.7 for: (a,b) Single array MVGs, and (c,d) Double array MVGs. Flow direction from top to bottom.

MVG IMPACT ON FLOW FIELD IN THE JET PLUME

Validation between PIV and LES predictions

Axial velocity distributions and centerline axial velocity profiles at NPR= 2.7, 3.0, and 3.5 are shown in Figure 3.3, Figure 3.4, and Figure 3.5 for the faceted baseline, single array, and double array MVG nozzles respectively. The PIV measurements are shown in the top half of each contour plot and LES predictions are shown in the bottom half. Also, the centerline axial velocity profiles are shown for both PIV and LES. It should be noted that LES predictions are made at the cold jet condition with NTR=1.0, whereas PIV measurements are made at NTR=1.05 to minimize condensation effects that can cause measurement errors from spurious vectors. However, the velocities from each data set are normalized with their respective isentropic exit velocity at each condition.

Overall, the axial velocity distribution results show good agreement between PIV and LES for the various nozzle configurations across all NPRs. For example, this agreement can be seen in Figure 3.3 of the baseline nozzle, where the shock cell spacing, jet potential core lengths, and shear layer spread all show a good match. The match in PIV and LES is also clearly seen in the centerline axial velocity profiles. A difference in peak magnitudes is observed across large velocity gradients, for example after the Mach disk outside the nozzle exit, as well as the maximum value of the first shock cell at NPR=3.5. This difference is expected due to the combined effects of lower vector spatial resolution of PIV data compared to LES as well as the relaxation time of tracer particles in PIV having a lag across sudden velocity changes at velocity maxima and minima. Another difference is seen in the region downstream of the end of the potential core where PIV measurements show slightly lower velocities compared to LES.

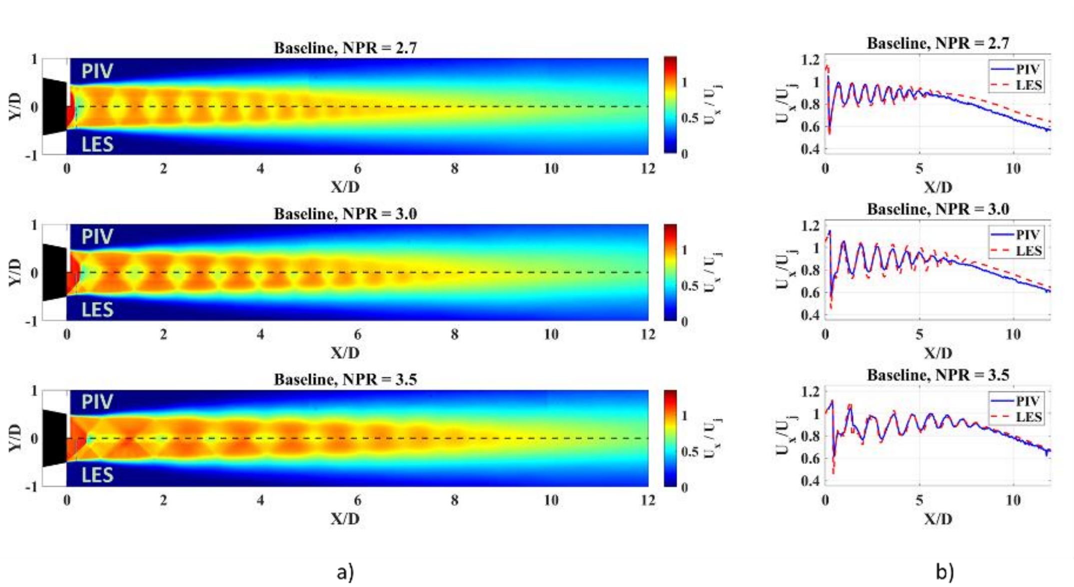

Figure 3.3: a) Axial velocity distributions and b) centerline axial velocity profiles of the faceted baseline nozzle at NPR=2.7, 3.0 and 3.5. Measurement plane is the middle of a seal surface. The velocity is normalized by the jet velocity at the fully expanded condition. Top half is PIV measurement and bottom half is LES prediction.

This velocity difference becomes smaller with increasing NPR and is seen for all nozzle configurations. The end of the potential core velocity differences between PIV and LES is attributed to temperature effects for the different NTR values and selecting the exact centerline location of the lower PIV vector resolution compared to the higher resolution LES vectors. Another explanation is due to the smaller size nozzle used for the PIV measurements with exit diameter of 1.45-inch. The flow path into this nozzle undergoes a sudden change in plenum diameter upstream of this nozzle and causes an increase in flow turbulence intensity. At the highly overexpanded conditions, the nozzle wall separation is more sensitive to the high turbulence levels of the flow.

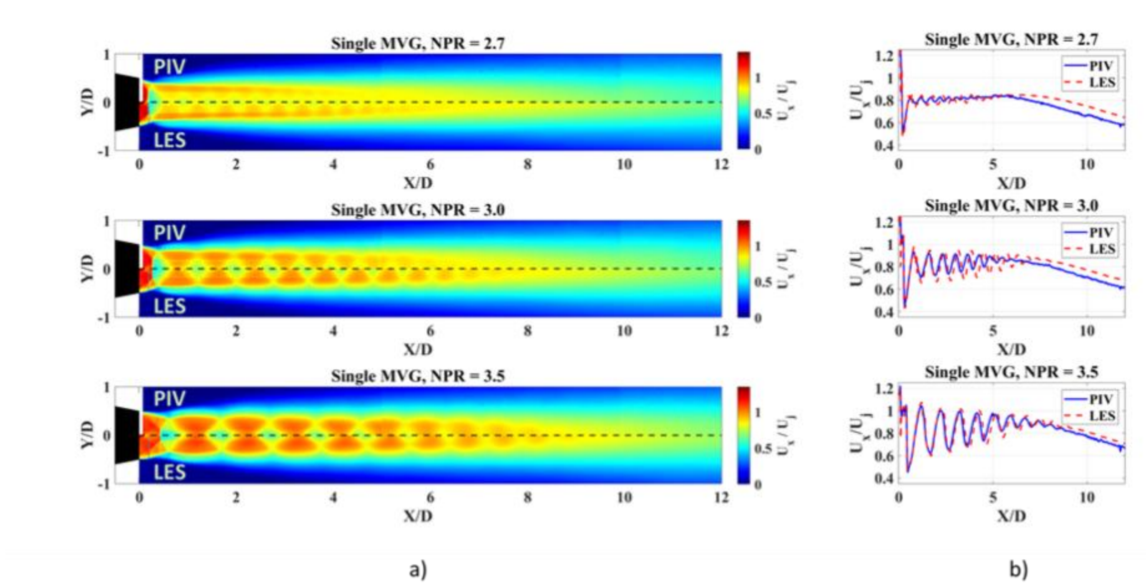

Figure 3.4: a) Axial velocity distributions and b) centerline axial velocity profiles of the single array MVG nozzle (MVGa90b36) at NPR=2.7, 3.0 and 3.5. Measurement plane is the middle of a seal surface between two VG blades. The velocity is normalized by the jet velocity at the fully expanded condition. Top half is PIV measurement and bottom half is LES prediction.

As the NPR increases, the nozzle lip separation region becomes smaller and its oscillations becomes more resistant to incoming flow turbulence leading to better agreement with centerline velocities of the LES simulations. Another difference between PIV and LES can be seen in the screeching jet condition of NPR=3.0. Where the rapid dissipation of the centerline shock cells after the fourth shock cell beyond X=4D, whereas LES prediction shows the persistence of the shock cell strengths for the same region. This difference between the results is attributed to the higher screech intensities observed in the experiment measurements compared to those predicted by LES and will be discussed in the acoustic far-field section. The higher-intensity screech tones generated in the experimental setup would cause stronger shock cell oscillations that would reduce the jet's core length and

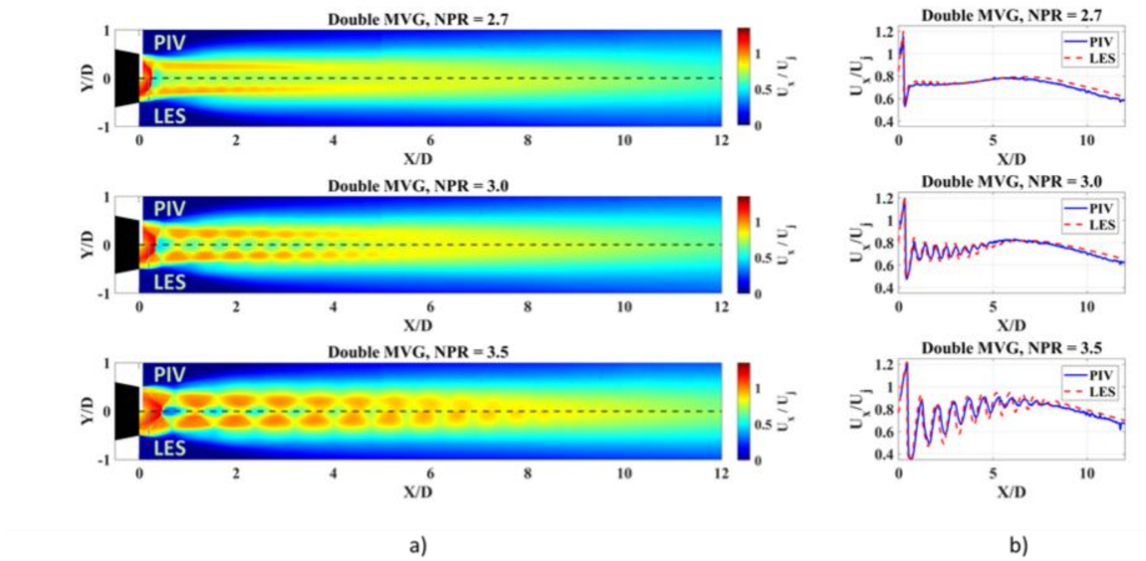

Figure 3.5: a) Axial velocity distributions and b) centerline axial velocity profiles of the double array MVG nozzle (2ArrayT) at NPR=2.7, 3.0 and 3.5. The measurement plane is the middle of a seal surface between two VG blades. The velocity is normalized by the jet velocity at the fully expanded condition. Top half is PIV measurement and bottom half is LES prediction.

diminish the strength of their respective shock cells due to a smearing effect of taking the flow-field average.

Turning our attention to axial velocity distributions of the single array MVG nozzle comparisons in Figure 3.4. It can be seen that the overall agreement between PIV and LES is good, but with the exception that the shock cell spacing shows some mismatch in the downstream jet plume near the end of the jet core at lower NPRs. This shock-cell spacing mismatch appears to be much less at higher nozzle pressure ratio of NPR=3.5 between PIV and LES prediction. In addition, the experiment data also presents a faster decay of the shock cells in the downstream jet plume region than LES predictions at lower NPRs. The cause of these differences between PIV measurements that use a smaller nozzle size of 1.45

inch and LES predictions that use a larger nozzle size of 3.16 inch is not clear so far and require a further investigation.

Effects of MVGs on the shock-cell structure in the jet plume

Single-array MVGs:

To assess the effects of MVGs on the jet plume, we start by comparing the flow field differences between the baseline nozzle in Figure 3.3 and the single array MVG nozzle in Figure 3.4. Also, the PIV centerline velocity profiles of the different jets are plotted together to aid direct comparisons in Figure 3.6.

A few observations can be made from this comparison. The strength of the large Mach disk at the nozzle exit at NPR = 2.7 is increased as shown in the centerline profiles, where the baseline at NPR=2.7 have a velocity drop across the Mach disk from u/U_j =1.15 to 0.6, whereas the drop for the single array MVG nozzle across the nozzle exit Mach disk is from u/U_j=1.35 to 0.5. This larger drop in velocity across a normal shock wave indicates that the Mach disk became stronger. This stronger Mach disk reduces the velocity magnitude and its spatial fluctuations in the jet core. For example, the MVG nozzle presents a jet core velocity averaged around u/U_j=0.8 but the baseline centerline velocity fluctuating between u/U_j = 0.8 and 1.0. Thus, there is a roughly 10\% averaged velocity drop in the jet core. The contour plot shown in Figure 3.4(a) at NPR = 2.7 presents an inverted velocity profile pattern, which could be beneficial to the far-field noise reduction[102,103]. In addition, the small fluctuations of the jet velocity of the single MVG nozzle results indicate the weakening of the shock cell strengths. It will be discussed later in the acoustics section that this effect causes a large reduction in the peak BBSN noise component by roughly 12dB in the far-field acoustics at the sideline observation angle of 90 degree in Figure 3.19(a).

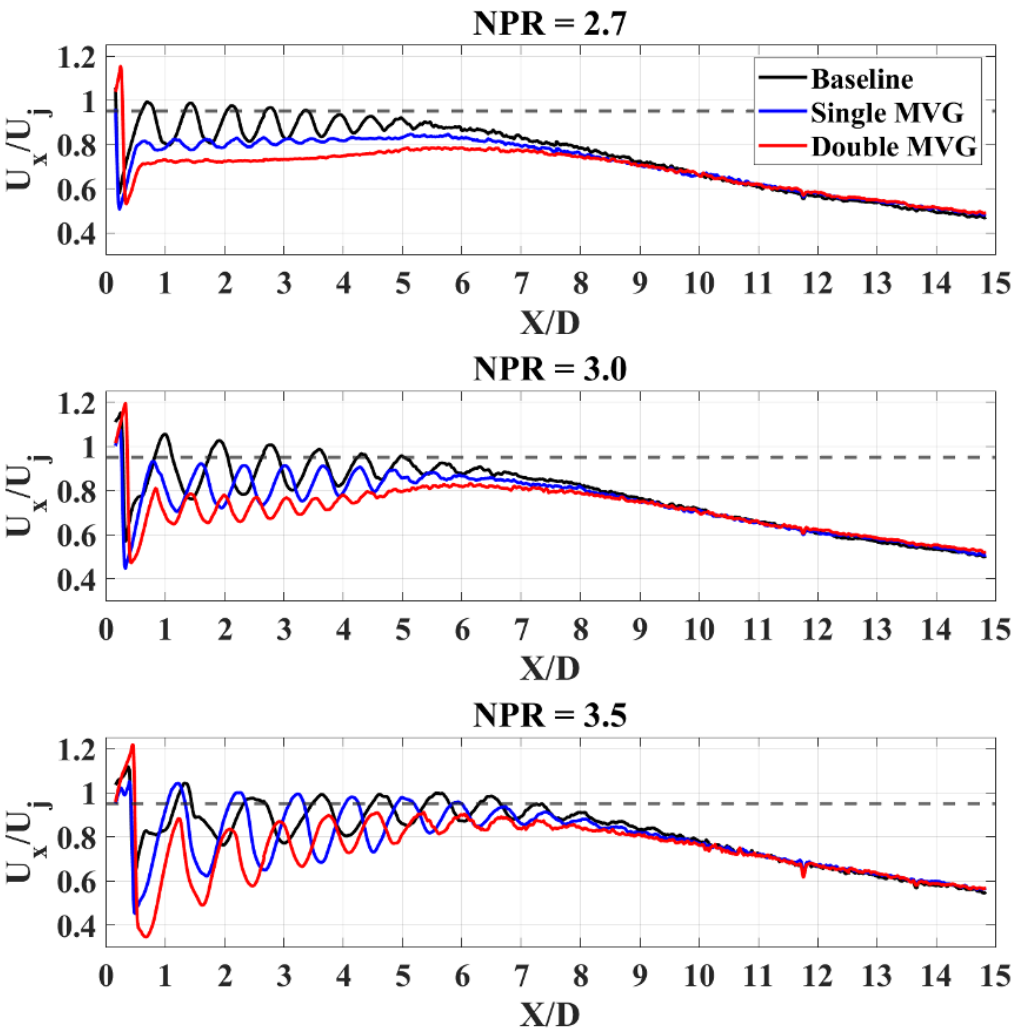

Figure 3.6: PIV comparisons of the centerline axial velocity distributions for the different jet configurations at NPR=2.7, 3.0, and 3.5. The measurement plane is the middle of a seal surface between two VG blades. The velocity is normalized by the jet velocity at the fully expanded condition.

In addition, the shock-cell spacing is also reduced by the single-array MVGs. This results in more shock cells than those observed in the baseline jet. The single-array MVG jet presents 10 shock cells for an axial distance up to X=5D at NPR = 2.7, but the baseline jet presents only 8 shock cells for a similar axial range at NPR = 2.7, Figure 3.6. These changes on the shock cells would result a peak BBSN frequency shift to a higher Strouhal number.

A similar trend can be seen at NPR=3.0. For example, this is also a roughly 10\% drop of the spatially averaged centerline velocity and the shock-cell strength and spacing are reduced by MVGs. The baseline jet shows 6 shock cells between the nozzle exit and the axial location of X=5D at NPR=3.0, whereas the single array MVG nozzle shows about 7 shock cells for the same NPR.

As the NPR increases to 3.5, this trend becomes somewhat different. The spatially averaged centerline velocity is reduced by MVGs, but the velocity spatial fluctuation is increased by MVGs. This indicates that MVGs have actually increase the shock-cell strength. This observation indicates that the axial location of 0.65D upstream of the nozzle exit may not be effective for higher NPRs. The axial location effect investigated by Liu et al.[85] shows that a further downstream location could be better suited for the higher NPRs. This highlights the importance of selecting the appropriate design parameter of axial location inside the nozzle for MVG placement to appropriately tailor the interaction of the MVG fin-generated oblique shock waves with the jet shock cells to achieve the desired noise reduction profile of the BBSN noise component for specific NPR operating conditions.

Double-array MVGs:

The double array MVG nozzle's axial velocity distributions of both PIV and LES are shown in Figure 3.5. A good match can be seen between PIV and LES for velocity fluctuations caused by the shock cells, shock cell spacing, and the overall velocity distributions for all NPRs. For NPR=2.7 the velocity variations across the weak shock cells are slightly lower than the LES predictions, and this probably is due to the limitation of lower PIV resolution from capturing the weaker shock cell variations.

Examining the effect of the double array MVG nozzle on the flow field, it is interesting to see that a much stronger Mach disk is formed downstream of the nozzle exit and causes a slow jet core surrounded by an annulus of higher speed flow that separates the core region from the shear layer. This inverted velocity profile has been already observed for NPR=2.7 in Figure 3.4, but the double-array MVGs produce a stronger inverted velocity profile. This indicates that the double-array MVGs generate stronger oblique shock waves because the Mach disk is formed by the converging of the two oblique expansion waves near the nozzle exit. Increasing the NPR from 2.7 to 3.0 and 3.5, it can be seen that the Mach disk size is reduced, and the radius of the lower-speed core region is also reduced. It should be noted that this annulus region surrounding the lower-speed jet core is not a perfect circle (not shown here) due to the presence of the shock cells. but instead has a corrugated shape due to the interaction of neighboring streamwise vortices causing inward fluid entrainment into the jet in the upwash region between each pair of MVG blades, and also, an outward fluid ejection of the jet flow into the ambient in the downwash region of neighboring blade pairs on different nozzle seal surfaces. The momentum energy of this high-speed annular flow would dissipate as the flow travels in the downstream direction, this momentum energy dissipation would transfer energy radially outward energizing the outer shear layer, as well as radially inward towards the jet core. This in turn increases the flow energy in the jet core causing an acceleration of the jet centerline velocity from the location of the Mach disk to the axial location near X=5.5D, after which the centerline velocity decays and slows down. This can be observed along the centerline for all NPRs in Figure 3.5. It is clear that this inverted velocity profile would enhance mixing and increase the noise reduction as shown in Tanna's work[102,103].

The Mach number distribution (not shown) generated by the double array MVG nozzle at NPR=2.7 indicates that Mach number downstream of the Mach disk has become subsonic except the high-speed annular region. On the other hand, the subsonic region generated by the single-array only limited to a few small spots associated with the compression shock waves in the jet plume. It is expected that the shock-associated noise would be much lower than that of the baseline jet and the jet generated by the single-array MVGs. This is a result of the combined interaction of the oblique shocks generated by the upstream and downstream MVG arrays of this nozzle configuration with the jet plume. At the higher-pressure conditions of NPR= 3.0 and 3.5, the reductions of the jet core velocity are also substantial although the reductions are less than that at NPR = 2.7. The peak centerline velocities of the shock cell structures are around u/Uj=0.8 and 0.9 for the double array MVG nozzle, which are reductions of 20\% and 10\% from the baseline nozzle at NPR= 3.0 and 3.5 respectively, see Figure 3.6. In addition, the shock-cell sizes are further reduced by the double-array MVGs. For example, Figure 3.6. shows that the double array MVG nozzle contains about 9 shock cells in the region between the nozzle exit and downstream axial location of X=5D, whereas the single-array MVGs present 7 shock cells and the baseline nozzle contains 6 shock cells in the same region. A similar trend can be seen for the shock cell spacing at NPR=3.5 between the double array MVG and the baseline nozzle. This reduced shock-cell size would expect a peak frequency shifting to higher frequencies.

MGV effects on transverse velocities and entrainment of ambient fluid

The MVG nozzles generate streamwise counter-rotating vortices that interact with the shear layer and induce a corrugated jet cross-sectional shape compared to a circular cross-sectional jet shape for the baseline nozzle as shown in Figure 3.7.

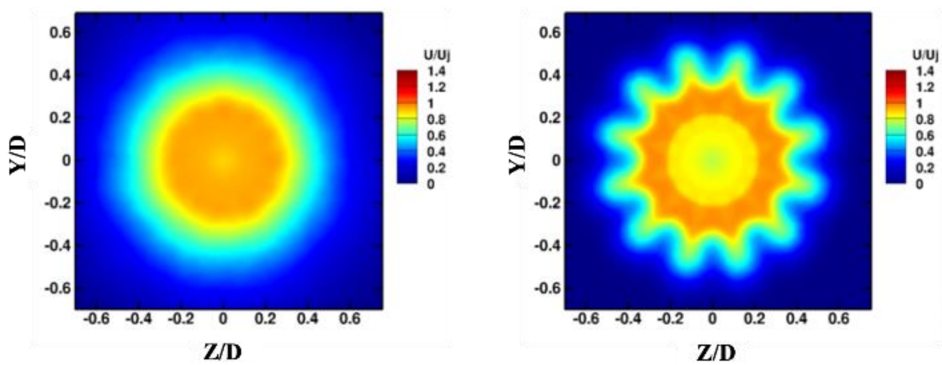

a) b)

Figure 3.7: LES axial velocity contours at downstream axial location X=3D for NPR = 2.7. a) baseline, and b) single array MVG nozzle. velocities are normalized by the fully expanded jet condition. (LES from Liu et. al.[9])

The regions between the blades of each MVG pair will cause radially inward entrainment of the ambient fluid into the shear layer, whereas the regions in-between neighboring MVG pairs will cause radially outward fluid ejection from the shear layer into the ambient. In the current study, the PIV measurement plane passes through the regions in between the MVG blade pairs and the jet axis, and will only detect the radially inward entrainment mechanism from the ambient to the shear layer.

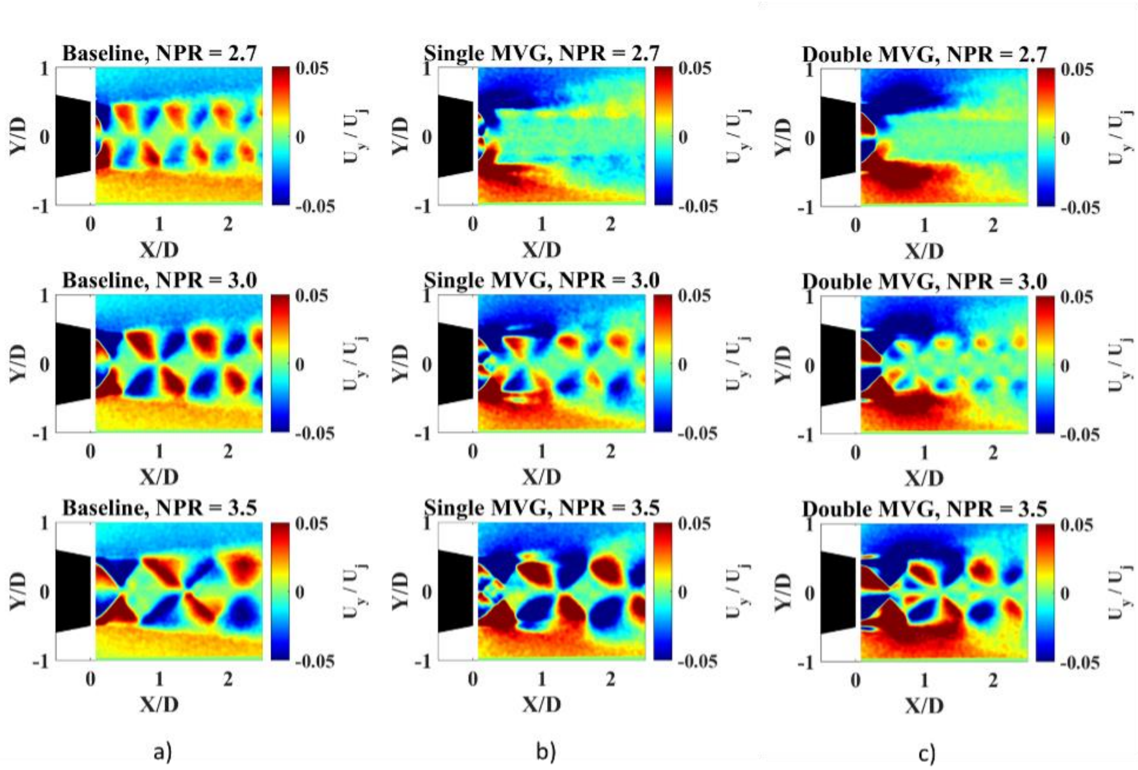

Figure 3.8: Transverse velocity distributions at NPR=2.7(first row), 3.0 (second row) and 3.5(third row). Measurement plane is the middle of a seal surface. The velocity is normalized by the jet velocity at the fully expanded condition. Data shown is from PIV measurement for nozzles: a) baseline (left column), b) single array MVG (middle column), and c) double array MVG (right column).

Transverse velocity distributions from PIV measurements for the baseline, single array MVG, and double MVG nozzles at various NPRs are shown in Figure 3.8(a), (b), and (c). These distributions highlight the level of ambient fluid entrainment towards the radially inward direction along the shear layer in the current PIV measurement plane. Values of the radially inward entrainment velocities are extracted at various radial distances from the centerline, Y/D= 0.6, 0.8, and 1.0 are presented in Figure 3.9. It can be seen for the baseline nozzle that a mild entrainment of the ambient fluid along the shear layer occurs. For the single array MVG nozzle, the counter-rotating streamwise vortices enhance the entrainment process and increase its intensity in the near nozzle exit region. This effect becomes even stronger for the double array MVG configuration. Examining the entrainment profiles at different radial distances in Figure 3.9, a clear trend emerges showing the increase in negative velocities representing radially inward flow towards the shear layer. For example, the maximum entrainment velocity at NPR = 3.0 near the nozzle exit has a peak magnitude value of roughly -0.025, -0.045, and -0.065 at a radial distance of Y/D=0.6 for the baseline, single-array MVG, and double-array MVG nozzles, respectively. It is clear that the vortices generated by MVGs enhance the mixing in the shear layer.

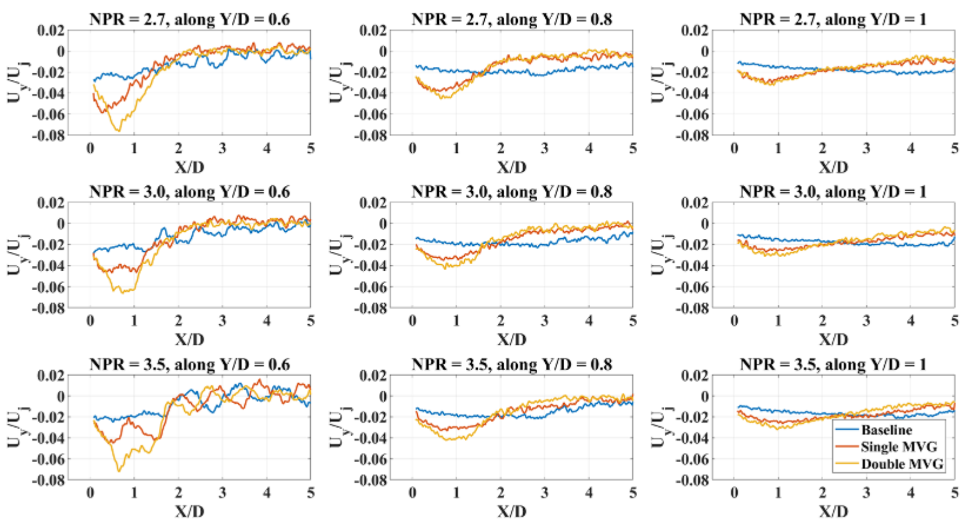

a) b) c)

Figure 3.9: Comparison of the transverse velocities of the various nozzle configurations along axial direction at radial locations Y/D= : a) 0.6 (left column), b) 0.8 (middle column), and c) 1.0 (right column), at NPR = 2.7 (first row), 3.0 (second row), and 3.5 (third row).

MVG effects on Vorticity

The corrugated cross-sectional shape of the MVG jets discussed earlier are driven by the interactions of streamwise counter-rotating vortices convecting along the jet shear layer with both the jet and the ambient fluid. The persistence of the counter-rotating streamwise vortices generated by the MVG blades are highlighted in the LES cross-section views at various downstream axial locations shown in Figure 3.10. It can be seen that near the nozzle exit at X/D= 0.5 the generated vortices have small size and high vorticity intensity. As the flow reaches X/D=1.0, the vorticity sizes have grown and stretched radially due to interactions with neighboring vortices and a reduction of the vorticity intensity occurs. Further downstream at X/D = 2.0 the streamwise vorticity is significantly reduced and their dissipation takes place. This is expected as the angular momentum of the streamwise vortices is dissipated due to the entrainment process as well as their interaction with neighboring vortices.

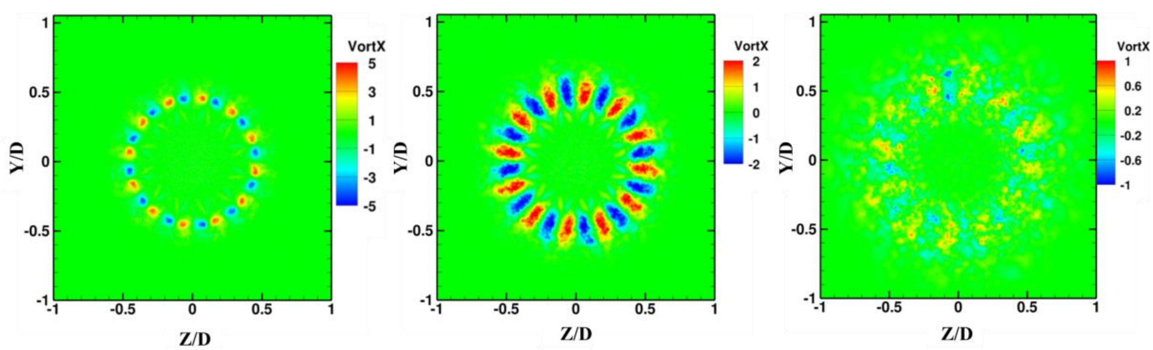

a) b) c)

Figure 3.10: LES axial vorticity contours of the single array MVG nozzle at NPR= 2.7 at axial locations a) X/D = 0.5 , b) X/D = 1.0 , c) X/D = 2.0. The vorticity is normalized by Uj/D. (LES from Liu et. al.[8])

Since the spanwise vorticity distribution represents the impact of the MVGs on the shear-layer development, this flow quantity is investigated and its distributions of both the baseline and MVG modified jets are shown in Figure 3.11. In each of the plots, the vorticity is perpendicular to the plane containing the 2D-PIV velocity field and shows a close-up view of the upper shear layer overlaid with path lines of the velocity field to highlight the entrainment of the ambient fluid into the shear layer.

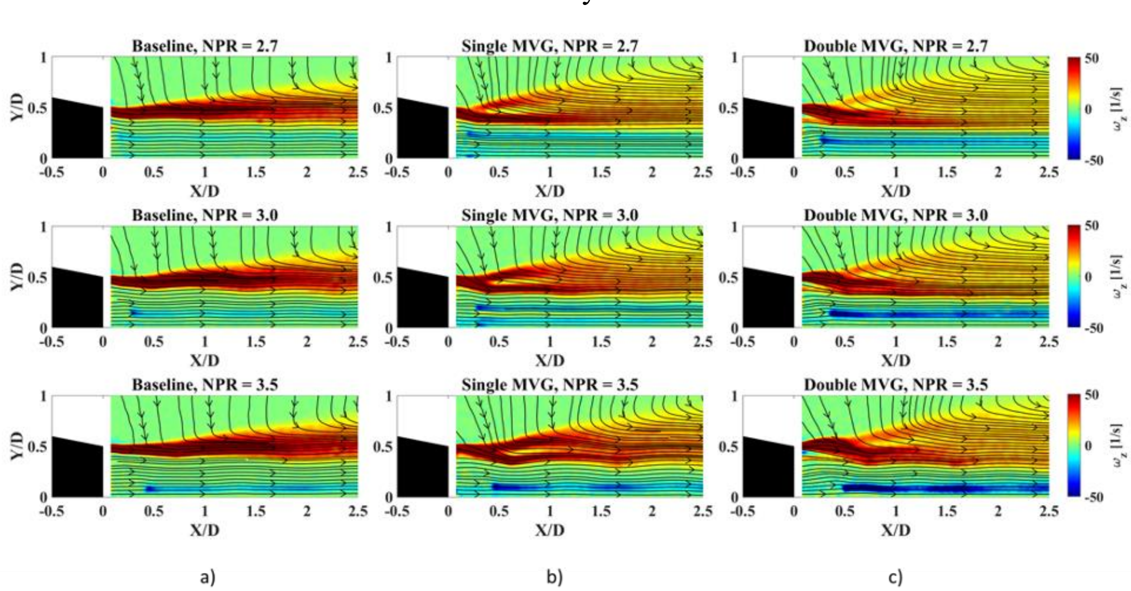

Figure 3.11: Spanwise vorticity distributions for: a) baseline (left column), b) single array MVG (middle column), and c) double array MVG nozzle (right column). nozzle at NPR=2.7, 3.0, and 3.5. The measurement plane is in the middle of a seal surface. The vorticity is normalized by the jet velocity at the fully expanded condition and the nozzle diameter. The data shown is computed from PIV measurement.

The baseline nozzle in Figure 3.11(a) shows a high level of spanwise vorticity peak in the near lip region and gradually reduces in the downstream direction as the shear layer spreads. This high-intensity vorticity is driven by the strong velocity gradients across the shear layer between the jet core flow and the almost quiescent ambient fluid. This spanwise vorticity interaction draws in the ambient fluid into the shear layer and the mixing process allows the shear layer to spread and as a result reduces the velocity gradient across it in the downstream direction. This mechanism is also responsible for the formation of large coherent structures in the downstream region around the end of the potential core, where high-intensity low-frequency turbulent mixing noise is generated and radiates to the far field at downstream observation angles.

The vorticity distributions of the MVG nozzles are presented in Figure 3.11(b) and Figure 3.11(c). MVGs introduce counter-rotating vortices, which convert some of the axial momentum energy of the jet plume into angular momentum energy in the shear layer. It should be pointed out that the current PIV plane is in the downwash region of vortices generated by MVGs. The angular momentum of the streamwise vortices induces a downwash flow momentum in the measurement plane, transferring the ambient fluid radially inwards to the shear layer. The distributions by the double-array MVGs present a larger shear layer spread with lower vorticity intensities in the slightly further downstream region due to the increased mixing introduced by the stronger streamwise counter-rotating vortices generated by the MVG blades of this configuration.

It is interesting to see the high-intensity vorticity levels leaving the nozzle lip and bifurcating into a two-prong structure starting to form around X/D=0.5 downstream of the nozzle exit plane for both MVG nozzle configurations in Figure 3.11(b) and (c). The inner region of this prong structure should present the shear layer adjacent to the high-speed jet core, while the outer part is a combination of the coalescence of the two counter-rotating streamwise vortices and their interaction with the entrained ambient fluid by the downwash momentum. Thus, this bifurcating feature would only occur in the region where the vortices are strong.

This spanwise vorticity intensity should vary inversely with the shear-layer spread rate because of its definition when the axial velocity gradient is the dominant component.

$$\omega_z = \frac{dv}{dx} - \frac{du}{dy}$$

When the flows get out of the nozzle, they present similar intensity levels across the initial thin shear layer in all jets, as shown in the region from the nozzle lip to X=0.25D. As the flow travels in the downstream direction, it can be seen that the baseline nozzle maintains a thin shear layer with a high-intensity spanwise vorticity distribution across the shear layer. This high intensity slowly decays as the shear layer spreads slowly in the downstream direction Figure 3.11(a). The single array MVG nozzle exhibits an accelerated shear layer spread with a reduction in the spanwise vorticity intensity distribution in the downstream direction, having the high-intensity vorticity magnitudes closer to the faster flow of the jet core and the low-intensity magnitudes closer to the ambient fluid Figure 3.11(b). The double array MVG nozzle continues this trend with further reduction in spanwise vorticity magnitudes towards the outer edges of the accelerated shear layer spread where ambient fluid entrainment, depicted by the flow path lines, enhances this effect Figure 3.11(c). As will be discussed later in the TKE section, the rapid spanwise vorticity intensity dissipation due to the larger shear layer spread is also the mechanism causing the rapid TKE reductions for the MVG nozzles observed in Figure 3.13, where the mixing of high momentum shear layer with the low momentum entrained fluid causes an overall kinetic energy reduction of the resulting mixed shear layer, hence a reduction in TKE intensities along the shear layer.

The generation of the streamwise vortices combined with the reduction in spanwise vorticity intensity along the shear layer in the near nozzle region is expected to impact the mechanism of the formation of the large coherent structures and would reduce their convection velocities.

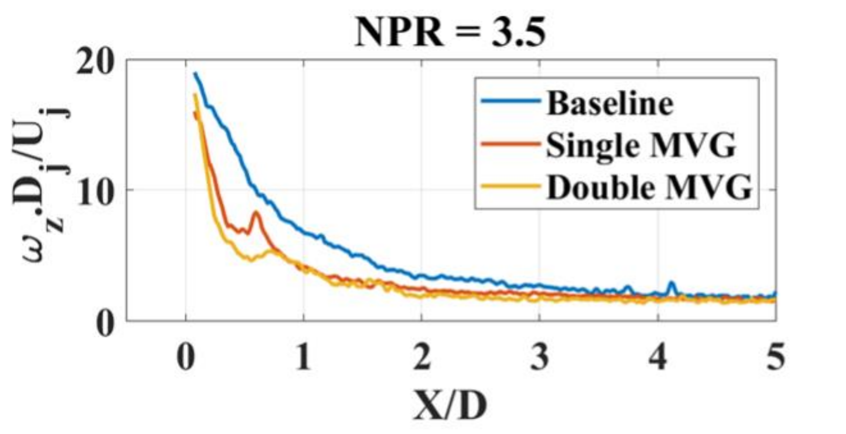

Figure 3.12: Comparison of the maximum spanwise vorticity distribution from PIV along the axial direction for various nozzle configurations at NPR= 3.5.

Figure 3.12 shows the maximum spanwise vorticity within the shear layer along the axial direction for all nozzle configurations at NPR=3.5 for brevity, since the other NPRs follow the same trend. It can be clearly seen that the peak vorticity values are reduced for the single array MVG nozzle compared to that of the baseline, and further reduction is obtained for the double array MVG nozzle. Since the nozzle core flow energy is distributed across two components of vortices, spanwise and streamwise vortices, it is expected that the intensity levels of spanwise vorticity for nozzles implemented with MVGs would be lower than that of the baseline nozzle flow. Examining the maximum spanwise vorticity plot in Figure 3.12 along with the entrainment plots in Figure 3.9 for NPR=3.5 appears to show that the maximum ambient fluid entrainment occurs in the region that has the rapid reduction of the maximum vorticity from the nozzle exit to first minima at around X=0.6D and 0.75D for the single array and the double array MVG nozzles, respectively. This shows that the spanwise vorticity reductions are a result of mixing with the ambient fluid entrainment that are greatly increased by the streamwise counter-rotating vortices of the MVG blades and this is responsible for a rapid shear layer spread.

MGV effects on Turbulent Kinetic Energy (TKE)

The turbulent kinetic energy distributions of the fluctuating velocity field for the baseline, single-array MVG and double-array MVG nozzles at three NPRs for a plane containing the jet centerline and the midpoint of a seal surface are shown in Figure 3.13. In each contour plot, the top half is for PIV and the bottom half is for LES. Again, both PIV measurements and LES predictions show a good agreement for the shear layer spread and the high-intensity distributions within the shear layer for all jets at the three NPRs. For the baseline nozzle at NPR=3.0, the LES prediction shows lower TKE intensities compared to the PIV measurements. It will be shown in the acoustics section that the NPR = 3.0 is a highly screeching condition and the screech intensities predicted by LES are slightly lower than those shown in laboratory measurements. This indicates that the screech tones in laboratory measurements are stronger and would cause larger perturbations to the jet plume, increasing the TKE levels. MVGs have increased TKE from the nozzle exit up to x = 2D, but reduce TKE further downstream. The increase of TKE near the nozzle is due to the interaction between the vortices and the shear layer. The impact on TKE is stronger in the jet generated by the double array MVG nozzle. The higher intensities are localized in the near nozzle region up to X/D=2 and a substantial TKE intensity decrease can be observed further downstream.

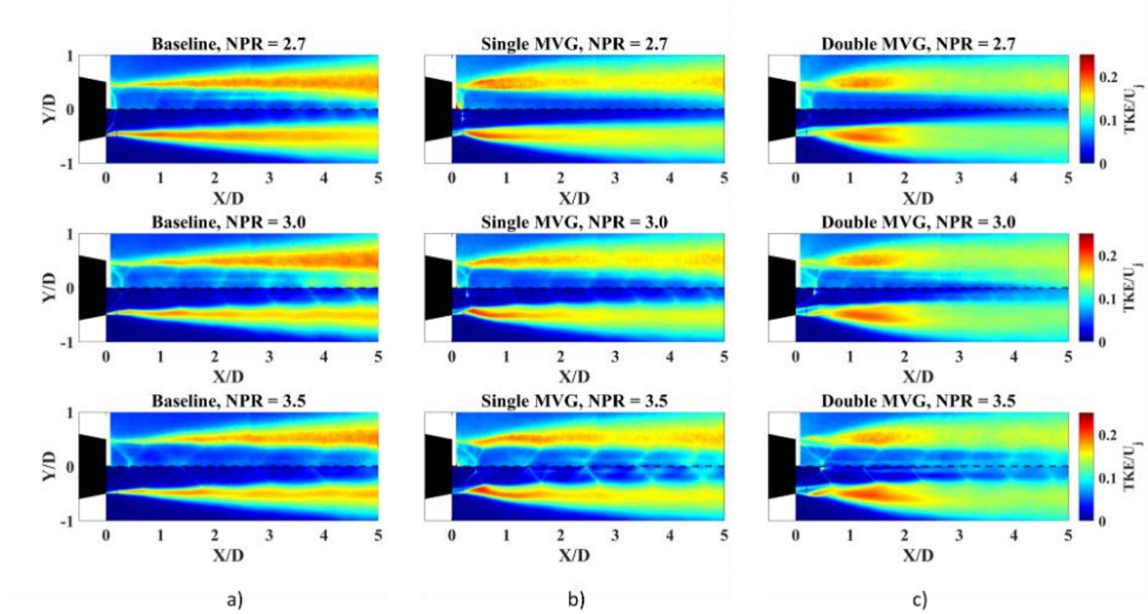

Figure 3.13: Turbulent Kinetic energy distributions for: a) baseline (left column), b) single array MVG (middle column), and c) double array MVG nozzle (right column). The nozzle pressure ratios are NPR=2.7 (top row), 3.0 (middle row), and 3.5(bottom row). In each contour top half is PIV result and bottom half is LES result. The TKE is normalized by the jet velocity at the fully expanded condition.

In the baseline jet, the shear layer turbulence generation is sustained by the high-speed jet core and the high-intensity turbulences are a result of turbulence fluctuations across the large velocity gradient of the thin shear layer. In jets generated by MVG nozzles, the streamwise vortices generated by MVGs interact with the jet plume, causing deceleration and dampening of the shear layer turbulence due to enhanced mixing with the increased ambient fluid entrainment in the near nozzle exit region as was discussed in the transverse velocities of Figure 3.8. The more aggressive TKE reduction trend observed in jets generated by the double array MVG nozzle is due to the generation of much stronger streamwise vortices that enhance shear layer mixing and dissipation when compared to both the baseline and the single array MVG nozzles.

MGV effects on convective velocities of turbulent structures

Since convective velocities of turbulent structures are critical to the noise generation and radiation, it is important to assess the impact of MVG nozzles on this quantity. The convective velocities within the shear layer along the nozzle lip-line at Y/D = -0.5 are estimated from the instantaneous LES data as well as from the high-speed Schlieren visualization by computing the cross-correlations in the frequency domain of the time series signals. The signals are transformed into the frequency domain where the frequency-dependent cross-correlation is computed and ensemble averaged. Afterwards, the frequency-dependent cross-correlation is transformed back into to the time domain. It should be noted that the Schlieren signal sample size is small, but can still demonstrate trends in convective velocity variations.

Figure 3.14 shows the standard deviation of the light intensity signal from the Schlieren flow field at NPR=2.7 for the double MVG array nozzle as well as its estimated convective velocities along the lip-line at the reference point of X/D = 2.0, where the convective velocity is normalized by the ambient sound speed a_∞.

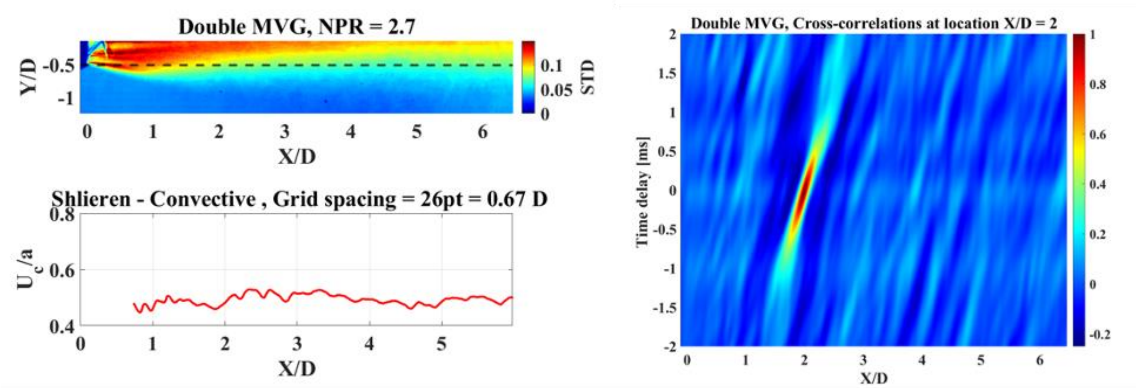

a)

b)

Figure 3.14: Schlieren fluctuating flow field (standard deviation) and the estimated convention velocities along the lip-line (data location indicated by black dashed line) for double array MVG nozzle. b) Cross-correlation contours of the reference location of X/D=2 with the entire lip-line at NPR=2.7 for Schlieren double array MVG nozzle.

The correlations between the reference point and other points along the lip line are first computed, and the slope of the correlation peak is extracted to estimate the convective velocity at each axial location. The extracted convective velocities are shown in Figure 3.15 based on both the axial velocity predicted by LES and Schlieren data at NPR=2.7. The LES results show convective velocities starting around $0.65a_\infty$ at X=1.5D and accelerating to $0.68a_\infty$ at X=2.1D, and drop to $0.65a_\infty$ by X=5D for the baseline nozzle. Both the single and double array MVG nozzles have greatly reduced the convective velocities near the nozzle exit, for example, the convective velocities are reduced from 0.65 a_∞ in the baseline jet to near $0.55a_\infty$ near x/D = 1.5, and the double array MVG nozzle shows a slightly more reduction in convective velocities beyond X=2D. The magnitude, however, gradually increases to a value similar to that of the baseline jet. The convective velocities estimated from the Schlieren data also show reductions by MVGs, however, there are some differences in details. Schlieren data estimated convective velocities show magnitudes dropping from $0.67a_\infty$ at X=1D to $0.55a_\infty$ at X=5D with a local acceleration region having velocity of $0.65a_\infty$ at X=3.25D, whereas the single MVG nozzle shows velocities from $0.55a_\infty$ at X=2.5D and approaching that of the baseline nozzle by X=5D, but shows convective velocities lower than $0.5a_\infty$ upstream of X=2.5D. In addition, the double array MVG nozzle shows convective velocities starting around $0.53a_\infty$ at X=2.5D and reaches lower values than both baseline and single array MVG nozzles at around 0.5 a_∞ at X/D=5. Even though the schlieren estimated convective velocities do not show the same magnitude levels seen by LES, the trend is consistent where both MVG nozzles reduce the near nozzle convective velocities. Also, towards the downstream direction, the double array MVG shows further convection velocity reduction than the other nozzles.

The underestimated convective velocities from the Schlieren images compared to the LES predictions are due to two factors. First, the Schlieren images spatial scaling was not calibrated but had an approximate scale value from pixel-to-pixel spacing mapped to the physical flow field space. Another factor is that the nature of Schlieren imaging being a line-of-sight integration causes contamination in the estimated convective velocity from different radial locations at different azimuthal angles around the jet axis that are tangent to the lip line through the line of sight.

An unexpected trend in the Schlieren convective velocity estimation is seen for the baseline nozzle showing a peak value between X/D = 3 and 4. Upon closer examination of the Schlieren image sequence, it was observed that this region shows jet core oscillations in the transverse direction away from the centerline increases in magnitude and as a consequence brings faster regions of jet inner flow to the geometric lip line of the nozzle. On the other hand, the LES predictions do not show this peak increase in convective velocity, the reason for this discrepancy is unknown and needs further investigation.

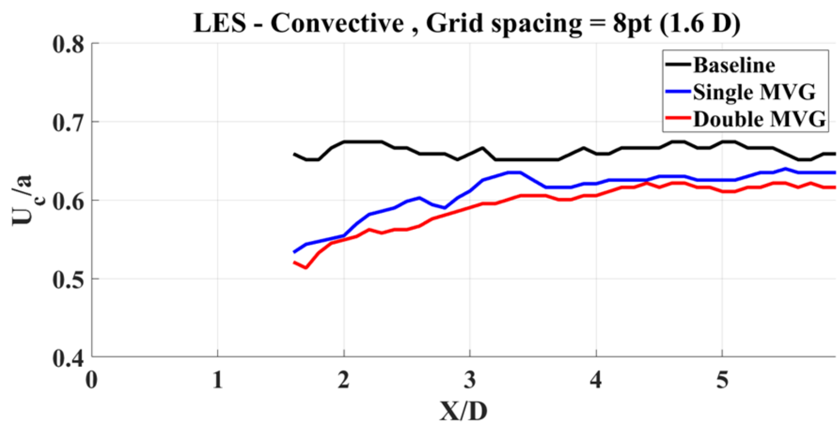

a)

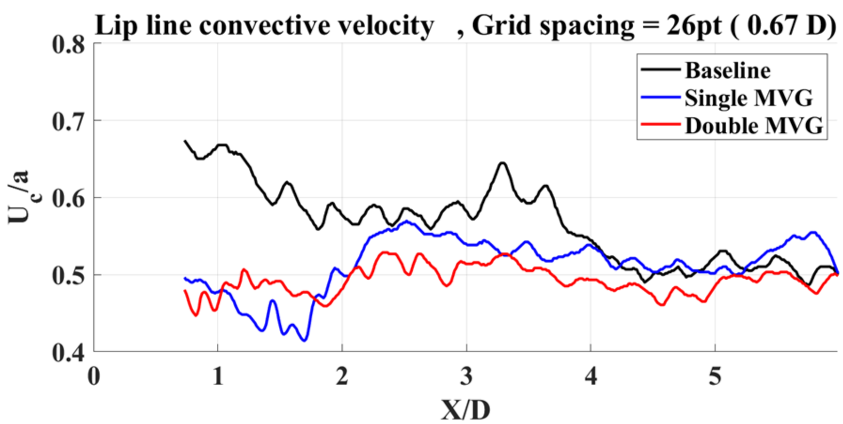

b)

Figure 3.15: Comparison of the estimated convection velocities along the lip-line for the various nozzle geometries at NPR=2.7 for (a) LES, and (b) schlieren data.

Convective velocities are normalized by ambient speed of sound [a = a_∞ = 340m/s].

The convective velocity reductions for the MVG nozzles should be the result of the reduced velocity gradients across the thicker shear layer due to the induced streamwise counter-rotating vortices that enhance shear layer mixing and reduces the TKE levels. The reduction in convective velocities should reduce the noise generation efficiency of large coherent structures and thus reduce the large turbulent mixing noise observed in the downstream direction of the acoustic far-field.

MGV effects on Near field acoustics

The microphone measurements of the acoustic near-field at NPR=2.7 and 3.0 are presented in Figure 3.16 and Figure 3.17, respectively. The baseline jet at NPR = 2.7 is a non-screeching jet, but it is a highly screeching jet at NPR = 3.0. In these figures, contours of the SPL distributions are plotted at the peak mixing noise frequencies corresponding to their respective nozzle configuration. These frequencies are based on the peak frequencies identified at the downstream observation angle of 150 degree from the far-field acoustic data of Figure 3.19. The acoustic magnitudes at the peak frequencies should reflect the source strength of mixing noise caused by the large coherent structures. For the screeching jet of NPR=3.0, the screech frequency is identified from the baseline jet at the upstream observation angle at 40 degrees.

It can be seen that high amplitudes associated with the mixing noise source sources are reduced with the implementation of MVGs. This is consistent with the reduction in TKE shown in Figure 3.13 and the reduction in the convective velocity shown in Figure 3.15. MVGs reduce both the noise source strength and the radiation efficiency.

At the screech frequencies shown in Figure 3.17, the baseline nozzle shows a distinctive two lobes pattern for the directivity of screech towards the upstream and downstream directions. A substantial reduction of the screech intensities is observed in both upstream and downstream lobes for the single-array MVG nozzle and a greater reduction is observed in the jet generated by the double-array MVG nozzle. These effects are due to the weakening of the shock cell structures in the jet plume for the single array MVG, as well as the subsonic jet core velocities induced by the double array MVG nozzle as discussed earlier, and will also impact the peak BBSN noise components and eliminate it.

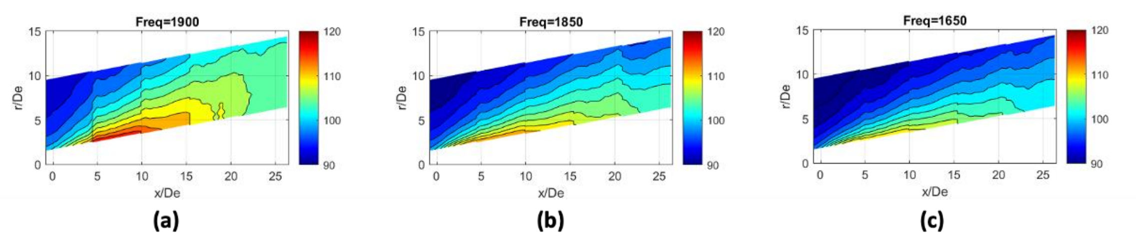

Figure 3.16: Distributions of the near-field microphone measurements at NPR=2.7 for (a) baseline, (b) single array MVG, and (c) double array MVG nozzle. The contours show SPL at the frequency of the peak turbulent mixing noise component. Frequency in [Hz].

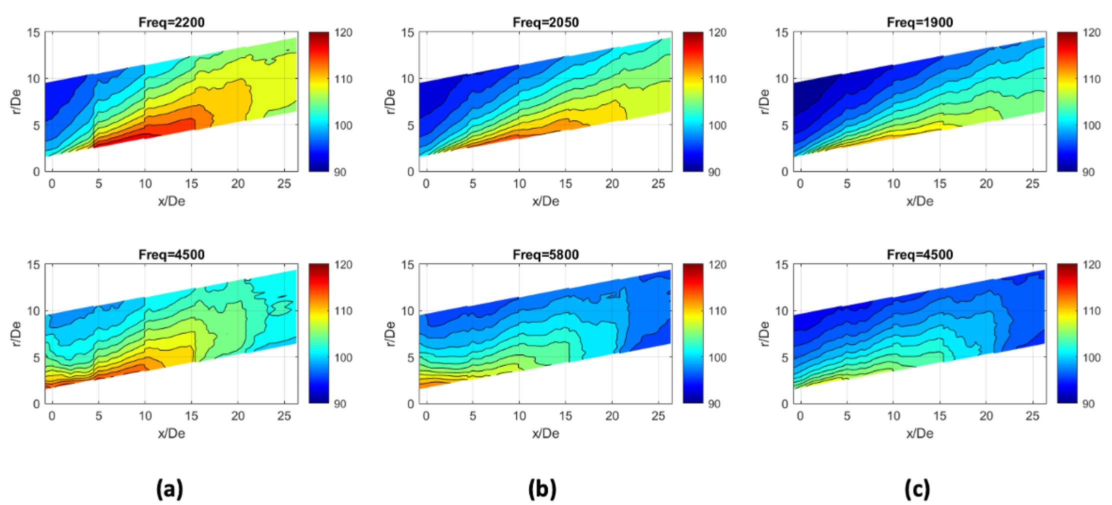

Figure 3.17: Distributions of the near-field microphone measurements at NPR=3.0 for (a) baseline, (b) single array MVG, and (c) double array MVG nozzle. The first row shows the contours of SPL at the frequency of the peak turbulent mixing noise component. The second row shows the contours of SPL at the frequency of the screech component. Frequency in [Hz].

Far field acoustics

In this section, the acoustic performances of the baseline and the MVG modified nozzles are compared and discussed. It should be mentioned that the data presented in this section were obtained by using the small nozzles of 1.45" at a far-field microphone distance of 100D. The far-field noise reductions $\Delta OASPL$ shown in Figure 3.18 are integrated over the full frequency range including the contributions from screech tones at the relevant conditions. The negative values indicate noise reduction relative to the baseline faceted nozzle. In Figure 3.19, the SPLs for both the baseline nozzle and the MVG modified nozzle are presented at jet conditions of NPR=2.7, 3.0, and 3.5 covering observation angles of 40°, 90°, and 150° for upstream, sideline, and downstream directions respectively. The nozzle total temperature is similar to the ambient temperature.

At the non-screeching condition of the baseline nozzle at NPR=2.7, both single and double-array MVG configurations show substantial noise reductions across all observation angles in Figure 3.18(a) as results of both the BBSAN reduction and also the mixing noise reduction. At this condition, the best performing nozzle configuration is the double array MVG nozzle with reductions up to 10dB at upstream angles, 6 dB at the peak noise angle 150°. The minimum noise reduction is 4dB near 120°.

In the upstream angles, both single and double array reductions have resulted from the reductions in BBSN amplitudes as shown at the upstream and sideline angles of the SPL plots in Figure 3.19(a). This is consistent with the weakening of shock cell structures shown in Figure 3.6 due to the large and strong large Mach disk generated by the oblique shocks internally generated by MVG blades. The reduction of the peak BBSAN is roughly 12dB for the single-array MVG nozzle and slightly more for the double-array MVG nozzle. In addition, the BBSAN peak frequency is also increased as a result of reduced shock cell spacing as shown in Figure 3.6 demonstrating the weakening of shock cell structures and lower jet core velocities.

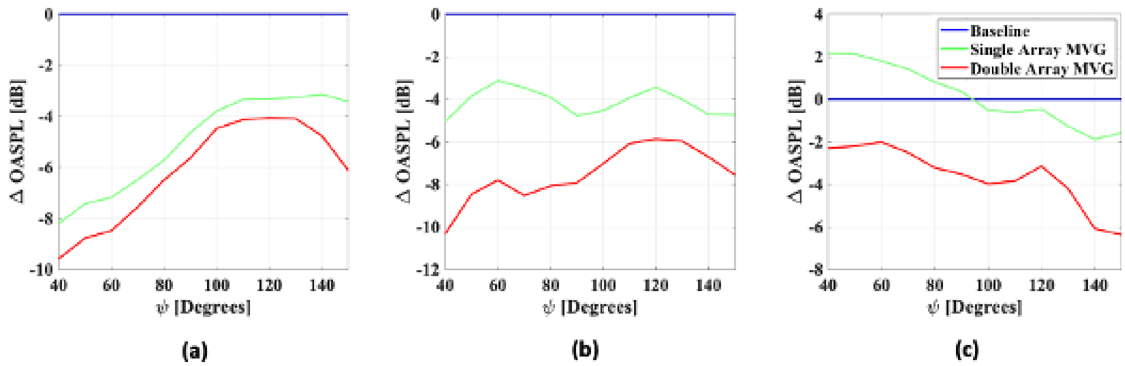

Figure 3.18: Comparison of the far-field overall sound pressure level reductions of the various nozzles at NPR= (a) 2.7, (b) 3.0, and (c) 3.5.

The MVG noise reductions at the downstream angles should come from several changes induced MVGs in the jet plume. First, the counter-rotating streamwise vortices generated by the MVG blades interact with the jet plume, resulting in an increased entrainment level between the ambient fluid and the shear layer. This accelerates the shear layer growth and reduces the spanwise vorticity levels for these nozzles (for example see Figure 3.11. In addition, the induced large and strong Mach disk reduces the jet core velocity, producing an inverted velocity profile that will also enhance the mixing in the jet plume. As a result, both the TKE intensities and the convective velocity of turbulence structures are reduced, and thus, the noise sources are weakened and the radiation efficiencies are reduced.

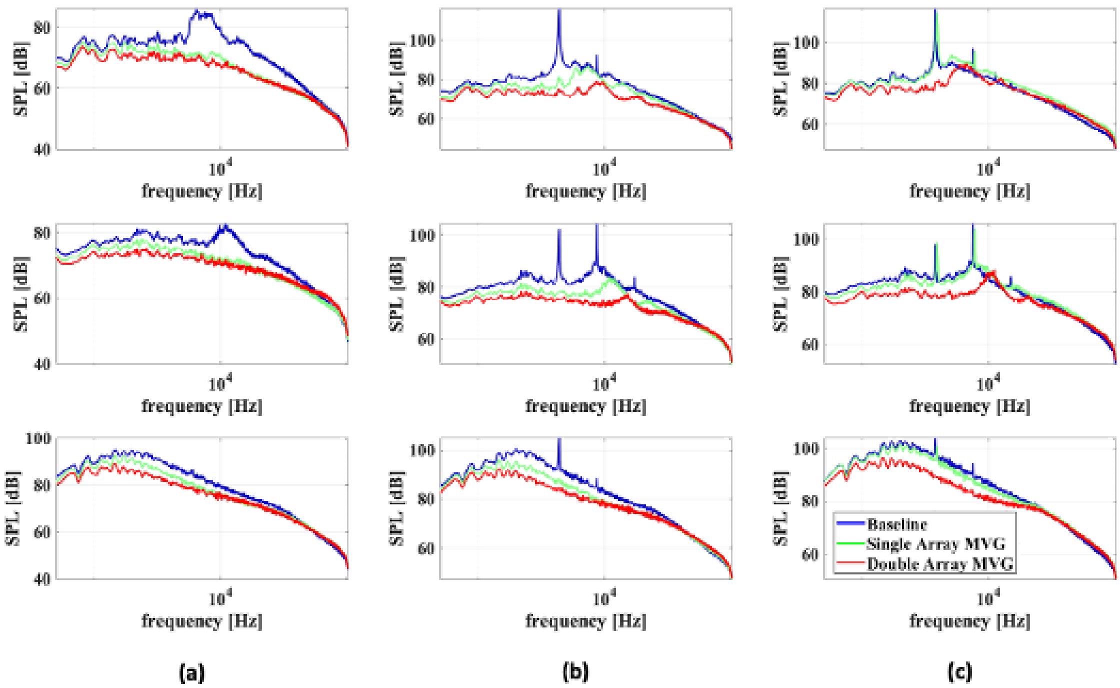

Figure 3.19: Comparison of the far-field sound pressure level of the various nozzles at NPR= (a) 2.7, (b) 3.0, and (c) 3.5. The observation angles are upstream at 40 degrees (first row), sideline at 90 degrees (second row), and downstream at 150 degrees (third row).

A similar amount of noise reduction is observed at NPR=3.0 for the double-array MVG nozzle, but the single-array MVG nozzle presents a reduction at the upstream observation angles. This is because at the condition of NPR=3.0, the shock cells are stronger but the Mach disk formed by the oblique shocks induced by the single-array MVGs is smaller and weaker, resulting in a smaller weakening effect on shock cells in the jet plume and less BBSN noise reductions as shown in the SPL spectra at the upstream and sideline angles in Figure 3.19(b). However, the double-array MVGs appear to still produce a strong Mach disk at this jet condition and the weakening effect on shock cells in the jet plume remains similar to that observed at NPR = 2.7. Both MVG modified nozzles present a shifted peak BBSN frequency to higher frequencies similar to that observed at NPR = 2.7. This is consistent with the reduced shock cell spacings observed in the MVG modified jets compared to the baseline jet as observed in the centerline velocity profiles discussed earlier.

At NPR=3.5, Figure 3.18(c) shows that the double array MVG configuration is capable of noise reductions across all observation angles, but the single array MVG shows a noise increase in the upstream angles. The increase in the upstream noise caused by the single array MVG can be also seen in the SPL distributions in the upstream and sideline directions in Figure 3.19(c). As was discussed earlier on the axial velocity profiles shown in Figure 3.6, the single-array MVGs increase the shock-cell strength rather decrease at this higher nozzle pressure. This is consistent with the increase of the BBSN noise component. On the other hand, the double-array MVGs still present a weakening effect on the shock cells in the jet plume at this nozzle pressure but at a lesser magnitude. This results in less noise reduction in the upstream direction compared with that observed at NPR = 2.7 and 3.0. A substantial noise reduction is again observed at the downstream angles by the double-array MVGs, but the downstream noise reduction by the single-array MVGs is less than those observed at lower NPRs. This single-array MVG nozzle placed at 0.65D upstream of the nozzle exit appears to be not as effective at higher NPRs, but the double-array MVG nozzle remains effective over all the nozzle pressure ratios studied in this paper.

Far-field Nozzle scale effects and comparison of Experiment and Numerical acoustics

The far-field acoustics of the baseline and single MVG nozzle configurations are presented in this section and are compared to LES predictions shown in Figure 3.20 to

Figure 3.22. It should be mentioned that the LES simulations are conducted with a nozzle diameter of 3.2 inches with a far-field distance of 50 D. The microphone measurements are done on a large nozzle size of 3.2 inches and a small nozzle of 1.45 inches, with far-field microphone distances of 50D and ~100D respectively. The use of two nozzle sizes illustrates the scaling effects of nozzles implemented with MVGs and shows if noise reduction trends can be achieved at different nozzle scales. It should be noted that due to the geometric differences in the external nozzle lip inclination angles between the large nozzles at 7.5° and the small nozzles at 45° shown in Figure 2.11, the acoustics scaling would be affected due to surface reflections and microphone line-of-sight limitations. Scaling of the small nozzles has been carried out following the method outlined by Viswanathan[104] with atmospheric attenuation corrections following Bass et. al.[95,96]).

Comparisons of scaling effects of the two nozzle sizes of the experiments are presented in Figure 3.20 and Figure 3.21. The formal shows the overall sound pressure levels (OASPL), and the latter is the noise reduction ΔOASPL. LES predictions are also presented in these figures. It should be noted that the screech tone has been removed in the noise computations. For the baseline and single array MVGs, it can be seen that there is a very good agreement between LES predictions and the laboratory measurements produced by the large nozzle.

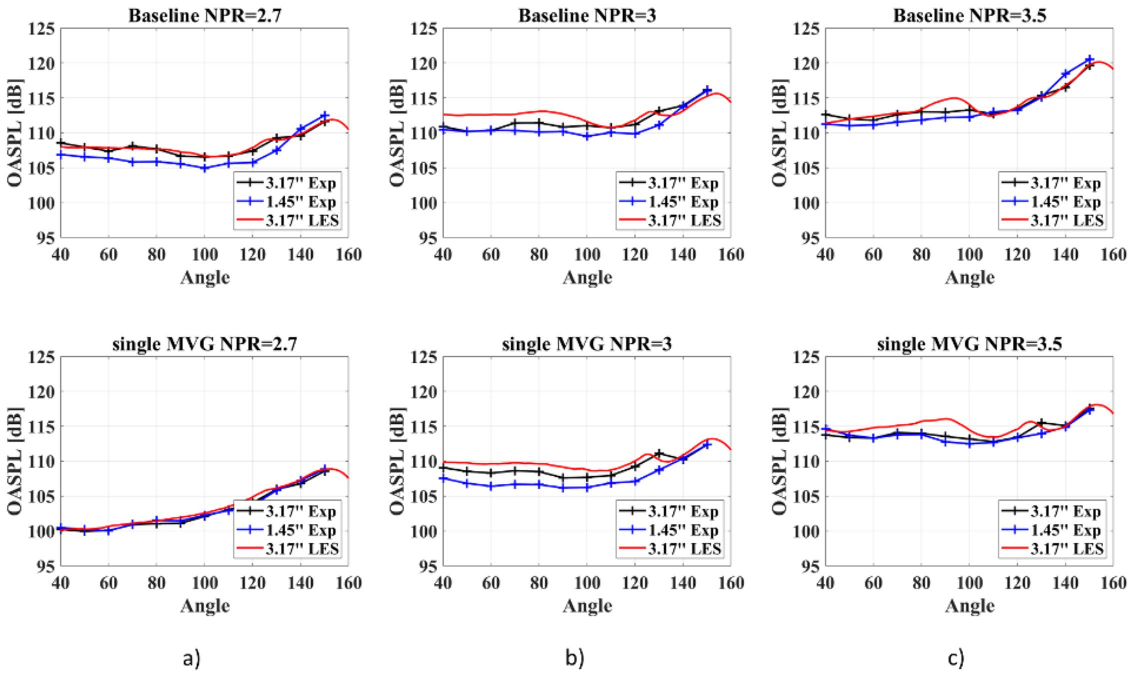

Figure 3.20: Far-field noise reduction at NPR= a) 2.7, b) 3.0, and c) 3.5. For baseline and single array MVG with different nozzle diameters. Small nozzles are scaled up to match large nozzles.

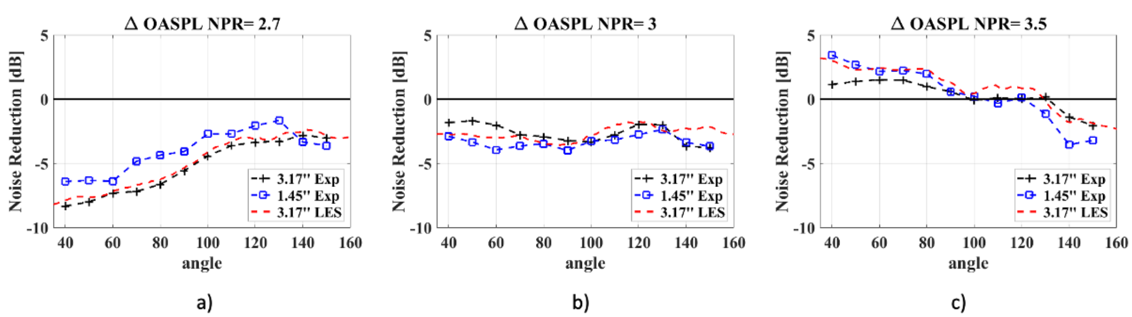

Figure 3.21: Far-field noise reduction at NPR= a) 2.7, b) 3.0, and c) 3.5. For baseline and single array MVG with different nozzle diameters. Small nozzles are scaled up to match large nozzles.

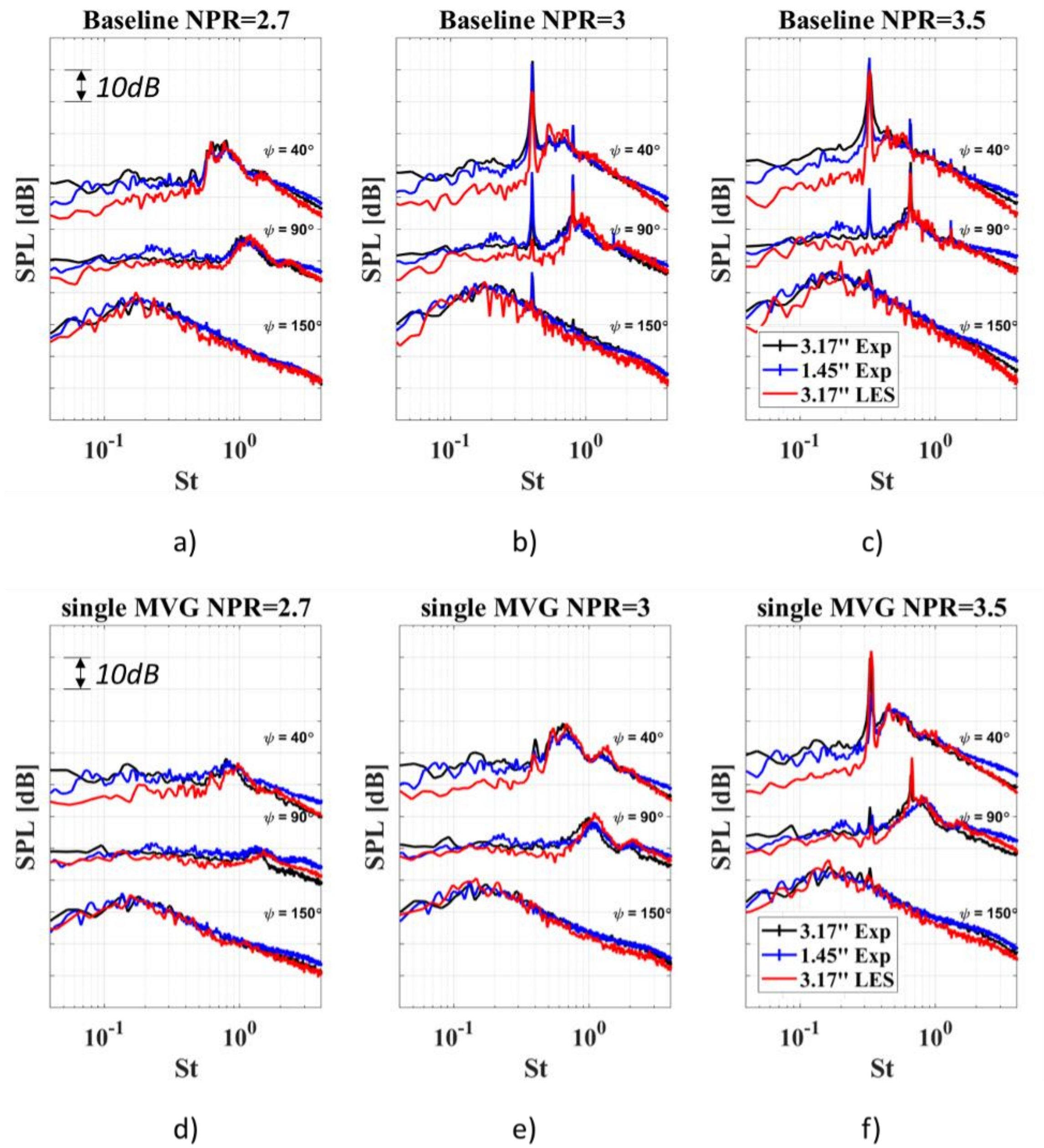

Figure 3.22: Far-field noise spectral pressure levels of baseline (top row a, b, and c) and single array MVG nozzles (bottom row d, e, and f) at nozzle pressure ratios NPR=2.7 (a,d) , 3.0 (b,e), and 3.5 (c,f). Noise scaling of experiment with diameter of 1.45” to match diameter 3.17” of experiment and LES data.

However, even though the results of the small nozzle follow the same trend, there are some differences in amplitudes especially at the upstream angles, where the small nozzles produce lower upstream noise intensities and the difference can be up to 2dB. As shown in the baseline SPL plots at upstream angles in Figure 3.22, the small nozzles produce weaker BBSN when scaled and compared to its larger nozzle counterpart. Also, the scaled high-frequency noise of the small nozzles is higher than that of the larger nozzles and this high-frequency noise increase is more visible in the upstream direction. A possible explanation for the latter could be due to a lack of a smooth transition from the jet rig plenum to the pipe upstream of the small nozzles. This sudden change of plenum diameter of the facility to the upstream section of the nozzle is expected to increase turbulence levels. On the other hand, the larger nozzle has a fifth-order polynomial plenum contraction that causes a smooth flow transition from the plenum to the connecting pipe upstream of the large nozzle and is expected to deliver a lower level of turbulence in the flow. It is possible that the higher upstream turbulences increase the fluctuation levels of downstream shock cells and reduce the shock-cell strength and thus produce weaker BBSN noise levels. This weaker BBSN level combined with the external nozzle geometry inclinations should be responsible for the noise difference in the upstream direction.

The agreement in scaling effects shown in these comparisons demonstrates that the MVG noise reduction mechanisms are applicable at the various nozzle sizes tested and are capable of delivering similar noise reduction levels and trends.

Chapter 4: Hydrodynamic and Acoustic Waves from Vortex Generators Noise Reduction for Supersonic Jets

Time-resolved Schlieren visualizations are analyzed using spectral analysis methods to simultaneously study the spatiotemporal spectral contents of both the waves generated in the flow field of the supersonic jet and its acoustic wave emissions. The physical mechanisms of supersonic jet noise generation as well as its reduction mechanisms using MVGs as a jet noise reduction technology is investigated. In addition, a new generation mechanism for BBSAN noise component and its directivity is proposed. The jets are analyzed in the frequency-wavenumber domain, it is found that MVGs cause a shift in wavenumber spectra to larger values. This shift reduces the noise generation efficiencies of the jet's instability waves and the turbulent structures in addition, it weakens their interaction with the shock cells leading to noise reductions. The directivity of BBSAN is influenced by interference patterns from the phased array of noise sources emitted from the interactions of turbulence with the shock cells. Finally, the BBSAN noise generation mechanism is a result of reflected shock waves produced from shock-vortex interaction that propagate as sound waves along the shear layer and influence it to generate internal trapped waves and modulate the phase coherence of the turbulent structures convecting along the shear layer to be phase locked with the shock cell tip interaction frequencies. Based on these findings new generation mechanisms for the noise and directivity are proposed in this study.

MVG FLOW FIELD MODIFICATIONS:

Figure 4.1 shows instantaneous axial Mach number contours in the streamwise-transverse plane (first row), as well as the time averaged axial velocity contours normalized by the jet exit velocity in the spanwise-transverse cross-sections at axial locations of X/D=0 (second row) and X/D=1 (third row) for a) baseline faceted nozzle and b) single array nozzle, for the jet operating condition of NPR=2.7. It is found that the MVG nozzle generates internal oblique shock waves that causes the Mach disk outside the nozzle to become stronger and weakens the shock waves in the subsequent shock cells in the jet plume causing a reduction in the jet axial velocity. The weaker shock cells will reduce the interaction strength between the shock cell tips and the convecting turbulent structures leading to reductions in the BBSAN noise components. In addition, the MVGs generate streamwise counter rotating vortices that are formed on the nozzle walls and travels along the shear layer as the flow exits the nozzle. These counter-rotating vortices induce radially inward and outward flow resulting in a corrugated shape for the jet cross-section as the flow travels away from the nozzle exit. This effect enhances shear layer mixing and enhances entrainment leading to a reduction in convective velocity of the turbulent coherent structures in the shear layer, also, this mixing interrupts the formation of large coherent structures and breaks down the larger turbulent structures and reduces their scales into smaller ones. This effect causes a reduction in the mixing noise generation efficiency and reduces its noise component. Hence, MVGs impact the supersonic jet by generating internal oblique shock waves that interact with the jet plume as well as generating streamwise counter-rotating vortices that enhance shear layer mixing and entrainment. Subsequently, the influence of the MVGs on the supersonic jet plume is examined in the statistical quantities derived from the Schlieren visualization data in terms of shock cell spacing in the time averaged flow field and the intensity of shock cell oscillations and shear layer spread in the standard deviation of the flow field. Figure 4.2 presents the time averaged flow of the jet plume for the various nozzle configurations at all NPRs of this study, which shows that the shock cell spacing (Shock cell locations indicated by the red dashed lines) is increased with the increasing NPR values. In addition, the MVGs cause the reduction in shock cell spacing for the single array MVG and further shock cell spacing reduction for the double array MVG configuration, this trend is seen for all NPRs in this study. It should be mentioned that for the double array MVG nozzle at NPR=2.7 the jet plume was found to be subsonic based on PIV measurements of an earlier study[105], since subsonic flow cannot sustain shock cells, the observed cells could be due to standing pressure waves inside the jet.

The fluctuating flow field for the nozzle configurations and the NPRs of this study is presented in Figure 4.3 where the contours show the standard deviation of the flow field. For the baseline nozzle at NPR=2.7, high intensity fluctuations can be seen along the inner shear layer as well as the shock cell tips up to the second shock cell, beyond that the entire shock cell undergoes intensity fluctuations. For this condition, the high intensity fluctuation along the inner shear layer is attributed to the jet's preferential instability mode of the coherent structures having a symmetric oscillation characteristic as will be shown in Figure 4.6(a). On the other hand, the anti-symmetric oscillations for the screeching jets of the baseline nozzle at NPR=3.0 and 3.5, the inner shear layer exhibit a spatially varying intensity fluctuation level as the flow passes subsequent shock cells in the downstream direction. The effect of entrainment from the MVG nozzle configurations can be seen as thickening of the shear layer and more prominently in the inner shear layer moving radially inward dissipating the jet core resulting in reduction of its diameter. In addition, the inner shear layer fluctuation intensity is reduced indicating a weaker interaction between the convecting shear layer structures and the shock cells. The exception is for the single array

MVG nozzle at NPR=3.0 showing an increase in fluctuation compared to the baseline case at the same NPR. This is due to the increased interaction between the lower portion of the stream-wise counter-rotating vortices interacting with the relatively strong shock cells. However, due to the breakdown of the large coherent structures its interaction with the shock cells can no longer sustain screech as will be discussed in Figure 4.19 (a). Therefore, MVGs can cause the weakening of the shock cells and reduce their spacing. Also, the increase in shear layer entrainment and mixing causes reductions in the shear layer's large turbulent fluctuations leading to weaker interactions with the shock cells.

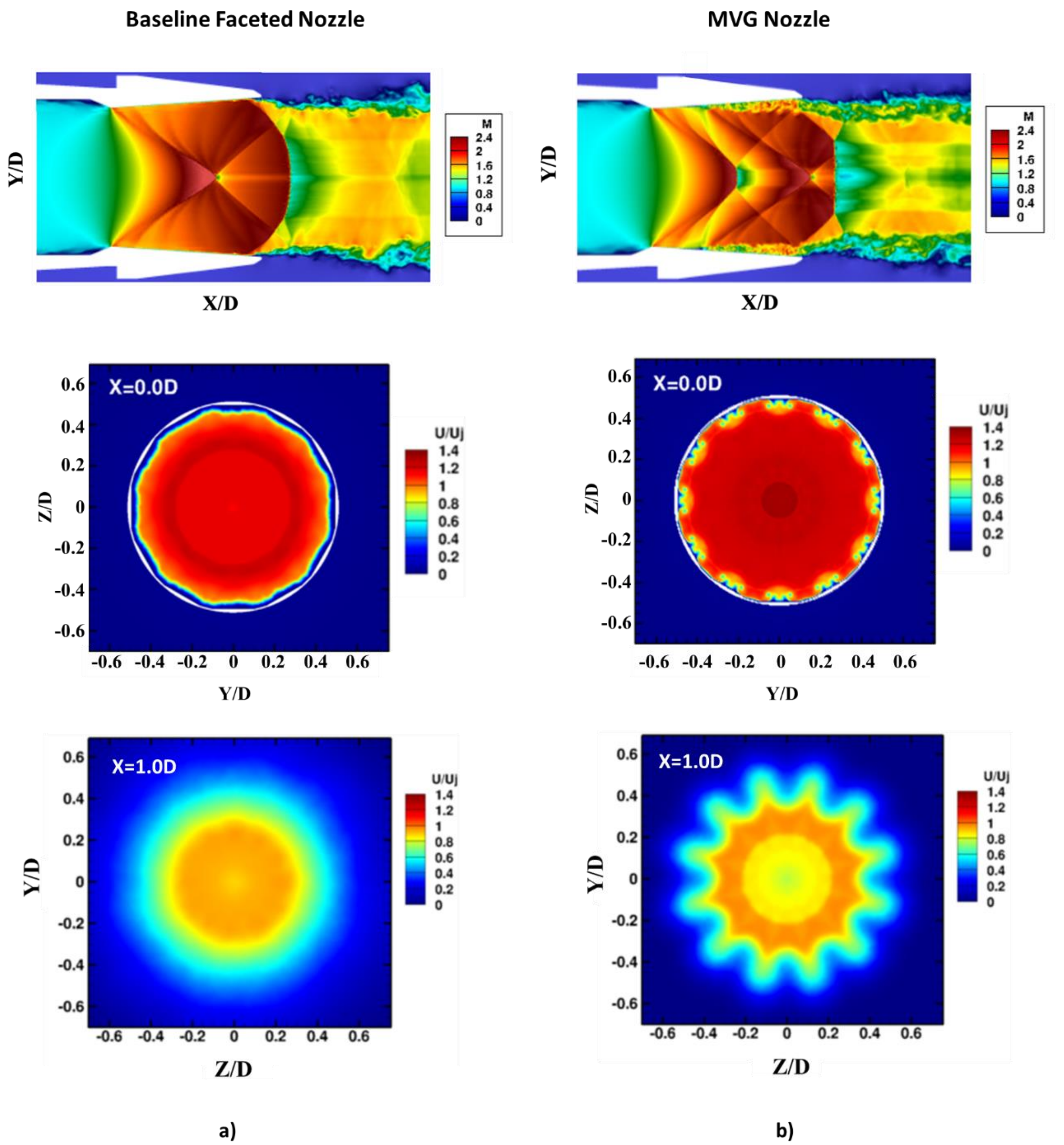

Figure 4.1: LES axial Mach number contours in the X–Y plane (top row), axial velocity contours in Y–Z cross section at the nozzle exit plane (second row), and at downstream location of X/D=1 (third row). The operating condition is NPR= 2.7 for: (a) baseline faceted (left column) and (b) single-array MVGs (right column). The contours are used to demonstrate the impact of MVGs on the nozzle lip separation size, the generation of oblique shocks, and the generation of streamwise counter-rotating vortices. LES contours from Liu et al.11[9]

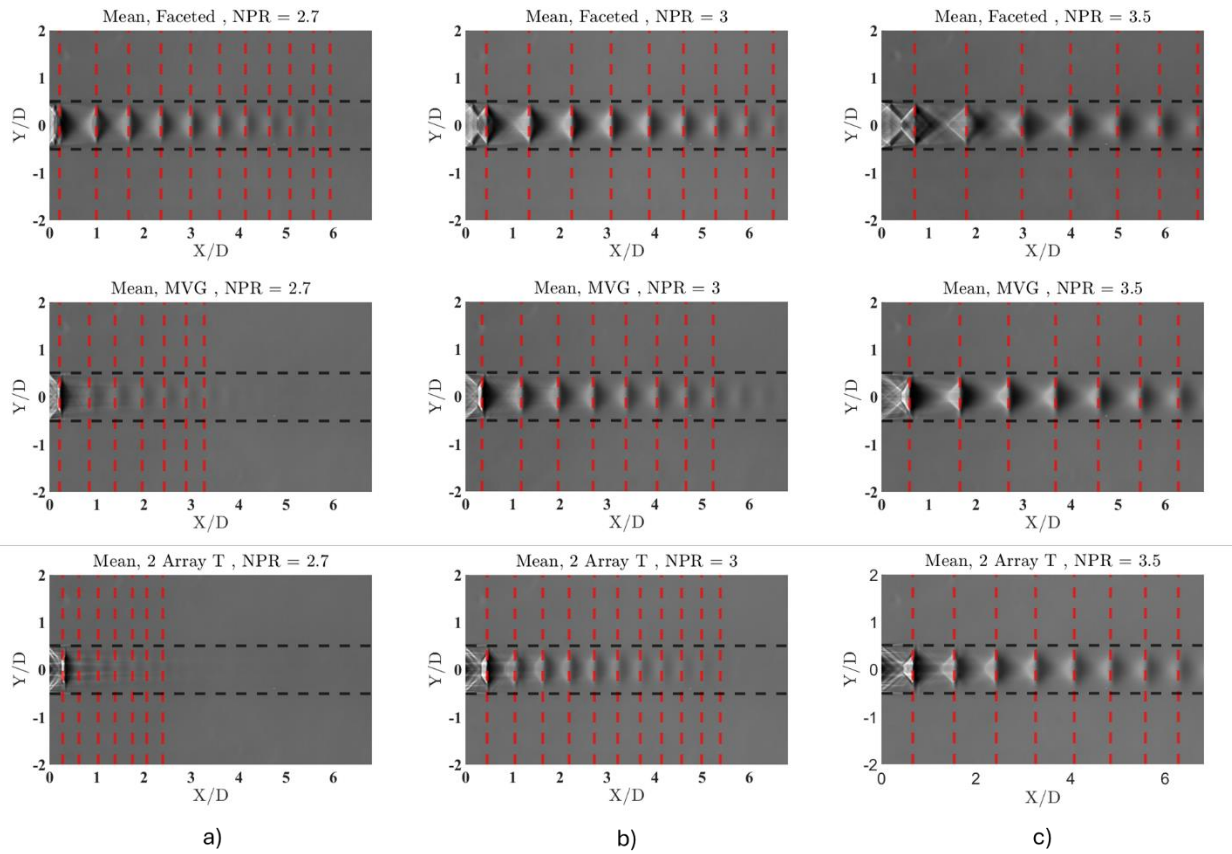

Figure 4.2: Schlieren visualization showing the average flow field for a) baseline faceted, b) single array MVG, and c) double array MVG nozzles. The operating conditions are for NPR=2.7(left column), 3.0 (middle column), and 3.5 (right column). Horizontal dashed lines indicate the nozzle lip lines and the vertical dashed red lines indicate locations of shock cell tip intersection with the shear layer.

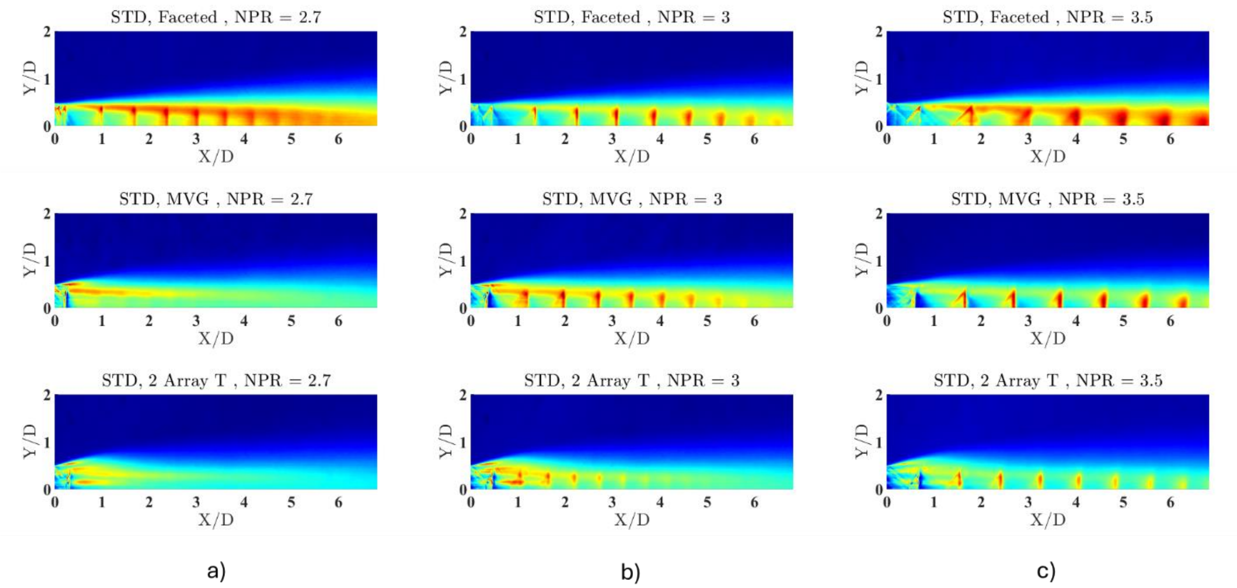

Figure 4.3: Standard deviation of Schlieren visualization showing the fluctuating flow field for a) baseline faceted, b) single array MVG, and c) double array MVG nozzles. The operating conditions are for NPR=2.7(left column), 3.0 (middle column), and 3.5 (right column).

FREQUENCY-WAVENUMBER SPECTRA

Apart from the conducted statistical analysis of the schlieren visualization, a spectral analysis can be performed on the time resolved data to shed light on the wave instability dynamics of the fluctuating flow field and its acoustic generation mechanisms. By transforming the Schlieren data from the temporal-spatial domain to the frequency-wavenumber (f-k) domain its spectral content can be studied. The f-k plots in Figure 4.4 show the frequency-wavenumber spectral intensity distributions for the baseline nozzle at various operating conditions of NPR values. The extracted data is along lines parallel to the jet axis and are from radial locations of Y/D= 0 (centerline), 0.5 (lip line), and 1(outside the jet) and are shown in Figure 4.4 (a), (b), and (c), respectively. In these f-k plots the axes show the temporal frequency in Strouhal number, and the axial wavenumber normalized by the nozzle diameter. The positive wavenumber values (right half of the plots) indicated downstream propagating waves and the negative wavenumber values (left half of the plots) indicate upstream propagating waves. For reference the ambient acoustic speed of sound propagation is overlaid on these plots where the dotted magenta lines with slopes indicating speed of sound wave propagation in the upstream and downstream direction. The wave propagation velocity as a function of frequency and wavenumber is given by:

$$U = \frac{2\pi f}{\left(\frac{k_x}{D_e}\right)}$$

Where f is the temporal frequency, k_x is the axial wavenumber, and D_e is the nozzle exit diameter. This equation shows that the propagation velocity of the waves or structures are proportional to their slopes in the f-k plots.

For the baseline faceted nozzle some of the flow features can be pointed out in the f-k plots in Figure 4.4, the high intensity of the distributions indicated by the dashed black oval is the wave spectral distributions of the turbulent structures convecting along the shear layer at Y/D=0.5 with slower convection velocities compared to the ambient speed of sound which is indicated by the dotted magenta line. Inside the jet at Y/D=0. The dashed red oval indicates upstream traveling internal waves, and the solid arrow indicates the peak wavenumber value of the average shock cell spacing. The dashed black arrows indicate the waves associated with the screech that are propagating in both upstream and downstream directions. Outside the jet at Y/D=1, the red oval indicates downstream acoustic waves assorted with the turbulent mixing noise, whereas the yellow oval indicates the upstream acoustic waves associated with BBSAN noise components propagating at the ambient speed of sound.

The following trends can be observed for the baseline jet: in Figure 4.4(a) along the jet axis Y/D=0, as the NPR increase the wavenumber of the shock cell spacing reduces to lower values from $kD \approx -12$ to $kD \approx -8$ for NPR=2.7 to NPR=3.5 respectively, this is consistent with the increase in shock cell spacing with increasing NPR and the wavenumber is inversely proportional to the wavelength (twice the shock cell spacing) which is given by the following equation:

$$k = \frac{2\pi}{\lambda}$$

Where: k is the wavenumber, λ is the wavelength; at the nozzle lip line Y/D=0.5 Figure 4.4 (b), the spectral distribution of the downstream convecting turbulent structures increases its slope with increasing NPR indicating an increase in convection velocity. In addition, the high-intensity distribution width becomes narrower as the NPR is increased indicating that the turbulence covers smaller wavenumber spread range and hence a smaller turbulence length scale range. This is due to the increased Reynolds number of the higher NPR having a thinner shear layer where the larger turbulent structures have not yet fully developed and grown within the shear layer length within the Schlieren field of view. At NPR= 3.0 and 3.5 the jet undergoes screech and a strong screech wave at the ambient speed of sound can be seen propagating in both upstream and downstream directions along the shear layer; Outside the jet at Y/D=1 in Figure 4.4 (c), the region of the high-intensity of the acoustic mixing noise propagating in the downstream direction is reduced in size for the same reason discussed earlier due to the increase in Reynolds number and the limited field of view to capture the shear layer growth rate to form the large coherent structures.

To study the impact of MVGs on the frequency wavenumber spectral distribution the f-k plots of the various nozzle configurations are presented in Figure 4.5 and are shown for NPR=3.0 as it is representative of the other operating conditions. At the jet centerline Y/D=0 in Figure 4.5 (a) it can be seen that the MVGs cause the lobe representing the shock cell wavenumber to shift to larger values where kD~-10 for the baseline, kD~-12 for the single array MVG, and kD~-14 for the double array configuration, this is due to reductions in the shock cell spacing. In addition, MVGs cause reductions in the intensities of the internal upstream propagating waves, indicating a weakening effect on these waves and is attributed to the weakening of the shock cell strengths and the reductions in the jet core velocities. Along the lip line at Y/D=0.5 Figure 4.5 (b) the slope of the downstream convecting turbulent structures distributions is reduced indicating that the mixing and entrainment from MVGs cause the shear layer to have lower convective velocities compared to the baseline, this effect is more for the double MVG configuration showing slower convection velocities than both the baseline and the single array MVG. In the upstream direction, the screech waves are diminished for the single array MVG and completely suppressed for the double array MVG configuration. Outside the jet at Y/D=1 Figure 4.5(c) the distribution intensities of the upstream acoustic waves of the BBSAN are reduced for the single array MVG configuration, and further reductions are seen for the double array configuration. Similar reductions are seen for the waves of the downstream mixing noise component with the highest reductions occurring for the double array MVG configuration due to the enhanced mixing and breakdown of the large coherent structures resulting in weaker mixing noise wave emissions.

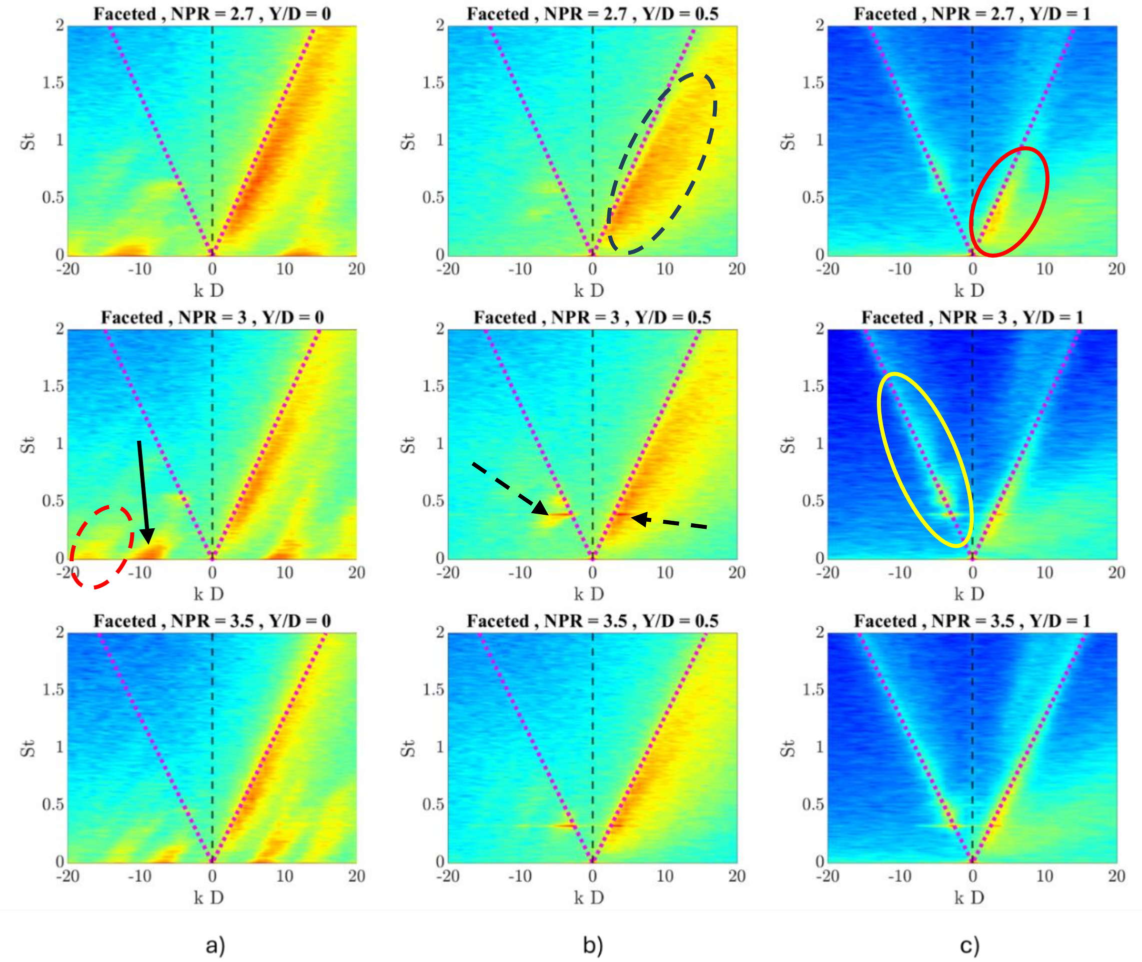

Figure 4.4: Frequency-wavenumber (f-k) intensity distributions from the time-resolved schlieren images of the baseline faceted nozzle for operating conditions NPR= 2.7 (first row), 3.0 (second row), and 3.5 (third row). The distributions are shown at various radial locations parallel to the jet axis, a) at the jet centerline Y/D=0, b) on the lip line Y/D=0.5, and c) outside the jet plume at Y/D=1.0. The dotted magenta lines indicate the slope of the ambient acoustic speed of sound propagation velocities in the downstream direction(right half of the plots with positive wavenumbers) and upstream direction(left half of the plots with negative wavenumbers). Dashed black oval indicates shear layer conveting turbulent structures. Dashed red oval indicates internal upstream propagating waves. Solid black arrow indicates main lobe of the shock cell spacing wavenumber. Dashed black arrow indicates screech instability waves propagating upstream and downstream.

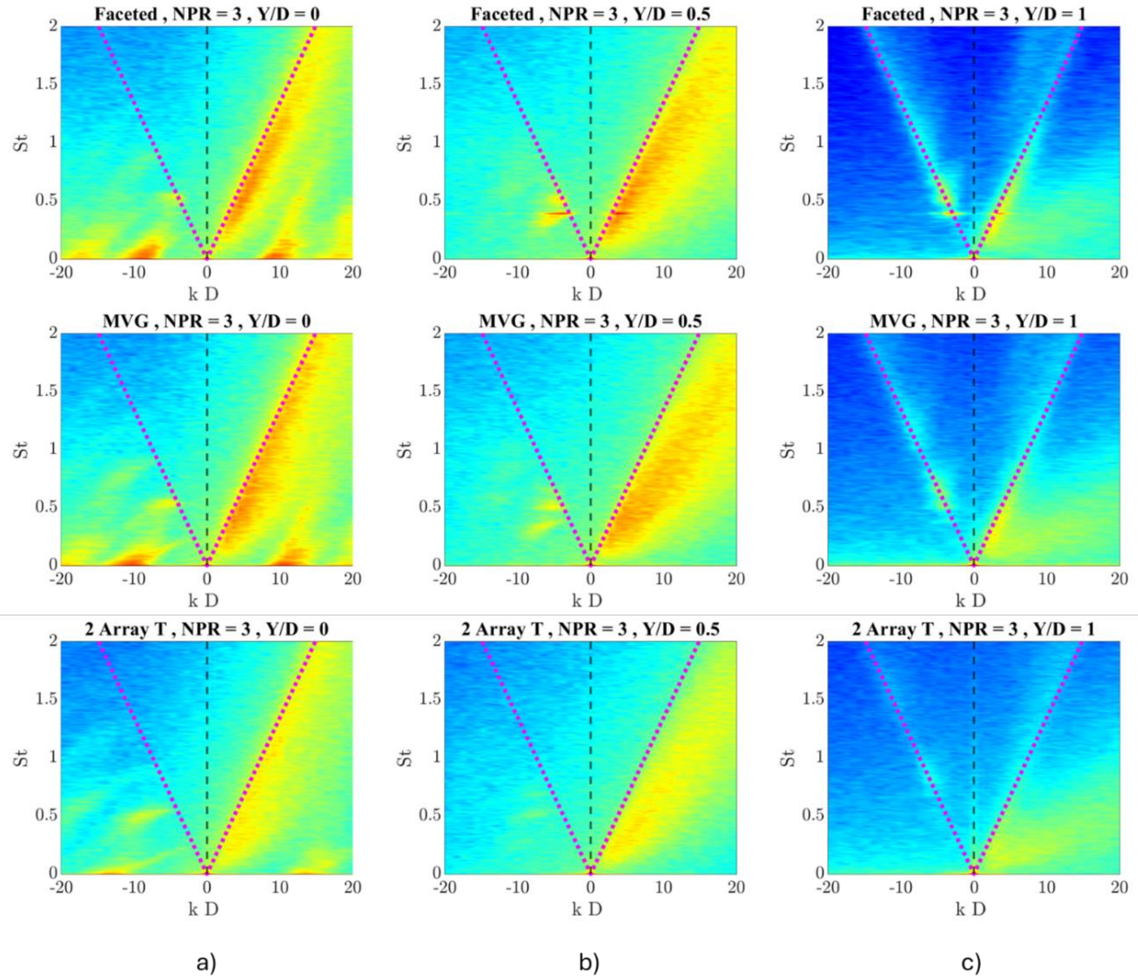

Figure 4.5: Frequency-wavenumber (f-k) intensity distributions from the time-resolved schlieren images of the various nozzle configurations for baseline faceted nozzle (first row), single array MVG (second row), and double array MVG configuration (third row). The Nozzle operating condition is NPR=3.0. The distributions are shown at various radial locations parallel to the jet axis, a) at the jet centerline Y/D=0, b) on the lip line Y/D=0.5, and c) outside the jet plume at Y/D=1.0. The dotted magenta lines indicate the slope of ambient acoustic speed of sound propagation velocities in the downstream direction(right half of the plots with positive wavenumbers) and upstream direction(left half of the plots with negative wavenumbers).

WAVENUMBER DISTRIBUTION AND ACOUSTIC WAVE RECONSTRUCTION

The above spectral analysis demonstrates the complexity and wealth of information that can be obtained from the flow field structures and the generated waves. To analyze the specific flow components that are dominant at specific temporal frequencies a Fourier filtering is applied, where the downstream wave components are separated from the upstream components using reconstruction of either positive or negative wavenumber spectra at a given frequency this is carried out mathematically by:

$$I(x,y,t) = \sum_{k}\sum_{\omega} \hat{I}_{k,\omega}\, e^{ikx} e^{-i\omega t}$$

And satisfying wavenumber values

$$k < 0, upstream\ propagation$$

$$k > 0, downstream\ propagation$$

Where ω is selected for a given frequency of interest. The reconstruction results of the Fourier filtered flow field are shown in Figure 4.6 for the baseline faceted nozzle at the highly screeching condition of NPR=3.5. The frequencies of interest are selected based on the far field acoustic spectra representing the peak large-scale mixing noise, the screech, and intense BBSAN noise components with frequencies St=0.17 (Figure 4.6 (a)), St=0.33 (Figure 4.6 (b)), and St=0.69 (Figure 4.6 (c)), respectively. In these contours, red dashed lines are overlaid as a visual aid to indicate the shock cell locations.

Examining the filtered Fourier flow field for the baseline nozzle at the peak frequency of the large-scale mixing noise component in Figure 4.6(a) it can be seen that the large-scale coherent structures undergoes a rapid growth rate as the wave instability travels downstream along the shear layer, additionally its associated acoustic wave emission increases in intensity towards the downstream direction. The accelerated growth rate of the convecting structures can be ascribed to the shear layer forcing of the K-H instability through the "collective interaction" mechanism proposed by Ho & Nosseir[35]. At this low frequency the wavelength of the convective structures is larger than the shock cell spacing, this makes their interaction with the shock cells unable to produce upstream propagating acoustic waves as seen in the contour of the upstream component. For the screech frequency Figure 4.6(b) shows the jet is undergoing intense flow resonance, where the shear layer K-H instability is modulated at the screech frequency leading to its growth along the shear layer exhibiting an anti-symmetric oscillation about the jet centerline. In addition, the wavelength of the coherent structures instability is comparable to the shock cell spacing causing intense acoustic wave emissions in both upstream and downstream directions, the superposition of these waves, the downstream hydrodynamic and acoustic waves and the upstream acoustic waves, give rise to the standing wave pattern observed by Panda [43,44]. In addition, the standing wave pattern helps modulate the growth of the shear layer instability as the convecting structures pass through successive high- and low-pressure regions. Furthermore, the intense upstream propagating acoustic waves interact with the shear layer influencing the upstream propagating waves inside the jet, which is the generation mechanism of the internal trapped waves and the Guided Jet Mode (G-JM) at the screech frequency. Similar to the features described above for the screech frequency, the same mechanisms can be seen at the higher frequency component of BBSAN in Figure 4.6(c). The downstream components of BBSAN show formation of organized coherent turbulent structures traveling along the shear layer accompanied by organized acoustic wave emissions, since the wavelength of these structures are small compared to the shock cell spacing, their interaction with the shock cell tips produce acoustic emissions that propagate into the upstream direction giving rise to BBSAN noise components in the far-field acoustic measurements. The BBSAN acoustic waves emitted by the jet are weaker than the screech acoustic wave emissions, but they are still intense to generate high acoustic noise levels. Also, the upstream and downstream waves interact to form standing wave patterns that aid in modulating the shear layer instability at this frequency which leads to the downstream convecting structures to be spatially coherent to interact with successive shock cell tips contributing to the overall phase coherence of the BBSAN emissions.

To study the wavenumber characteristics of the previously discussed flow features, the radial distributions of the axial wavenumber spectra are extracted for the same frequencies of large-scale mixing, screech, and BBSAN and are presented in Figure 4.7(a-c), respectively. In these contour plots, the left half of the plots indicate negative wavenumbers with waves propagating in the upstream direction, while the right half of the plots indicate positive wavenumber with waves propagating in the downstream direction. The nozzle lip lines are indicated by the dashed black lines, and the wavenumber associated with the ambient speed of sound is indicated by the dotted black lines for directions.

In Figure 4.7(a), it is found that inside the jet core there are multiple high intensity lobes for waves propagating inside the jet in the upstream direction with negligible external wave propagation, this internal waves are a result of the intense interaction between the large coherent turbulent structures with the collapsing end of the potential core causing the shock cells in the region $3<x/D<6.5$ to have axial oscillatory motion with varying propagation velocities, this can be clearly seen in the smearing of the shock cell shapes towards the end of the jet in Figure 4.6(a - upstream components). Additionally, the shock cell oscillations of the collapsing jet core will have a downstream perturbation component and is observed as high intensity positive wavenumber lobes in Figure 4.7(a). Outside the jet in the downstream direction, the low frequency wavenumber distribution shows intense acoustic emissions around the ambient speed of sound wavenumber with intensities dropping rapidly for larger wavenumber values which is representative of the various length scales turbulence and their associated hydrodynamic pressure waves at various wavelengths. Where, as the turbulent structures are reduced in size their hydrodynamic pressure wave emissions are rapidly weakened and are spatially confined to radial regions close to the shear layer. In Figure 4.7(b) the wavenumber distribution for the screeching jet is presented, it is found that the high-intensity lobes inside the jet have bifurcated into two lobes near the inner shear layer in the upstream direction and closer to the jet centerline in the downstream direction, additionally, the wavenumbers of the peak lobes have shifted to smaller wavenumber values. The bifurcation near the shear layer effect is due to the anti-symmetric upstream and downstream propagating waves having a strong region of influence near the inner shear layer in the upstream direction, whereas its propagating influence reaches closer to the centerline in the downstream direction which can be seen in Figure 4.6 (b). Since the main high intensity lobes have wavenumbers at the ambient speed of sound and at their vicinity, they are capable of efficiently emitting intense acoustic wave radiation at the acoustic wavenumbers. For the BBSAN frequency component, the wavenumber distribution shows reductions in the intensity levels for the internal upstream wave propagation but is still capable of producing acoustic wave emission at the acoustic wavenumber, on the other hand, the intensity of the downstream internal wave shows a gradual intensity decrease with larger wavenumbers. Just inside the shear layer, two prominent intensity peaks are observed at the downstream ambient speed of sound wavenumber, and they emit their associated acoustic waves. The high-intensity distribution inside the jet shows a gradual decrease towards larger wavenumber values, this trend is also seen extending outside the shear layer, which is due to the convection of the fine-scale turbulence which can be seen in the downstream component of Figure 4.6(c).

In the previous discussion, the full wavenumber spectra were utilized to investigate all waves in the flow field showing the turbulent structures and their wave emissions. To study the noise generation mechanism of the sound emission wave packets from the flow field a reconstruction is carried out using only the ambient speed of sound wavenumber, this reconstruction suppresses the flow structures and shows waves propagating at the ambient speed of sound only (acoustic waves). The reconstructed sound field for both upstream and downstream propagating acoustic waves for the same frequencies of large-scale turbulent mixing noise, screech noise, and BBSAN noise are shown in Figure 4.8(a-c), respectively.

By examining the acoustic wave packets of the low frequency large mixing noise in Figure 4.8(a), it is found that the emitted acoustic intensity rapidly increases in the downstream direction, this is due to the rapid growth of the large scale turbulent structures traveling along the shear layer which was observed in Figure 4.6(a), in addition, as the waves propagate in the downstream direction, they acquire intensity contributions driven by the jet core as seen in the region 3<X/D<6.5 in Figure 4.8(a). The upstream wave component shows a disorganized pattern which could be due to detecting the upstream contribution from the spherical wave front generated from the downstream acoustic radiation. For the screech sound field in Figure 4.8(b), the acoustic wave emission is driven by high intensity sources inside the inner shear layer, which intensities increases in the downstream direction. This is consistent with the noise generation mechanism due to the interaction of the convecting coherent structures with the shock cells showing stronger interactions in the downstream direction due to the coherent structures' growth in the downstream direction. The upstream acoustic screech component shows intense noise radiation propagating upstream at shallow angle relative to the shear layer. The sources driving the upstream screech emission is indicated by the high intensity lobes inside the shear layer at axial location range 4<X/D<6.5 corresponding to the region between the fourth and seventh shock cells. Considering the sound field for at the higher frequency representing BBSAN in Figure 4.8(c), the downstream acoustic sources can be seen concentrated along the inner side of the shear layer each providing acoustic emission contributions that in forming the downstream acoustic radiation beam outside of the jet. For the upstream component of the BBSAN noise emission, the noise sources are in the vicinity of the shear layer, which is generated from the interaction of the turbulent structures with the shock cell tips. These sources produce the acoustic beam radiation for the BBSAN noise component.

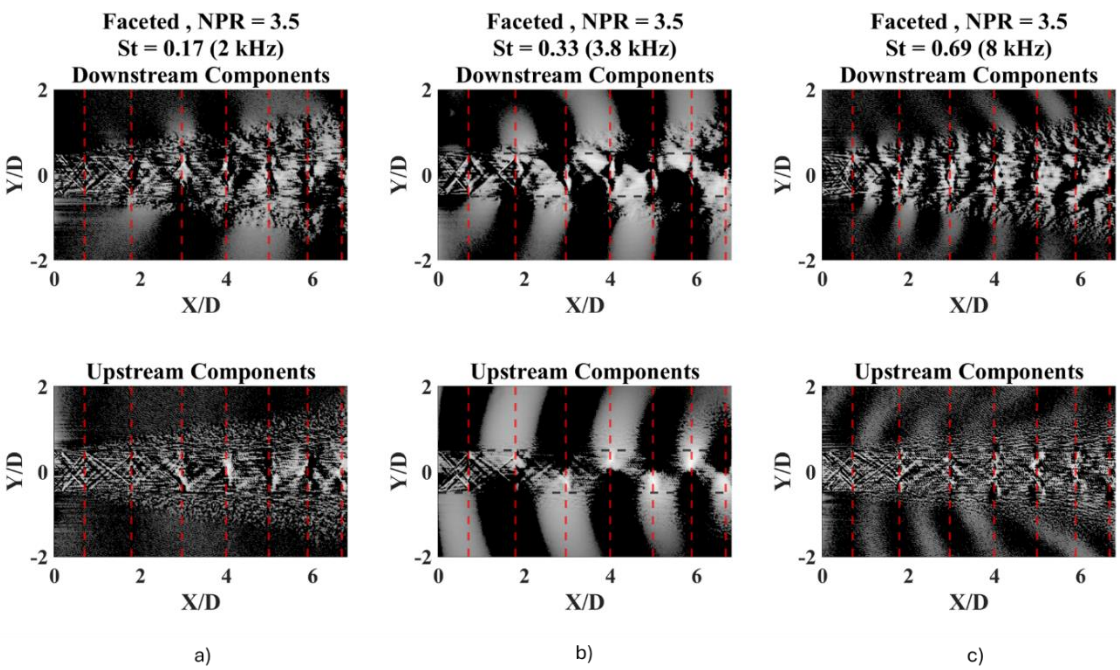

Figure 4.6: Fourier filtered flow field reconstruction at frequencies representative of a) large-scale mixing noise, b) screech, and c) high-intensity BBSAN. The reconstruction filters out all temporal Fourier modes except for the mode associated with the frequency of interest. The positive wavenumber spectra are used for downstream propagating components (top row), while the negative wavenumber spectra are used for the upstream propagating components (bottom row). The horizontal black dashed lines indicate the nozzle lip line and the vertical red dashed lines indicate shock cell tip locations. The results are for the baseline faceted nozzle, the nozzle operating condition is NPR=3.5.

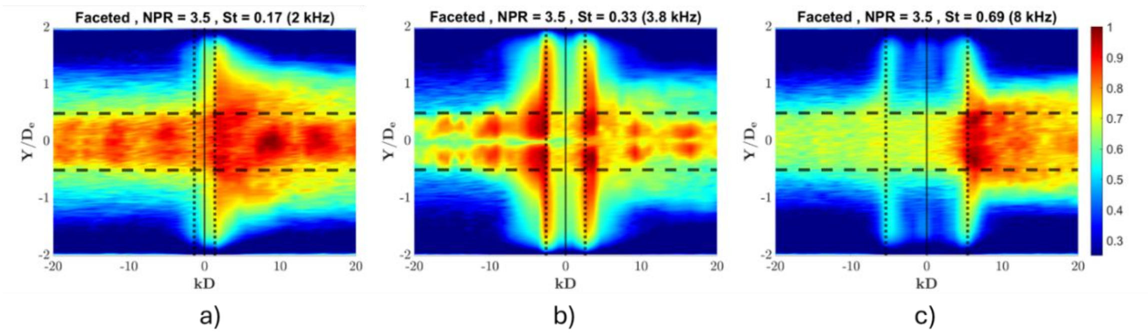

Figure 4.7: Radial distributions of axial wavenumber spectra at frequencies representative of a) large-scale mixing noise, b) screech, and c) high-intensity BBSAN. The results are for the baseline faceted nozzle at NPR=3.5. The vertical dotted black lines are for upstream (negative wavenumber) and downstream (positive wavenumber) acoustic wavenumber propagation. The horizontal dashed black lines indicate the top and bottom nozzle lip lines.

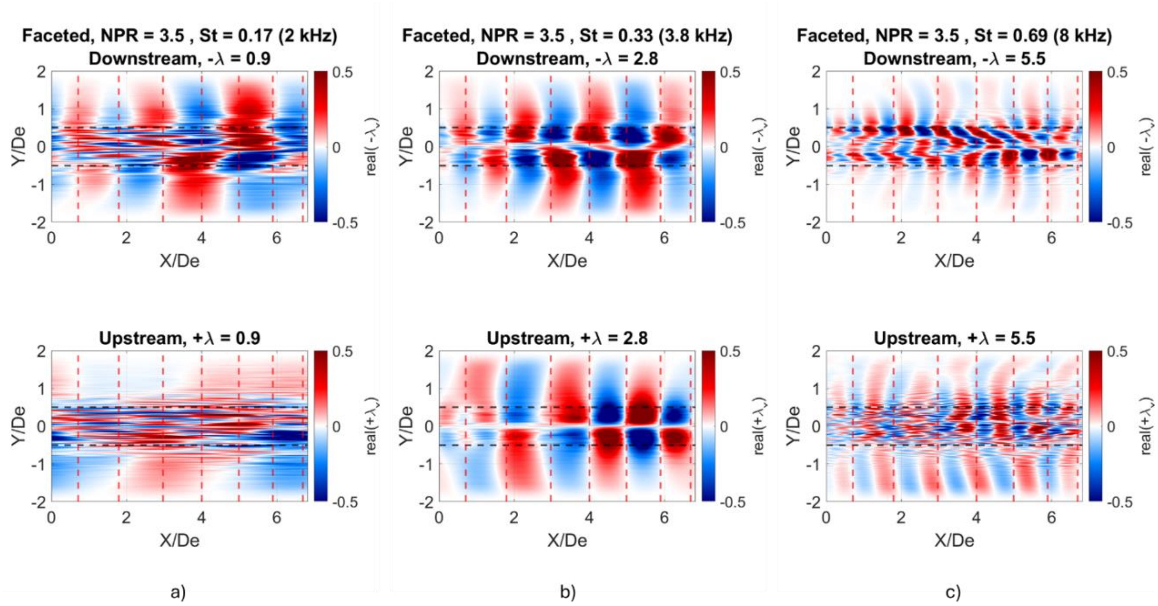

Figure 4.8: Acoustic wavenumber reconstruction at frequencies representative of a) large-scale mixing noise, b) screech, and c) high-intensity BBSAN. The reconstruction highlights the acoustic wave generation and propagation associated with the frequency of interest. The positive acoustic wavenumber is used for downstream propagating components (top row), while the negative acoustic wavenumber is used for the upstream propagating components (bottom row). The horizontal black dashed lines indicate the nozzle lip line and the vertical red dashed lines indicate shock cell tip locations. The results are for the baseline faceted nozzle, the nozzle operating condition is NPR=3.5.

Onset of screech:

In this subsection the onset of screech is studied. The spectral analysis methods discussed earlier is now applied for the baseline faceted nozzle at two operating conditions, a non-screeching jet at NPR=2.7 and the highly screeching jet at NPR=3.5 and the results are presented in Figure 4.9, Figure 4.10, and Figure 4.11. The selected frequencies correspond to the preferential jet instability mode and the screech frequency for the respective NPRs. In the Fourier filtered flow field contours of Figure 4.9(a), the non-screeching jet shows the formation of large turbulent coherent structures having a symmetric instability mode around the jet axis. Due to the smaller wavelength of the turbulent structures compared to the shock cell spacing, their interaction with the shock cells cannot emit upstream acoustic waves and therefore cannot induce jet resonance and no screech is produced. On the other hand, the highly screeching jet in Figure 4.9(b) produce large turbulent coherent structures undergoing an anti-symmetric mode oscillation having a wavelength of comparable size to that of the larger shock cell spacing produced by the jet at this NPR. Consequently, the interaction between the convecting coherent structures and the shock cells produces intense acoustic waves which influences the jet to undergo intense resonance and exhibit screech behavior.

Considering the radial distributions of the axial wavenumber in Figure 4.10(a), it is found that the internal upstream propagating waves show peak lobes with wavenumber larger than that of the ambient speed of sound wavenumber and hence cannot emit strong resonating acoustics for the non-screeching jet at NPR=2.7. On the other hand, for the screeching jet at NPR=3.5 dominant peak lobes with wavenumbers at and around the ambient speed of sound wavenumber are seen in Figure 4.10(b) causing the emission of strong acoustic wave intensities and driving the jet's resonance and screech.

Turning our attention to the acoustic wavenumber reconstruction, the sound field is presented in Figure 4.11(a). It is found that the downstream acoustic wavefronts are produced inside the shear layer and interacting with two shock cells due to their larger wavelengths, a similar effect is observed in the upstream acoustic sources interacting with two shock cell tips. Conversely, for the screeching jet in Figure 4.11(b) the acoustic sources are spaced apart to have wavelengths comparable to that of the shock cell spacing leading to the upstream acoustic sources being coherent and intensely energized by each shock cell tip at a time this is due to the optimal interaction of the turbulent structures with the each shock cell for screech generation.

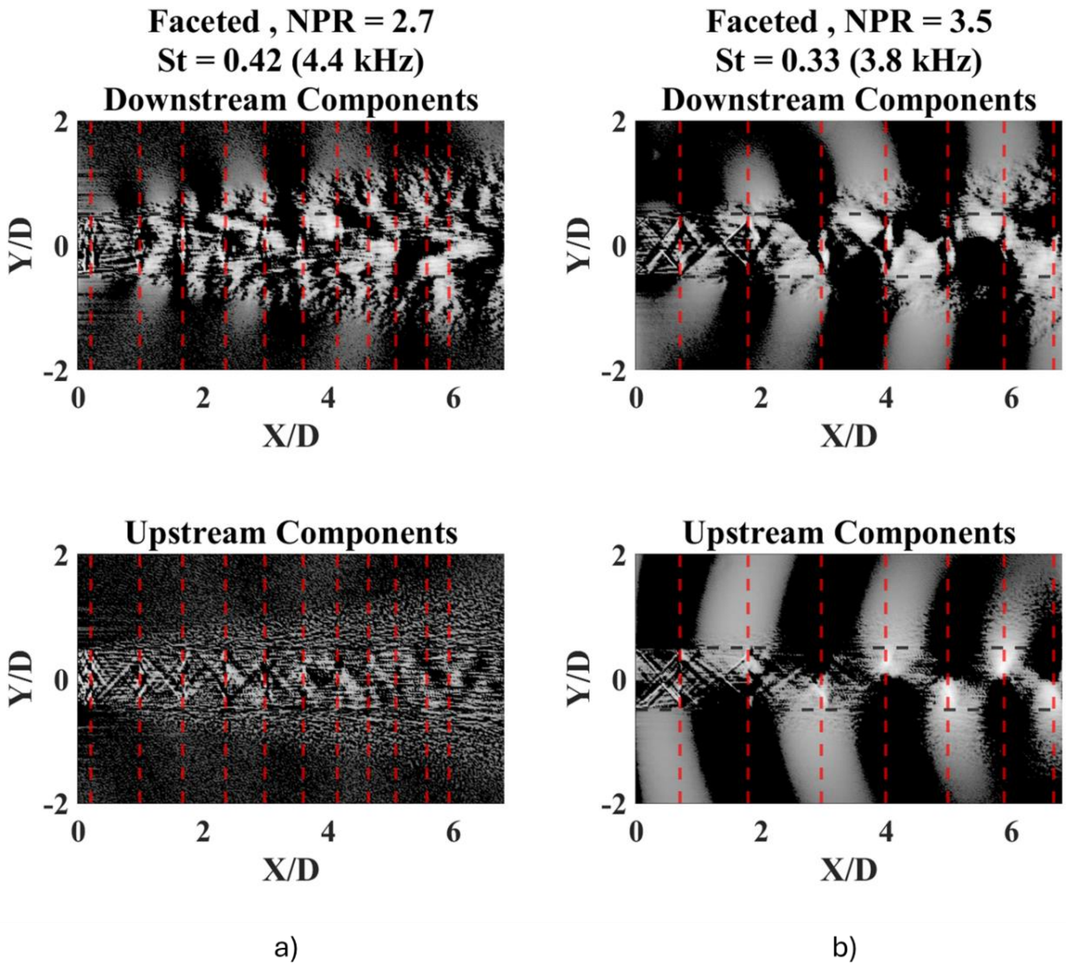

Figure 4.9: Fourier filtered flow field reconstruction at frequencies representative of preferential jet instability mode and jet screech. The reconstruction filters out all temporal Fourier modes except for the mode associated with the frequency of interest. The positive wavenumber spectra are used for downstream propagating components (top row), while the negative wavenumber spectra are used for the upstream propagating components (bottom row). The horizontal black dashed lines indicate the nozzle lip line, and the vertical red dashed lines indicate shock cell tip locations. The results are for the baseline faceted nozzle at operating conditions a) NPR=2.7, and b) NPR=3.5.

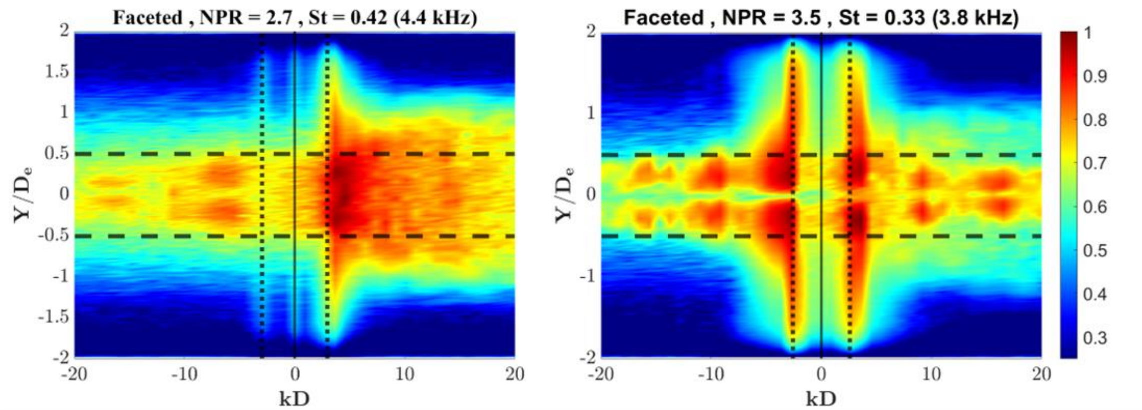

a) b)

Figure 4.10: Radial distributions of axial wavenumber spectra at frequencies representative of preferential jet instability mode and jet screech. The vertical dotted black lines are for upstream (negative wavenumber) and downstream (positive wavenumber) acoustic wavenumber propagation. The horizontal dashed black lines indicate the top and bottom nozzle lip lines. The results are for the baseline faceted nozzle at operating conditions a) NPR=2.7, and b) NPR=3.5.

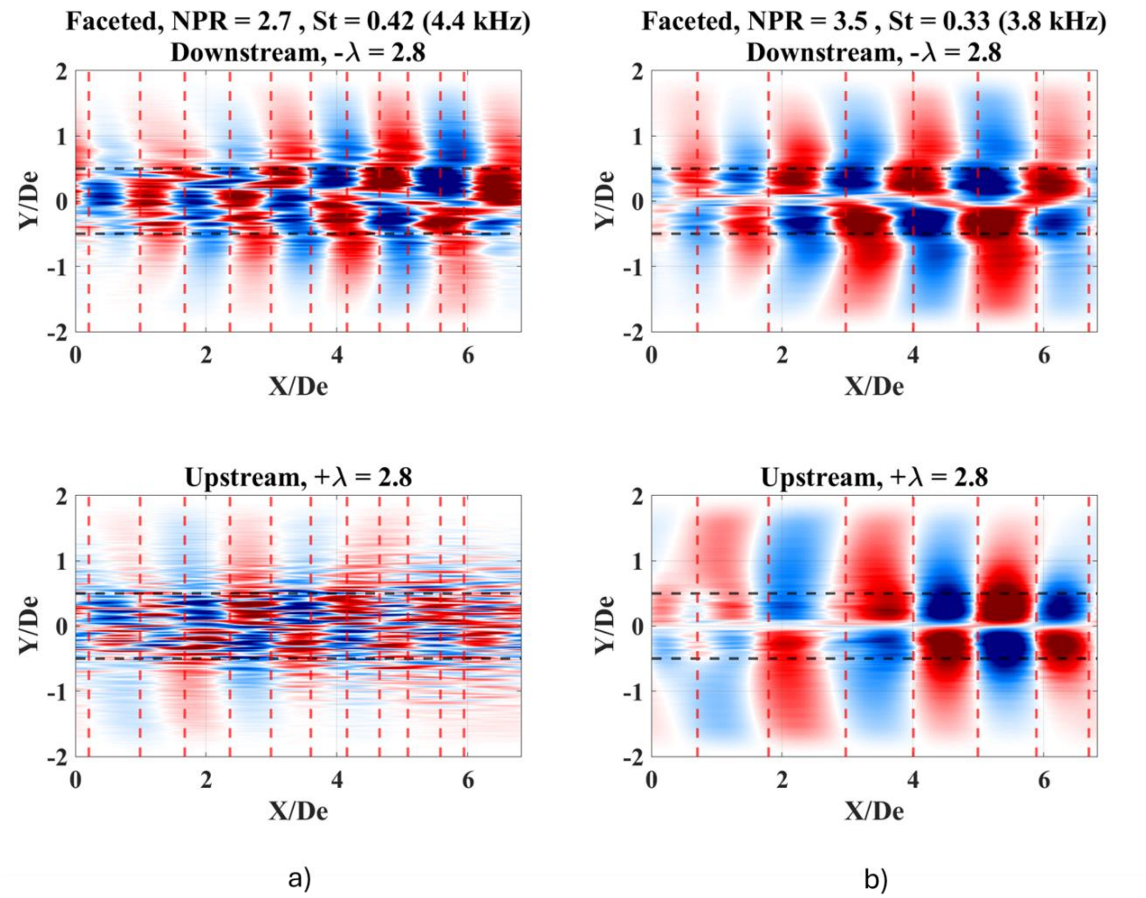

Figure 4.11: Acoustic wavenumber reconstruction at frequencies representative of preferential jet instability mode and jet screech. The reconstruction highlights the acoustic wave generation and propagation associated with the frequency of interest. The positive acoustic wavenumber is used for downstream propagating components (top row), while the negative acoustic wavenumber is used for the upstream propagating components (bottom row). The horizontal black dashed lines indicate the nozzle lip line and the vertical red dashed lines indicate shock cell tip locations. The results are for the baseline faceted nozzle at operating conditions a) NPR=2.7, and b) NPR=3.5.

Impact of MVGs

In this subsection the impact of MVGs on the jet is investigated by comparing the radial wavenumber distributions and the generated sound field of the various jets at the moderately screeching condition of NPR=3.0 as it is representative of the other operating conditions. The frequencies of interest are the same as before representing the peak noise components of the large-scale turbulent mixing noise, Screech, and BBSAN, and are presented in Figure 4.12 to Figure 4.17.

Figure 4.12 shows that for the large-scale mixing noise frequency, MVGs cause the lobes of peak intensities to shift towards larger wavenumber values in both upstream and downstream directions. This is because the MVGs break down the large coherent structures into smaller scales which has a weaker effect on perturbing the shock cells at the collapsing end of the potential core leading to slower shock cell oscillations. This effect leads to reduced sound emission efficiency of the dominant lobe peaks inside the jet. The reason for this change is that MVGs cause the reduction of jet velocities as well as increased mixing of the shear layer, where the coherent structures are smaller and convecting at lower velocities causing the reduced efficiency in mixing noise generation in the downstream direction.

Examining the sound field in Figure 4.13 shows that the growth rate of the emitted acoustic waves of the large mixing noise component is substantially decreased for the MVG cases where the wavelengths of the radiated sound wave packets are reduced for the single array MVG and further reduced for the double array MVG nozzle, this effect is due to the breakdown of the large scale coherent structures responsible for this noise emission.

The impact of MVG nozzles on the radial wavenumber distributions at the screech frequency is presented in Figure 4.14, which shows that the upstream propagating peak lobes of the internal guided jet mode have shifted to larger wavenumbers away from acoustic wavenumber value, hence substantially weakening the acoustic emissions for the single array MVG and completely suppressing it for the double array MVG configuration. Additionally, the wavenumber distributions of the shear layer in the downstream direction have been distributed over a larger wavenumber range which distributes its energy over a wider range of turbulent scales and hence reduces their downstream mixing noise generation efficiency. These effects can also be seen in the sound field of these nozzles in Figure 4.15, where the strong jet resonance of the baseline jet has been reduced for the single array MVG configuration due to weaker downstream and upstream acoustic wave emissions. The reduced acoustic wave emissions in the downstream is due to MVGs breaking down the shear layer coherent structures and reducing their convecting velocity resulting in weaker downstream acoustic emissions, additionally, these weakened structures will have a weaker interaction with the weakened shock cells producing lower intensity upstream acoustic waves which impact the screech resonance by substantially reducing it. This effect is much stronger for the double array MVG nozzle leading to screech suppression.

Figure 4.16 examines the impact of MVGs on the radial distribution of wavenumber spectra at the BBSAN frequency, which shows the same mechanism described above, where MVGs disperse the energy content over wider wavenumbers corresponding to redistributing the turbulence fluctuation energy to a wider range of turbulent scales along the shear layer. in doing so, the efficiency of the downstream noise efficiency is reduced, and combined with the weaker shock cells their interaction with the turbulent structures produces weaker upstream shock noise resulting in lower emissions.

The reconstructed sound field in Figure 4.17 clearly shows reductions in upstream propagating shock noise emissions. Where the baseline nozzle shock strong acoustic wave packets being emitted along the entire shear layer, whereas the single array MVGs show emission reductions for most of the shear layer except for high emissions towards the end of the jet. On the other hand, the double array MVG nozzle shows substantially lower acoustic emissions in the upstream region of the jet 0<X/D<4 .

The reductions in acoustic emissions discussed in this section will have a direct impact on reducing the acoustic noise radiation into both the acoustic near field and the acoustic far field and will be discussed in the following section.

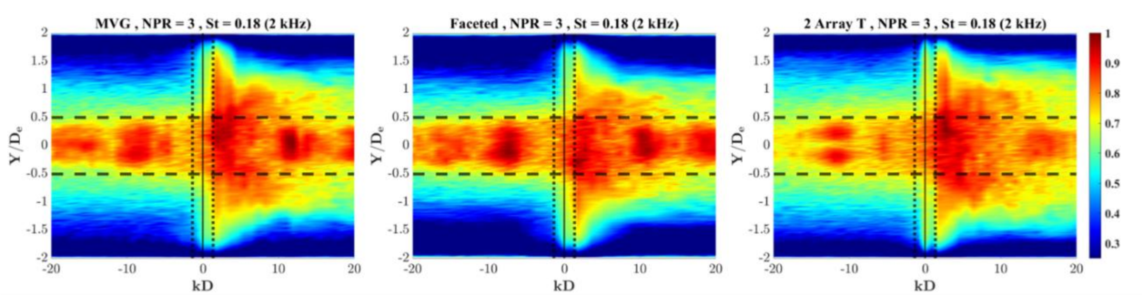

a) b) c)

Figure 4.12: Comparisons of radial distributions of axial wavenumber spectra at a frequency representative of large-scale mixing noise for various nozzle configurations a) baseline faceted, b) single array MVG, and c) double array MVG nozzles. The jet operating condition is NPR=3.0. The vertical dotted black lines are for upstream (negative wavenumber) and downstream (positive wavenumber) acoustic wavenumber propagation. The horizontal dashed black lines indicate the top and bottom nozzle lip lines.

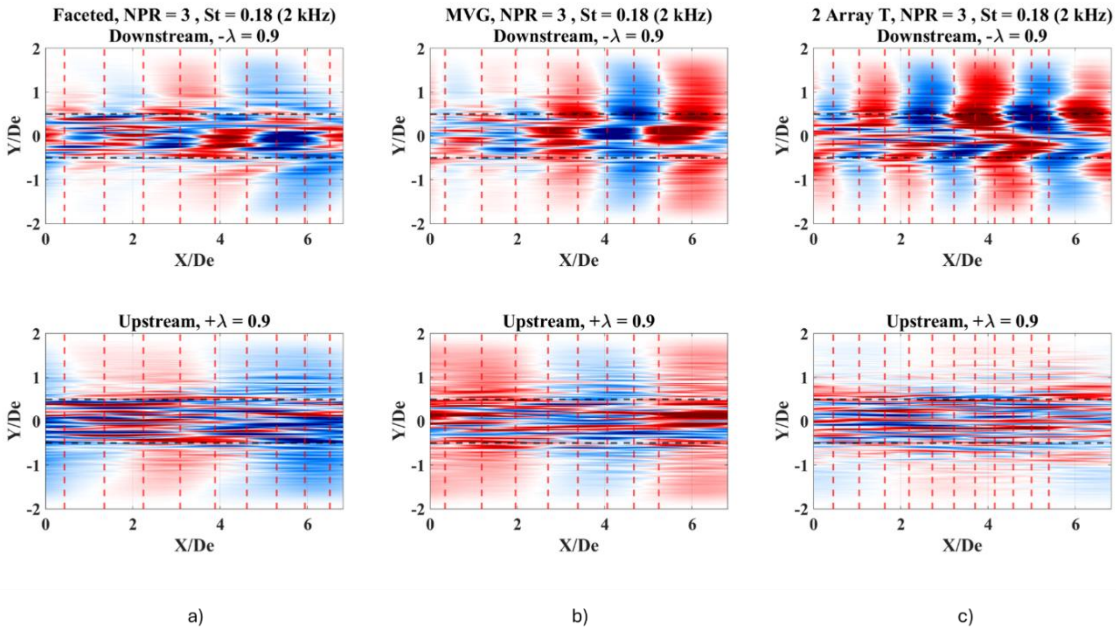

Figure 4.13: Comparisons of acoustic wavenumber reconstruction at a frequency representative of large-scale mixing noise for various nozzle configurations a) baseline faceted, b) single array MVG, and c) double array MVG nozzles. The jet operating condition is NPR=3.0. The reconstruction highlights the acoustic wave generation and propagation associated with the frequency of interest. The positive acoustic wavenumber is used for downstream propagating components (top row), while the negative acoustic wavenumber is used for the upstream propagating components (bottom row). The horizontal black dashed lines indicate the nozzle lip line and the vertical red dashed lines indicate shock cell tip locations.

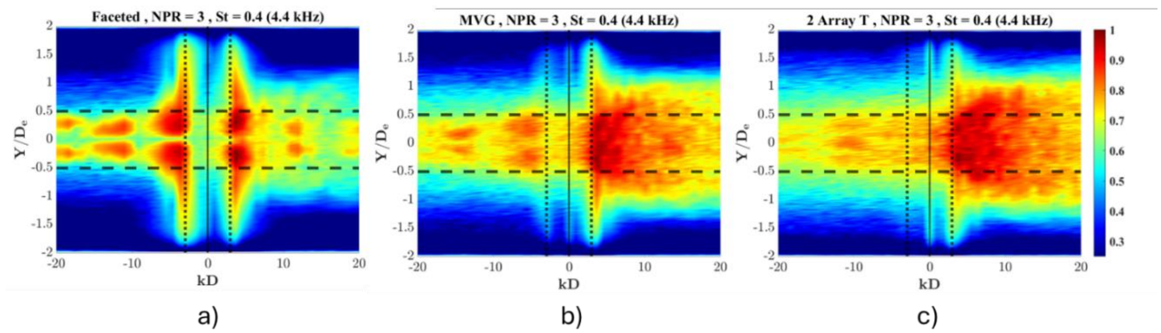

Figure 4.14: Comparisons of radial distributions of axial wavenumber spectra at a frequency representative of screech noise for various nozzle configurations a) baseline faceted, b) single array MVG, and c) double array MVG nozzles. The jet operating condition is NPR=3.0. The vertical dotted black lines are for upstream (negative wavenumber) and downstream (positive wavenumber) acoustic wavenumber propagation. The horizontal dashed black lines indicate the top and bottom nozzle lip lines.

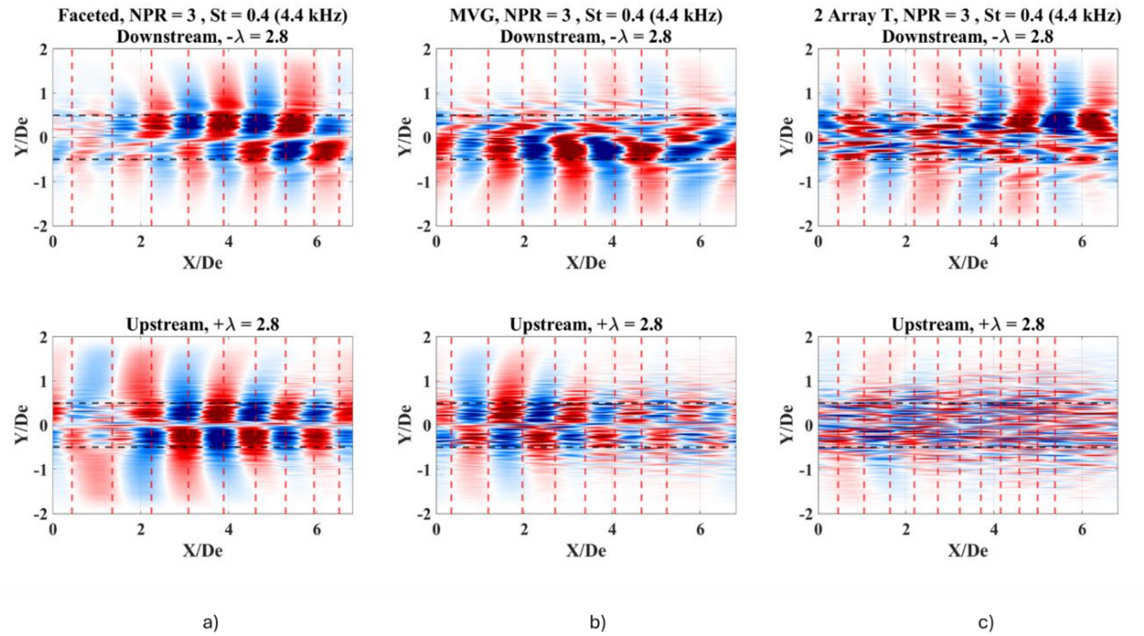

Figure 4.15: Comparisons of acoustic wavenumber reconstruction at a frequency representative of screech noise for various nozzle configurations a) baseline faceted, b) single array MVG, and c) double array MVG nozzles. The jet operating condition is NPR=3.0. The reconstruction highlights the acoustic wave generation and propagation associated with the frequency of interest. The positive acoustic wavenumber is used for downstream propagating components (top row), while the negative acoustic wavenumber is used for the upstream propagating components (bottom row). The horizontal black dashed lines indicate the nozzle lip line and the vertical red dashed lines indicate shock cell tip locations.

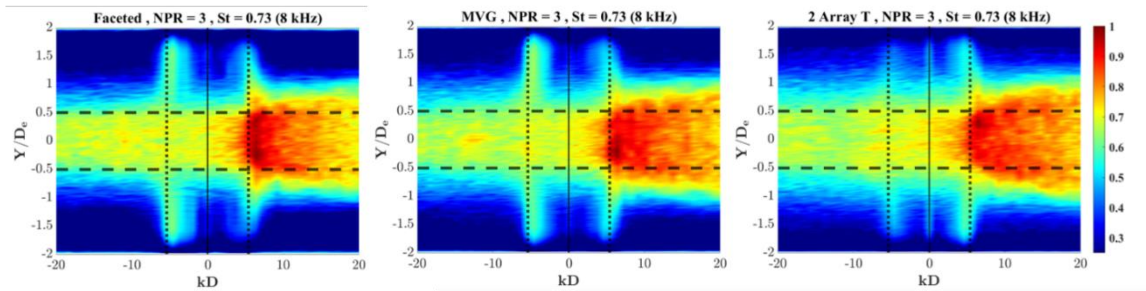

a) b) c)

Figure 4.16: Comparisons of radial distributions of axial wavenumber spectra at a frequency representative of BBSAN noise for various nozzle configurations a) baseline faceted, b) single array MVG, and c) double array MVG nozzles. The jet operating condition is NPR=3.0. The vertical dotted black lines are for upstream (negative wavenumber) and downstream (positive wavenumber) acoustic wavenumber propagation. The horizontal dashed black lines indicate the top and bottom nozzle lip lines.

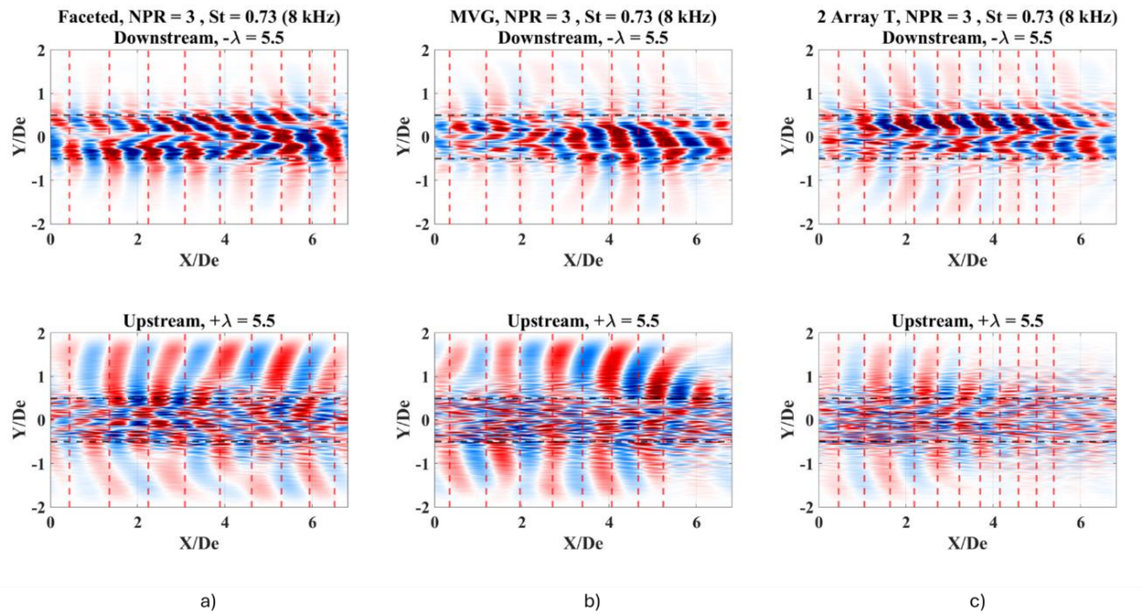

Figure 4.17: Comparisons of acoustic wavenumber reconstruction at a frequency representative of BBSAN noise for various nozzle configurations a) baseline faceted, b) single array MVG, and c) double array MVG nozzles. The jet operating condition is NPR=3.0. The reconstruction highlights the acoustic wave generation and propagation associated with the frequency of interest. The positive acoustic wavenumber is used for downstream propagating components (top row), while the negative acoustic wavenumber is used for the upstream propagating components (bottom row). The horizontal black dashed lines indicate the nozzle lip line and the vertical red dashed lines indicate shock cell tip locations.

NEAR AND FAR FIELD ACOUSTICS:

This section studies the noise reductions observed in the flow field and acoustic emissions and how they propagate into the acoustic near-field and subsequently into the far-field. Figure 4.18 shows contour plots comparing the near-field acoustic measurements for the various nozzle configurations at the same frequencies discussed earlier for representing frequencies of peak noise components of the low-frequency large-scale mixing noise, screech, and BBSAN, and is shown for NPR=3.0. In addition, the far-field acoustic SPL spectral measurements are shown for the same nozzle configurations and presented in Figure 4.19(a-c) for the main observation angles of 40, 90, and 150 degrees corresponding to upstream, sideline, and downstream observation directions, respectively. At the low-frequency large mixing noise frequency, it is found that the baseline nozzle produces the largest acoustic noise emissions with a main lobe showing directivity towards the downstream direction. On the other hand, the single array MVG nozzle shows a significant reduction in noise levels for this noise component, and further reductions are seen for the double array MVG nozzle configuration. The observed reductions in mixing noise components are consistent with the earlier discussions, where the MVGs cause reductions in the jet velocity and its shear layer conveting structures' scale and convection velocity which was observed to influence the peak wavenumber distributions to shift to larger values, resulting in weaker acoustic wave emission that was observed in Figure 4.13. These reductions are also observed for this noise component propagating into the far-field acoustic measurements as the low-frequency peak SPL values are reduced for the single array MVG and further reduced for the double array MVG as shown in Figure 4.19(c) for the microphone located at the downstream observation angle of 150 degrees.

At the screech frequency, the baseline faceted jet shows two high-intensity lobes in the near-field noise distribution directed towards the upstream and downstream directions [second row of Figure 4.18(a)]. For the single array MVG nozzle, the intense upstream propagating noise lobe is significantly reduced and suppressed for the double array MVG nozzle [second row of Figure 4.18(b, c)]. This effect is directly related to the weaker sound emission in the upstream sound field discussed earlier in Figure 4.15. In addition, the downstream lobe of the near-field acoustics shows reductions in noise levels for the MVG nozzles, which is consistent with the redistribution in turbulence wavenumbers. The impact of screech reduction and suppression can be clearly seen in the upstream observation angle of the far-field spectra in Figure 4.19(a), where the dominant screech peak of the baseline nozzle (blue line) is seen reduced for the other MVG nozzles (green and red lines). As discussed earlier, this reduction is caused by the changes in wavenumber spectral distributions of the flow field leading to weaker interactions of smaller turbulent structures with the weakened shock cells observed in the MVG nozzles.

Considering the selected BBSAN frequency, the near-field contours show two distinct lobes with the upstream lobe having significantly higher intensity than the downstream lobe for the baseline nozzle. This is because the upstream shock noise emission is significantly stronger than the downstream noise emission at this frequency. The single MVG nozzle shows noise intensity reductions in the upstream lobe of the emitted shock noise, while the double array MVG nozzle shows more significant reductions in that lobe. These reductions are due to reduction is acoustic wave emission observed in Figure 4.17, which resulted from the weakening of the shock cells and their weaker interaction with the smaller turbulent structures convecting along the shear layer of the MVG nozzles. The acoustic noise reductions in the near field at the selected BBSAN frequency is also observed in the acoustics propagating to the far-field measurements and is clearly seen in the spectra of the upstream and sideline observation directions in Figure 4.19(a, b).

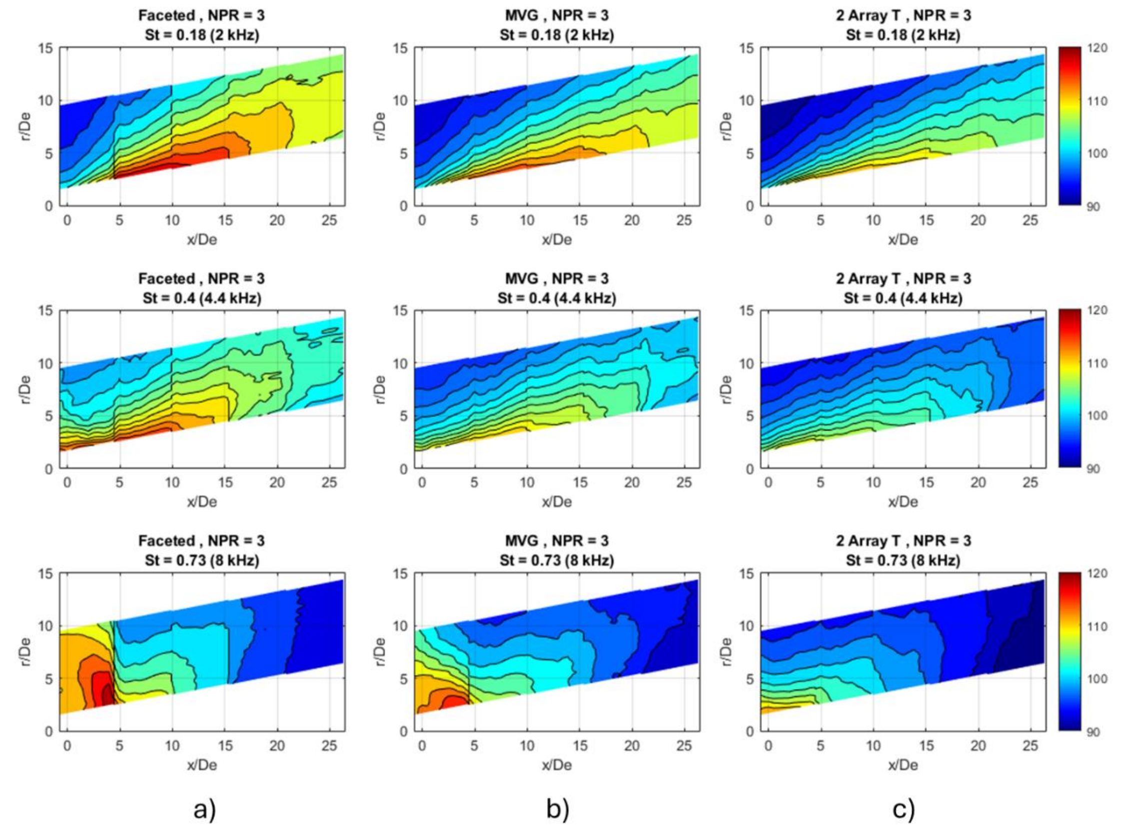

Figure 4.18: Comparisons of the near-field acoustic distributions for the various nozzle configurations a) baseline faceted, b) single array MVG, and c) double array nozzle configuration. The contours show sound pressure levels (SPL) at frequencies representative of large-scale mixing noise (first row), screech (second row), and high-intensity BBSAN (third row). The nozzle operating condition is NPR=3.0.

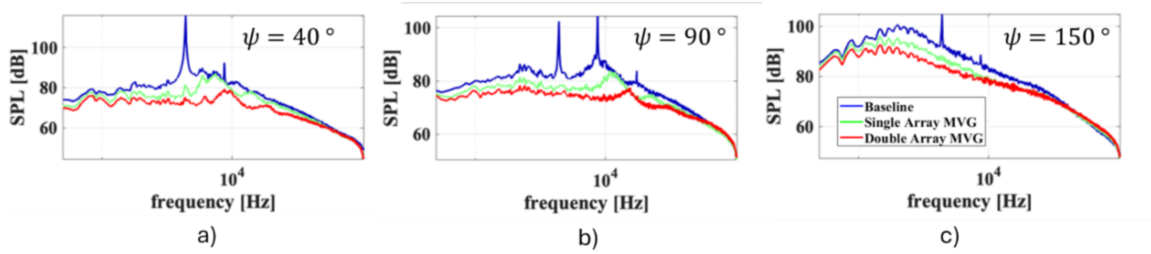

Figure 4.19: Comparisons of sound pressure level (SPL) spectra for the various nozzle configurations of baseline faceted, single array MVG, and double array nozzle configuration. The results are shown for microphones at observation angles a) 40 degrees (upstream), b) 90 degrees (sideline), and c) 150 degrees (downstream). The nozzle operating condition is NPR=3.0.

DIRECTIVITY AND GENERATION MECHANISMS OF SHOCK NOISE

Supersonic jets show distinct noise radiation directivity for the shock noise components including the screech tone and the BBSAN. Since the screech tone is a special case of BBSAN, its directivity mechanism is similar to that of BBASN and it is a function of acoustic wave interference patterns. In this section the purely BBSAN directivity and generation mechanism is studied for the non-screeching baseline jet at NPR=2.7, this condition is chosen to avoid any screech effect that can influence the shock noise generation mechanism.

BBSAN Directivity

For a given shock containing supersonic jet, its emitted broad band shock associated noise BBSAN shows a variation in its peak noise radiation direction as a function of frequency, this effect is known as BBSAN directivity. In this subsection, the underlying mechanism of BBASN directivity is studied. To understand how variations in BBSAN frequency causes a change in peak radiation directivity for specific frequencies it is necessary to filter out all frequencies except for the frequency of interest. Figure 4.20(a-c) shows contours of the Fourier filtered flow field at BBSAN frequencies of f=7.7, 11.3, and 25.3 kHz, respectively. These frequencies are chosen based on the peak BBSAN frequencies from the far-field acoustic measurements at observation angles of 40, 90, and 130 degrees.

At the lower BBSAN frequency, Figure 4.20(a) shows that the jet emits high intensity acoustic wave packets with intense radiation beams propagating along the jet in the downstream direction that are generated from turbulent mixing noise at this frequency in the initial region of the jet up to X/D=2.5, after that a radiation interference pattern emerges resulting in two radiation directivities as indicated in the figure with the red and cyan arrows. For the higher intensity radiation pattern propagating in the upstream direction, an intense radiation beam is observed propagating primarily in the upstream direction at a shallow angle relative to the jet axis as indicated by the red arrow. In addition, a faint radiation beam that dissipates can be seen as indicated by the cyan arrow. The combined effect of the downstream and upstream radiation beams give rise to the noise distribution which can be seen in the near field acoustic measurement in Figure 4.21(a), and it shows two distinct radiation lobes with the upstream lobe having a higher noise intensity levels compared to the downstream lobe. This upstream lobe propagates to the acoustic far-field and is clearly detected as high intensity BBSAN peak at the microphone with observation angle of 40 degrees in Figure 4.22.

Figure 4.20(b) shows the BBSAN wave emissions at the mid frequency range of f=11.3kHz, where the acoustic beam radiation has split into multiple radiation beams for both upstream and downstream propagation direction. This effect is due to reductions in the radiation wavelengths which makes the radiation beams exhibit constructive and destructive interference. The interference patterns emerge due to variation in the phase oscillations of the various acoustic sources. The downstream beam radiation interference patterns emerge from the phase change in the spatial coherence of the convecting turbulent structures, whereas the upstream beam radiation interference patterns originate from the phase delay at each shock cell tip interaction with the turbulent structures. Since the radiation wavelength is reduced at the higher frequency, its acoustic emissions energy is reduced because they are emitted from smaller turbulent structures and their weaker interactions with the shock cell tips, this leads to lower BBSAN noise intensity generation at higher BBSAN frequencies. This effect is compounded with the splitting of the main radiation lobe into multiple radiation lobes and their interference effect, where regions of destructive interference will lose acoustic energy. Both these effects drive the BBSAN radiation energy to lower noise levels at higher frequencies. This effect is clearly seen in the near-field distribution shown in Figure 4.21(b), which shows reduced SPL levels and a change in lobe radiation directivity towards the sideline at 90 degrees. In addition, the emitted noise from this directivity reaches the far-field where the peak BBSAN noise levels at this frequency is prominent at the microphone with observation angle of 90 degrees as shown in Figure 4.22.

At the highest BBSAN frequency (f=25.3kHz), the acoustic radiation wavelengths become even smaller, and the acoustic radiation is split into four radiation beams propagating in the downstream direction and five radiation beams propagating in the upstream direction. The multi radiation beams show destructive interference patterns between them. Due to the increase in radiation beams at the higher BBSAN frequency, their effective radiation directivity show an almost omni-directional acoustic radiation, this combined with the lower acoustic energy that can be carried by the acoustic beams leads to the reduction in SPL with omni-directional distribution pattern as seen in Figure 4.21(c).

At this BBSAN frequency, the noise propagating to the far-field shows a diminished BBSAN peak at the microphone with observation angle of 130 degrees. After this angle the higher frequency contents no longer show distinctive BBSAN hump in the acoustic spectra.

From this discussion the mechanism responsible for the BBSAN directivity change as a function of frequency is due to constructive and destructive interference from the phase delay of the acoustic radiation sources. Hence, the noise sources exhibit a phased array behavior which drives the BBSAN directivity pattern based on the frequency and the phase delay of the sources.

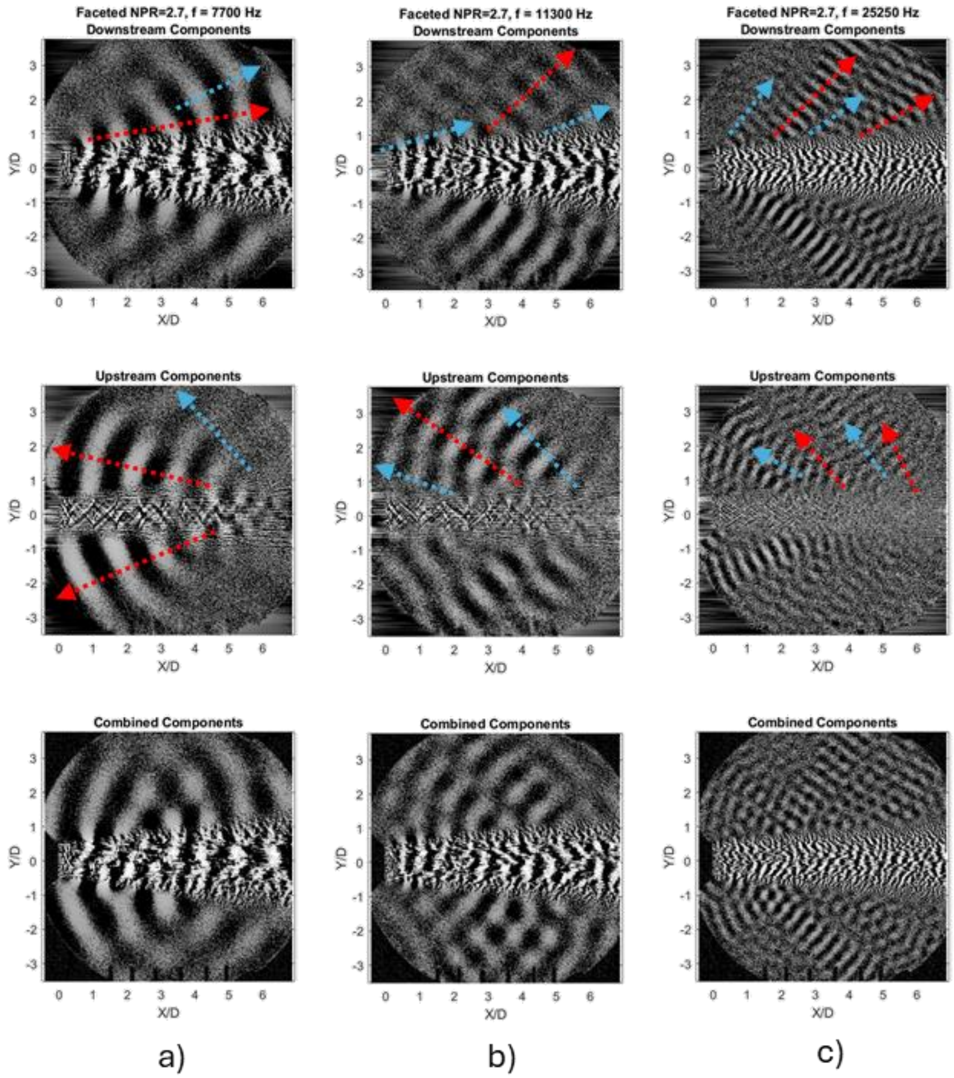

Figure 4.20: Fourier filtered flow field reconstruction at various BBSAN frequencies representative of peak noise emission directivity towards a) upstream, b) sideline, and c) downstream directions for low, mid, and high BBSAN frequency values. The dotted arrows indicate the noise radiation directions. The reconstruction filters out all temporal Fourier modes except for the mode associated with the frequency of interest. The reconstruction shows the downstream propagating wave components using positive wavenumbers (first row), the upstream propagating wave components using negative wavenumbers (second row), and the combined upstream and downstream wave components (third row). The results are for the baseline faceted nozzle, the nozzle operating condition is NPR=2.7.

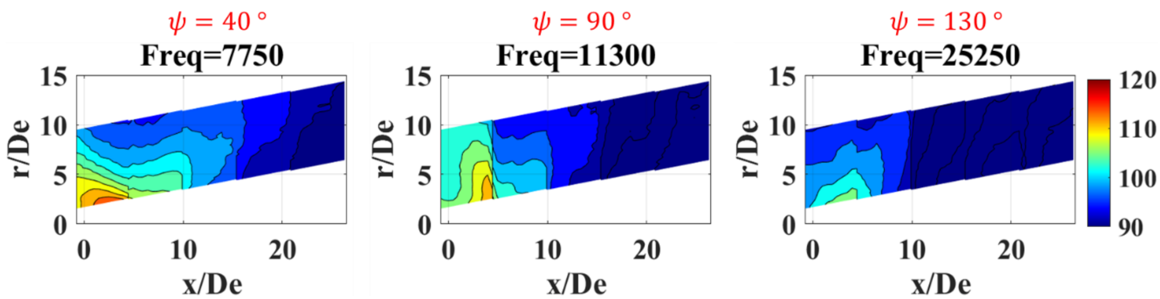

Figure 4.21: Near-field microphone measurements showing Sound Pressure Levels (SPL) distributions at frequencies corresponding to peak BBSAN radiation directivity as identified from the far-field spectra for a) 40 degrees (upstream), b) 90 degrees (sideline), and c) 130 degrees (downstream) observation angles. The results are for the baseline faceted nozzle at operating condition NPR=2.7.

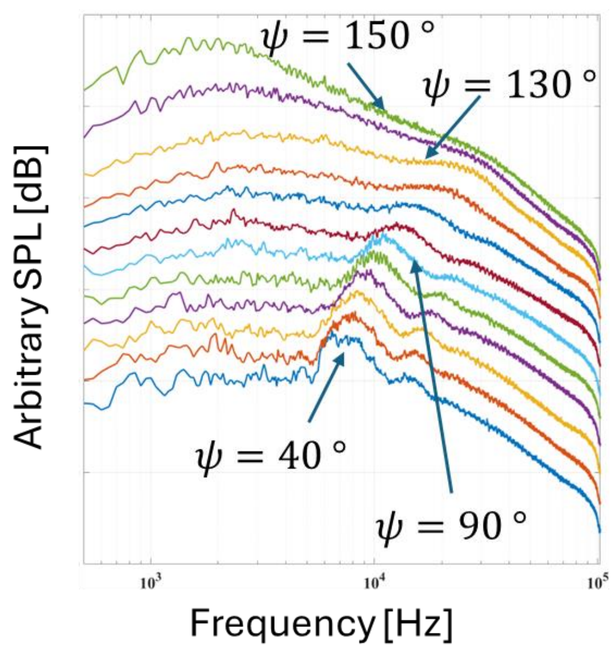

Figure 4.22: Far-field Sound Pressure Level(SPL) spectra at observation angles 40 degrees (lower curve) to 150 degrees (upper curve). The various microphone spectra are stacked vertically to aid in visuals. The results are for the baseline faceted nozzle at operating condition NPR=2.7. The plot demonstrates the change in peak BBSAN directivity in frequency and amplitude as a function of the observation angle.

Shock vortex interaction and BBSAN noise generation mechanisms:

In this subsection the physical flow phenomena responsible for the generation mechanisms of shock noise particularly BBSAN is uncovered. The flow field is probed by zooming into the shock cell tips using shadowgraph imaging to directly visualize the shock behavior in producing BBSAN. Also, Schlieren visualization is utilized with various analysis methods to develop a dynamic model that covers the main aspects of the shock noise generation mechanism.

To observe the shock vortex interaction responsible for the BBSAN noise generation, high speed shadowgraph imaging in a region around the shock cell tip in supersonic jet is presented in [Figure 4.23 (t1-t4)]. The figure shows four successive snapshots from t1 to t4 to track the dynamics of the shock cell tip interacting with shear layer vortices. The top row of the figure shows a closeup view with the red curves tracing the shock tip boundary taken from the second row of the figure. In a turbulent shear layer, the turbulence and vortices cause the shear layer's convective velocity to maintain strong velocity fluctuations, this causes the shock tips to respond to the local velocity and momentum fluctuations. Where a higher momentum flow packet would cause the local shock to become stronger and tilt backwards in the downstream flow direction [Figure 4.23 (t1)], as the vortical structure passes and clears the shock tip, the shock tip recoils and can over shoot [Figure 4.23 (t2)], if the incoming flow perturbation is slower than the mean local velocity in a way that the shock can overcome it and tilt upstream against the flow direction [Figure 4.23 (t3)], the shock tip will transition into an acoustic wave where it gets separated from the shock tip and propagate into the ambient as sound waves [Figure 4.23 (t4)].

The sound generation dynamics are schematically represented in Figure 4.24(a-d) which captures the sequence of events. This starts with a shear layer vortical structure approaching a shock cell tip and interacts with it, this causes the generation two reflected shocks R1 propagating inside the jet core, while the second reflected shock R2 propagates into the ambient and becoming a sound wave, the second vortical structure follows the same mechanism and generating two additional reflected shocks indicated by R3 and R4. This sequence of events continues to repeat for successive convecting vortical structures.

The sound waves generated from the shock vortex interaction discussed earlier causes the formation of multiple acoustic wavefront that propagate along the shear layer towards the upstream direction. Since, the shear layer is considered as a contact surface in equilibrium with equal pressure on both sides, the local static pressure inside the shear layer is equal to the ambient pressure outside the shear layer, the acoustic wavefront passing along the shear layer will cause a pressure perturbation whose effect will cause the generation of internal waves inside the jet being initiated at the root location of the external acoustic wave on the shear layer. As the acoustic waves propagate in the upstream direction, the internally generated trapped waves will follow the disturbance of the acoustic waves on the shear layer. This effect can be seen in Figure 4.25, showing the wave reconstruction and its phase angles. From these contours a clear cross hatch pattern emerges inside the jet and is synchronized by the external acoustic waves as the internal waves follow their path of propagation to the upstream of the jet flow.

The proposed BBSAN and internal trapped waves generation mechanism is shown schematically in Figure 4.26, where the sequence of events is:

1- Sound waves generated from shock vortex interaction propagate externally along the shear layer towards the upstream direction and causes a pressure perturbation on the shear layer contact surface which influence reaches the inside of the shear layer.

2- This perturbation causes the generation of internal trapped waves propagating in the upstream direction inside the jet core and has a region of influence reaching the opposite side of the shear layer and synchronizes the interaction of vortex shock interaction on the opposite side of the shear layer.

3- The synchronized shock vortex interaction of the opposite side of the shear layer controls the phase of the newly formed acoustic wavefronts, and the same dynamics discussed from 1-3 repeat to synchronize the top side of the shear layer creating a feedback loop mechanism.

The BBSAN noise generation mechanism exhibits a turbulent/ vortical structure coherence that travels along the shear layer covering the BBSAN frequency spectra. These coherent structures interact with the shock cell tips at multiple locations to emit shock noise which show high levels of acoustic intensities due to constructive interference from the multiple emission sources which is facilitated by phase locking the turbulence coherence with the shock noise acoustic waves. This phase locking mechanism is a result of the shear layer modulation of the smaller turbulent structures to merge and form larger vortical structures and is known as "collective interaction" and was studies by Ho & Nosseir[35] where they show that the coherence is driven by a forcing of the shear layer. In the current study, we show that this is indeed the case where the shear layer instability is amplified by acoustic forcing emitted by the BBSAN mechanism. This drives the shear layer instability to undergo modulation to form coherent vortical structures that convect in the downstream direction, these structures subsequently interact with the shock cell tips to generate additional shock noise propagating upstream and sustaining the shear layer modulation forming a closed feedback loop. These effects are clearly seen in the filtered Fourier flow field contours in Figure 4.27(a), where it shows the impact of shear layer modulation by forming organized acoustic wave packets emitting into the ambient to the downstream direction which are also phase locked with the emitted upstream propagating shock noise at various BBSAN frequencies. The phase locking of the coherent vortical structures allows the shock tips to generated acoustic emissions that interfere constructively with subsequent shock cell tips, this effect is clearly seen by the upstream acoustic wave packets having wavelengths with harmonics and sub-harmonics being emitted at each shock cell location.

To aid in visualizing these effects and how the mechanism works, wavefronts are traced from the filtered flow field and are shown schematically in Figure 4.27(b). The first schematic shows the combined upstream and downstream waves. The second schematic shows the downstream component being emitted as mixing noise from the convecting coherent vortices and show two radiation beams due to interference effects from the vortices having different coherence at two regions along the shear layer for this specific frequency. The third schematic shows that these conveting structures interact with the shock cells and produce upstream shock noise having two distinct radiation beams due to interference effects from the change in coherence experienced by the conveting vortices.

From this discussion a model can be developed for the shear layer modulation and is shown schematically in Figure 4.28. Figure 4.28(a) shows a contact surface/ shear layer where the pressure gradient across its boundary is zero, i.e. the pressure acting on both sides of the shear layer is equalized, also shown is a traveling acoustic wave front having a non- zero pressure gradient i.e. an acoustic pressure perturbation. At the root of the interface between the shear layer and the acoustic wave foot, the shear layer is perturbed with a finite pressure jump delta p which will cause the supersonic jet flow and the shear layer to react accordingly. The slight increase in local pressure would be experienced by the incoming internal jet flow causing it to initially turn away from the shear layer and form a Mach wave. As the external acoustic wave passes, the local shear layer boundary would experience a pressure imbalance and return to its initial equilibrium by forming expansion waves internally and steering the jet flow towards the shear layer and eventually the jet flow becomes parallel to the shear layer. This interaction causes a “bump” in the shear layer forcing for the collective interaction, that would drive the modulation of the shear layer to form coherent vortices. When multiple synchronized acoustic waves pass over the shear layer as shown in Figure 4.28(b), the effect is repeated to form a modulated shear layer with repeated coherent vortices traveling in the downstream direction passing through the opposing upstream acoustic waves successively. As the newly formed coherent vortical structures travel in the downstream direction, they interact with additional perturbations from the incoming successive acoustic waves, and the vortical structures experience additional phase locked perturbations causing them to grow as they convect in the downstream direction. The increase in growth rate of the downstream convecting vortical structures increases their mixing noise generation efficiency allowing them to emit stronger mixing noise radiating downstream as shown in the last schematic in Figure 4.28(c).

Integrating the various aspects of BBSAN noise generation mechanisms discussed so far, an overall BBSAN generation mechanism and feedback loop is proposed which encompasses the following steps:

1) An initial shear layer instability is formed and propagates along the shear layer as a vortical structure. This vortical structure interacts with the tip of a shock cell leading to the generation of two reflected shock waves. The external shock reflection transitions into an acoustic wave as it propagates into the ambient towards the upstream direction along the shear layer.

2) The upstream propagating acoustic waves causes a perturbation of the shear layer leading to a modulation forcing that causes the formation of phase locked coherent vortices that will further produce acoustic emissions from their interaction with the shock cells.
3) The phase locked multiple interactions from the various shock cells with the coherent structures, will emit phase locked acoustic wave trains, these wave trains interact with the shear layer generating internal trapped waves with a cross-hatched pattern and synchronizes the opposite side of the shear layer to emit phase locked BBSAN interaction.
4) As the train of acoustic waves propagates into the upstream direction, the shear layer undergoes coherent modulation that amplifies the vortical structure growth as it passes through successive wave fronts. The increasing vortical structure size leads to an increase in mixing noise generation leading to strong wave emission towards the downstream direction.

These steps occur at all frequencies of the BBSAN noise components with various coherent vortical structure sizes that are frequency dependent. Since this mechanism is formulated for BBSAN, it can also be considered as an underlying generation mechanism for screech which is considered as a limiting case of BBSAN.

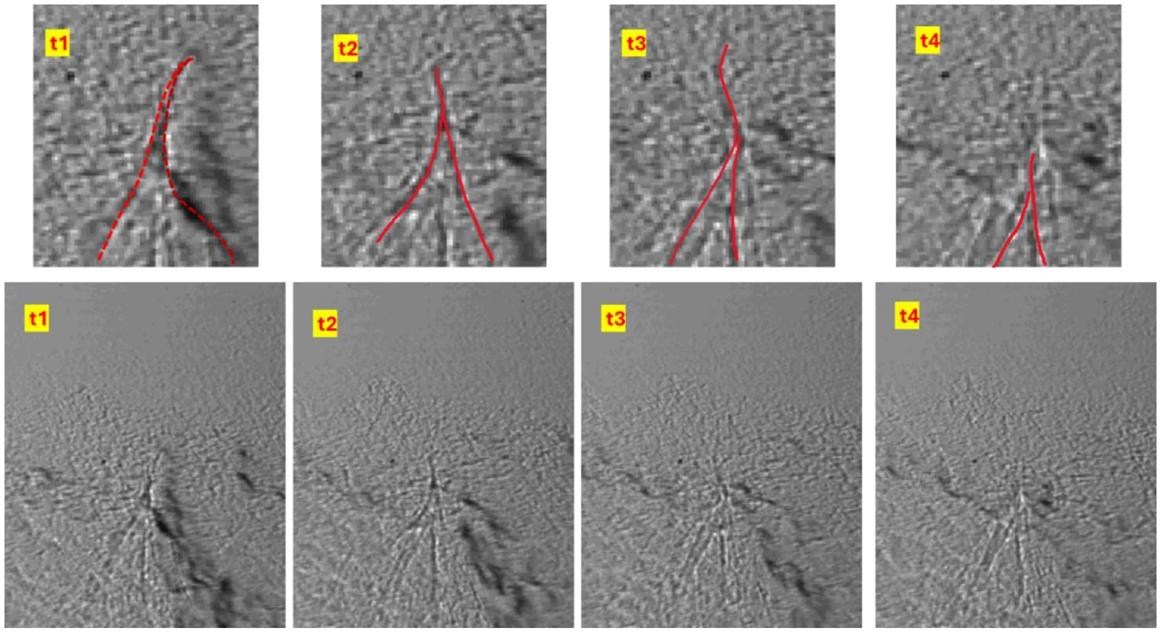

Figure 4.23: Snap shots of high-speed shadowgraph visualization showing the sequence of shock cell tip dynamics resulting from shear layer vortices interacting with the shock cell tip and its break-off to generate sound waves. The top row shows a close-up view of the bottom row. The results are for the baseline faceted nozzle at the non-screeching condition of NPR=2.7.

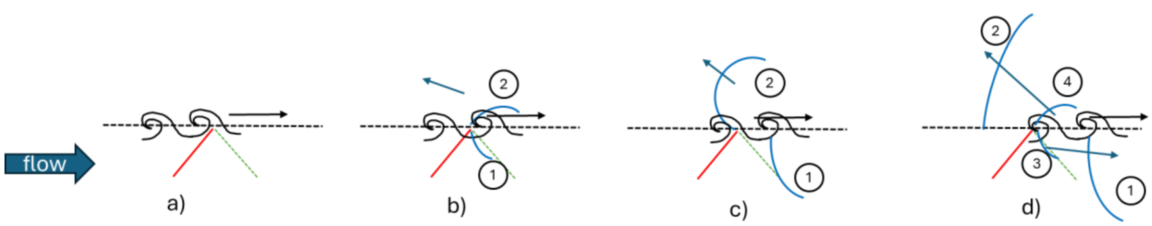

Figure 4.24: Schematic of the sequence of events for the shear layer vortices and shock cell tip interaction generating reflected shock waves and acoustic waves. The interaction dynamics show the generation process of acoustic noise emission resulting from shock vortex interaction at the shock cell tip. The interaction causes the generation of two reflected shocks R1 and R2.

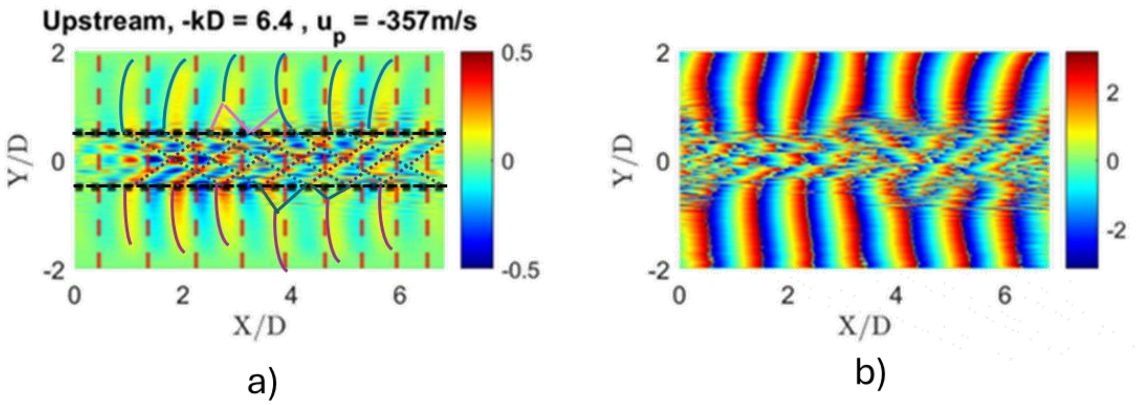

Figure 4.25: Sample BBSAN reconstruction of upstream acoustic wavenumber demonstrating the generation of internal wave propagation (cross-hatch pattern) due to external acoustic waves interacting with the shear layer. a) the real part of the complex plane showing normalized wave amplitudes, and b) the phase angle of the complex plane. The results are for the baseline nozzle at NPR=2.7 at a frequency representative of BBSAN. The black dotted lines indicate the nozzle lip line and the vertical dashed red lines indicate the shock cell locations. The waves are traced by curves and lines for visual aid.

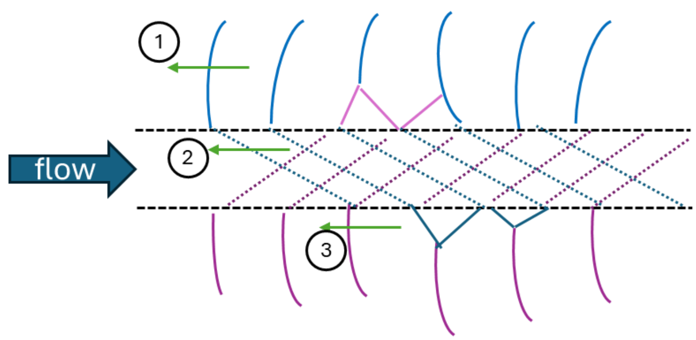

Figure 4.26: Schematic showing the traced lines of 1) the upstream external waves propagating in the upstream direction, 2) the induced oblique internal waves forming a cross-hatched pattern, and 3) the synchronization of the external acoustic waves on the opposite side of the shear layer being forced by the internal cross-hatched wave patterns. The schematic is a representation of BBSAN-generated internal and external waves propagating in the upstream direction for the baseline faceted nozzle at the non-screeching jet condition of NPR=2.7.

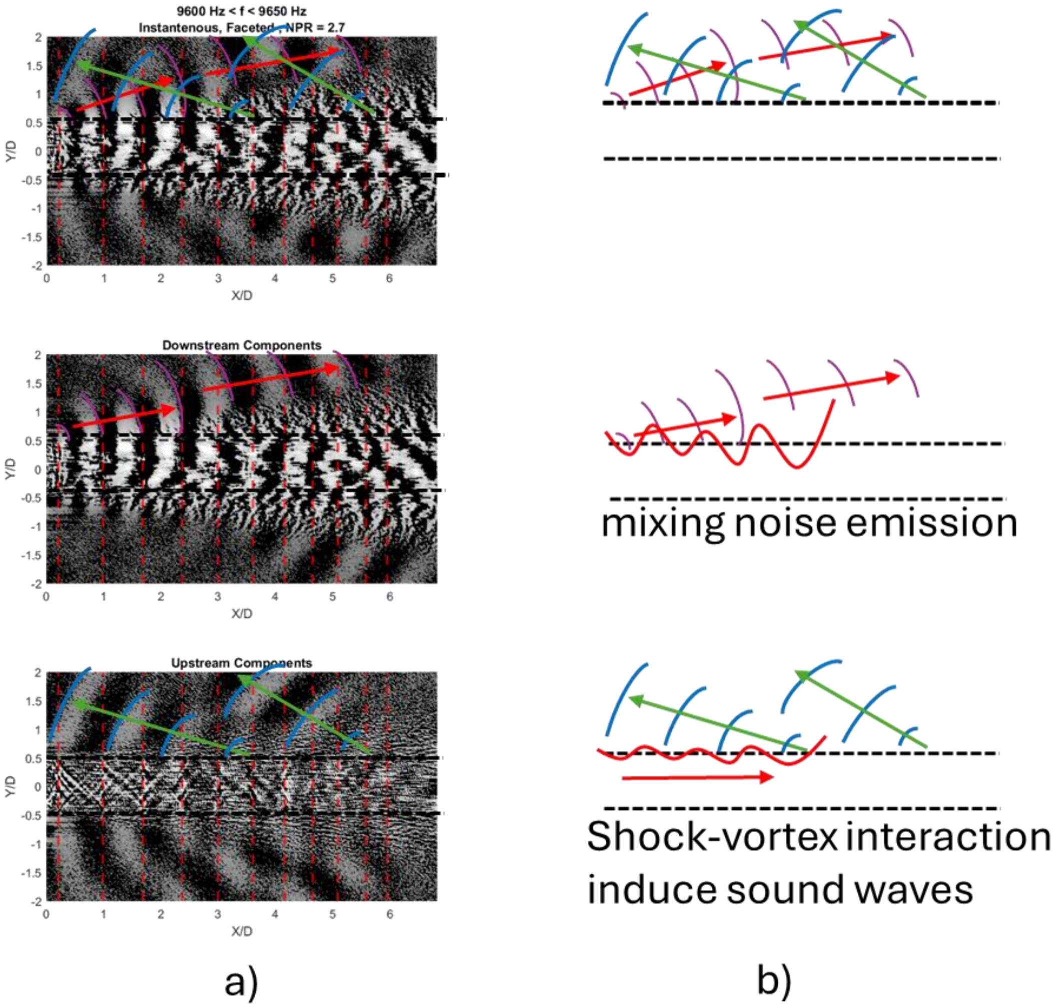

Figure 4.27: Fourier filtered flow field reconstruction at sample BBSAN frequency showing the fluctuating hydrodynamic and acoustic radiation field. The results show the combined upstream and downstream waves (top row), The downstream shear layer modulation and coherent turbulent structures with its associated downstream acoustic radiation beams (second row), and the upstream propagating internal waves and the upstream acoustic radiation beams and wave packets (third row). a) the flow field reconstruction overlaid with lines tracing the wave packets of acoustic wave radiation and the modulated shear layer coherence of turbulent structures, b) sketches of the overlaid radiation patterns. The arrows indicate different radiation acoustic beams. The results are for the baseline faceted nozzle, the nozzle operating condition is NPR=2.7.

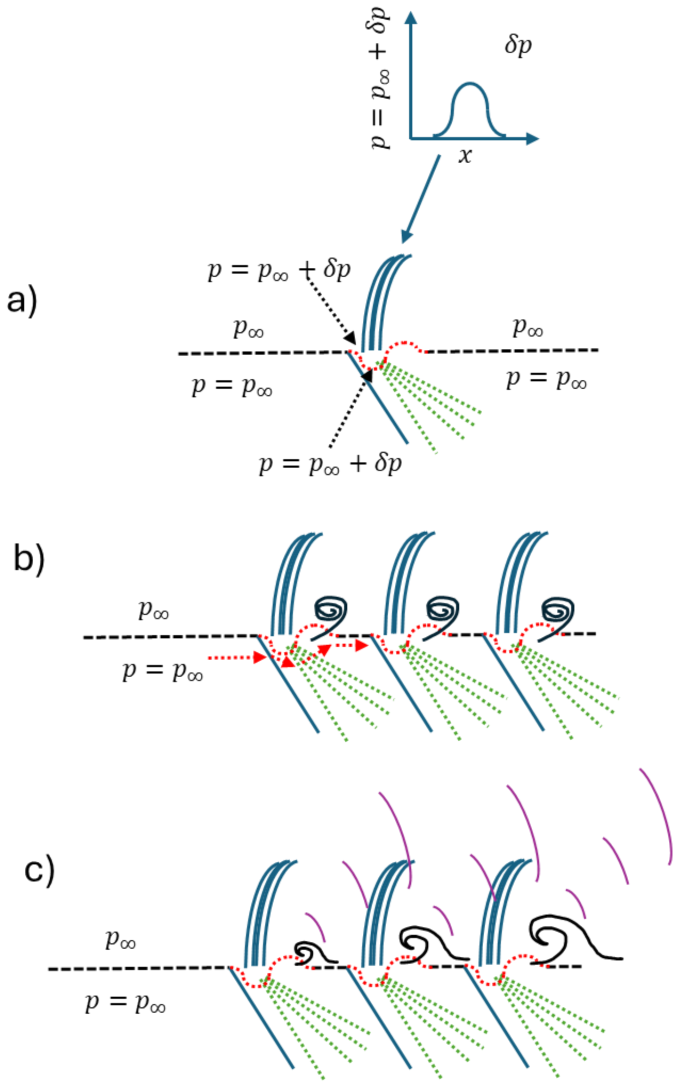

Figure 4.28: Schematic representation of shear layer modulation that causes the convecting turbulence coherence. a) shear layer at pressure equilibrium from outside ambient pressure and internal static pressure of the jet flow, the shear layer is perturbed by a passing acoustic pressure wave that influences the internal Mach waves and local flow turning, b) the passing of multiple acoustic waves successively perturbs the shear layer applying a forcing that drives the K-H instability and its coherence, c) the cumulative effects of forcing causes the instability to grow in the downstream direction and causes the emission of stronger downstream acoustic waves from the mixing noise component.

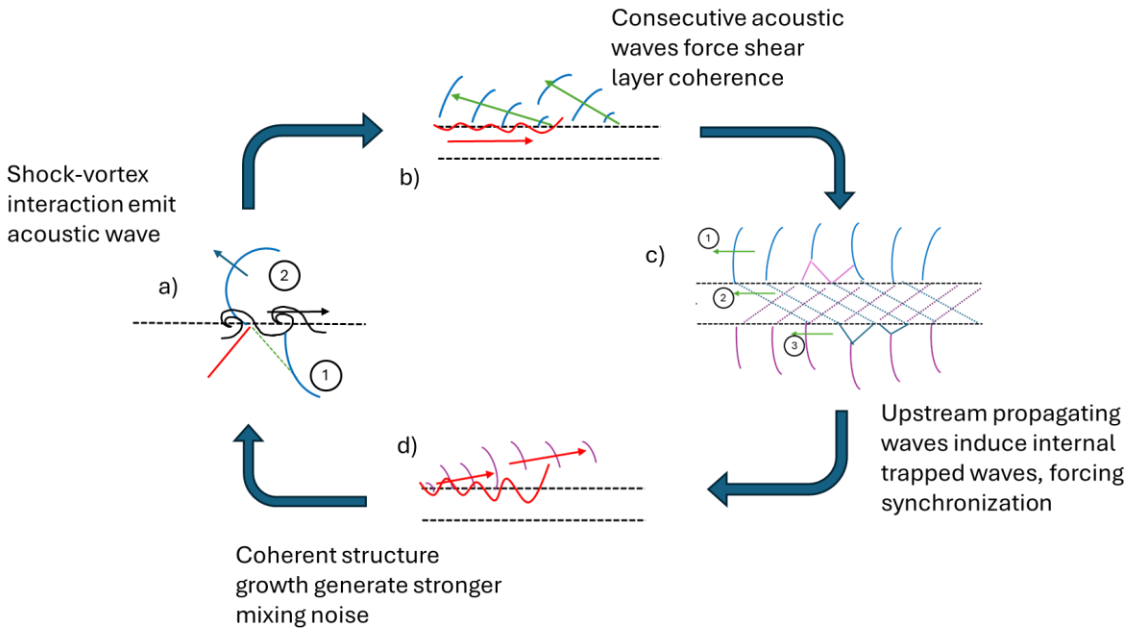

Figure 4.29: Proposed model for BBSAN noise generation and feedback loop. a) convecting shear layer vortices interact with shock cells generating reflected shocks and acoustic wave emission to the ambient, b) upstream propagating acoustic waves interact with the shear layer and force its coherent structures modulation, c) the external upstream propagating waves influence the shear layer and generates internal waves propagating in the upstream direction and synchronizes the opposite side of the shear layer, and d) the coherent structures caused by the shear layer modulation generates downstream acoustic radiation.

Chapter 5: Conclusions

MVG nozzles reduce the two dominant supersonic jet noise components of BBSN and turbulent mixing noise, leading to significant overall noise reduction with minimal thrust loss. The first part of this study explains the previous findings from microphone measurements and LES predictions by using new experimental flow and acoustic field data such as; surface oil flow visualizations, PIV, high-speed Schlieren imaging, and near-field acoustics. The experimental flow data is used to validate LES flow predictions of the MVG nozzles. The findings of the current study illustrate why MVG nozzles provide effective noise reduction outcomes. The thrust losses induced by single array MVG configurations are within 1.5% at the design or cruise condition. On the other hand, the double array induces higher thrust losses near 5% at the design condition. The thrust performance improvement is needed if the double-array configurations are to be used.

The noise reduction mechanisms of single and dual array Micro vortex generators implemented on scale model nozzles representative of GE-F404 nozzles have been investigated for NPRs relevant to takeoff conditions at the cold flow temperature. Experimental methods using surface oil flow visualization, PIV, high speed Schlieren imaging, far-field acoustics, and near-field acoustics have been utilized. The experimental results were compared to LES results and a good agreement was obtained. Scaling effects of MVG nozzles were performed on two model scales, a large nozzle with exit diameter of 3.166” and a small nozzle with exit diameter of 1.455” and the results show that MVG nozzle noise reduction performance is scalable for the tested model sizes.

Surface oil flow visualization revealed the intricate internal flow structures of the MVG nozzles and was complimented with internal LES flow fields to explain the internal mechanisms. It was found that the MVG blades interact with the flow and generated oblique shock waves that strengthened the external Mach disk near the nozzle exit and weakened the subsequent shock cells within the jet plume. Also, the oil flow showed the imprint of the formed counter-rotating streamwise vortices as they convect out of the nozzle along the shear layer and causes a delay to the nozzle lip separation point that reduces the size of the separated flow region.

PIV data quantified the flow velocity drop across the external Mach disk and the reductions in jet core velocities for the MVG configurations. MVGs increased the strength of the external Mach disk which caused a substantial velocity drop for the entire jet plume. The resulting lower jet core velocity weakened the shock cell structures and reduced the shock cell spacing. The double array nozzle showed further jet core velocity reductions and showed a subsonic jet centerline velocity at NPR=2.7. The transverse velocities showed that the streamwise counter-rotating vortices of the MVGs enhance ambient fluid entrainment into the shear layer. This entrainment interacted with the spanwise vorticity field within the shear layer causing a reduction in its intensity levels and causing a substantial increase in the shear layer spreading rate, also the increase in shear layer spread reduces its spanwise vorticity intensity due to a reduction in the velocity gradient across the shear layer between the jet core at its inner edge and the ambient fluid at its outer edge. The increased spreading rate of the shear layer in MVG nozzles causes a reduction and redistribution of the TKE intensity levels along the shear layer, showing that enhanced shear layer mixing is the underlying mechanism in its energy dissipation.

High-speed Schlieren visualization was used to estimate convective velocities along the nozzle lip-line, and it was found that MVG nozzles reduce the convective velocities of the turbulent structures within the shear layer when compared to the baseline nozzle.

The near-field acoustic measurements show that the enhanced shear layer mixing of the counter-rotating streamwise vortices generated by the MVG nozzles causes a substantial reduction to the low-frequency mixing noise sources which are due to reductions in shear layer TKE and convective velocity. Also, the reduced jet core velocity shows reduction and suppression of the screech noise sources. The reductions in the near-field noise sources cause the weakening of their acoustic radiation into the far-field. This is confirmed in the observations of the far-field acoustic measurements showing substantial noise reductions in the BBSN and mixing noise components for the MVG configurations. Additionally, the double array MVG showed the elimination of BBSN component at NPR=2.7.

The effectiveness of MVG nozzles in reducing the supersonic jet noise is due to two main mechanisms, the first is that MVGs generate streamwise counter-rotating vortices that induce higher levels of ambient entrainment causing reductions in the convective velocity of the shear layer and accelerate it dissipation. This reduces the shear layer turbulent kinetic energy and results in lower mixing noise generation. The second mechanism is that MVG blades generate internal oblique shocks that form a Mach disk near the nozzle exit. This Mach disk causes a reduction in the jet core velocity that produces an inverted velocity profile in the jet plume. This would increase the jet mixing and also reduce the shock-associated noise component. This first mechanism is also observed in applications of chevrons but not the second one.

In the second part of this study, a new analysis approach for experimental data that utilizes spectral analysis methods on the time resolved Schlieren visualizations was conducted to simultaneously study the spatio-temporal spectral contents of both the waves generated in the flow field of the supersonic jet and its acoustic wave emissions that generate the supersonic jet noise. This analysis approach was used to investigate the physical mechanisms of supersonic jet noise generation as well as its reduction mechanisms using MVGs as a jet noise reduction technology. In addition, this study culminated in the discovery of a new generation mechanism for BBSAN nose component, which is proposed in this study.

The jet's flow features were examined by transforming the flow field snapshots into the frequency-wavenumber domain. Where the jet's turbulent structures, internal waves and the external acoustic emissions in both upstream and downstream directions were characterized. It was found that MVGs cause the wavenumber of the propagating waves to shift to larger wavenumber values, this is due to an increase in shock cell spacing and a reduction in its strength leading to reductions in the jet core velocity. In addition, the streamwise counter rotating vortices produced by the MVGs cause the coherent structures traveling along the shear layer to breakdown to smaller scales and the mixing with the ambient fluid causes reductions in their convecting velocities.

Fourier filter was applied to the flow field to examine the frequency dependent flow features and its associated acoustic emissions. It was found that the wavelength of the coherent structures is an important factor in the type of noise emission produced. Where the large-scale mixing noise oscillating at low frequencies emitted downstream propagating acoustic waves. For higher frequencies, it was found that when the wavelengths of the convecting structures are equal or less than the wavelength values of the shock cell spacing, an upstream shock noise emission is produced due to the interaction of the convecting structures with the shock cell tips. This was observed in the radial distributions of the axial wavenumbers showing high intensity peak lobes approaching the wavenumber of the ambient speed of sound, which increases the noise emission efficiencies of these lobes and allow them to generate acoustic waves. The generated acoustic wave packets that are produced by the jet was visualized using a reconstruction of the sound field by suppressing wavenumber spectral content and only using the speed of sound wavenumber.

The mechanism for the onset of screech was identified, where a jet will undergo resonance and screech when the peak lobes related to the jet's preferred instability mode has a wavenumber equal to the ambient speed of sound wavenumber. And it was found that MVGs suppress screech by shifting this lobe to larger wavenumbers away from that for the ambient speed of sound.

In addition, MVGs cause reductions in the BBSAN noise component. This is because MVGs reduce the convection velocities and the scales of the turbulent structures which interact with the weakened shock cells both of which reduce the downstream and the upstream acoustic noise emissions of the BBSAN noise component.

Finally, the BBSAN directivity and noise generation mechanism was investigated. It was found that the change in BBSAN radiation direction as a function of peak frequency was due to a constructive and destructive interference patterns from the noise sources having a phased array behavior. In addition, it was found that the BBSAN sound generation mechanism is a result of shock-vortex interaction generating reflected waves which transitions into acoustic waves propagating outside the jet along the shear layer. And the interaction of these acoustic waves with the shear layer has two effects on the jet: first, it induces the modulation of the shear layer instability to form spatially coherent vortices through the collective interaction mechanism. And second, this interaction induces the formation of the jet's internal upstream propagating waves and the guided jet mode (GJM). Based on the experimental evidence presented in this study, a new BBSAN noise generation mechanism and it directivity mechanism are proposed.

Chapter 6: Future work

The research contributions provided in this dissertation are a physical understanding of the influence of hydrodynamic and acoustic wavenumber spectra on jet noise generation. Effective jet noise reduction is achieved by modifying the wavenumber spectra by inducing a shift in peak wavenumber values that produces acoustic emissions to wavenumber values that reduce the acoustic emission efficiency. The analytical methodology was successfully applied to MVG nozzles to directly analyze the flow modification influence on the emitting noise sources. In addition, new noise generation mechanisms were discovered and proposed. Future work is recommended to provide additional measurements and simulations to substantiate the proposed noise generation mechanisms and include:

- Conducting experiments on larger nozzles to provide higher spatial resolution of the flow field for time-resolved Schlieren visualizations.
- Conducting experiments using low turbulence nozzles by using a fifth-order polynomial from the plenum to the nozzle, the cleaner flow with low turbulence will permit high detail investigations on the internal wave structures in the flow which is substantially obscured by the highly turbulent jet.
- Implementing high-speed time-resolved PIV measurements and applying spectral analysis techniques to investigate the shock-vortex dynamics.
- Implementing Tomographic-PIV to obtain 3D-volumetric measurements to investigate azimuthal instabilities in the velocity field of the jet.

- Implementing simultaneous PIV and Schlieren visualization to correlate velocity fluctuation with emitted acoustic waves to investigate acoustic sources.
- Conduct numerical simulations on the entire jet flow to confirm the noise generation mechanisms proposed in this dissertation.
- Conduct higher resolution numerical simulations of model problems using a mixing layer and a single shock cell to isolate the relevant noise generation mechanisms and wavenumber spectral content and its acoustic emissions.

References

1 Veterans Administration, "Annual Benefits Report - Veterans Benefits Administration Reports," *Annual Benefits Report*, 2015.

2 Ahuja, K., "Supersonic jet noise reduction by tabs and ejectors," 1993.

3 Callender, B., Gutmark, E. J., and Martens, S., "Far-Field Acoustic Investigation into Chevron Nozzle Mechanisms and Trends," *AIAA Journal*, vol. 43, 2005, pp. 87–95.

4 Henderson, B., and Bridges, J., "An MDOE investigation of chevrons for supersonic jet noise reduction," *16th AIAA/CEAS Aeroacoustics Conference (31st AIAA Aeroacoustics Conference)*, 2010, pp. 1–18.

5 Bridges, J., Wernet, M. P., and Frate, F. C., "PIV measurements of chevrons on f400-series tactical aircraft nozzle model," *49th AIAA Aerospace Sciences Meeting Including the New Horizons Forum and Aerospace Exposition*, 2011, pp. 1–15.

6 Bridges, J., and Brown, C., "Parametric Testing of Chevrons on Single Flow Hot Jets," *10th AIAA/CEAS Aeroacoustics Conference*.

7 Henderson, B., and Bridges, J., "An MDOE investigation of chevrons for supersonic jet noise reduction," *16th AIAA/CEAS Aeroacoustics Conference (31st AIAA Aeroacoustics Conference)*, 2010, pp. 1–18.

8 Liu, J., Khine, Y. Y., Saleem, M., Rodriguez, O. L., and Gutmark, E., "Comparison of the Thrust-Based Noise Reduction Performance between Micro-Vortex Generators and Chevrons," *28th AIAA/CEAS Aeroacoustics Conference, 2022*, 2022, pp. 1–32.

9 Liu, J., Khine, Y. Y., Saleem, M., Lopez Rodriguez, O., and Gutmark, E., "Supersonic Jet Noise Reduction Using Micro Vortex Generators," 2021, pp. 1–24.

10 Saleem, M., Rodriguez, O. L., Gutmark, E., and Liu, J., "Enhanced Supersonic Jet Noise Reduction using Two Array Configurations of Micro Vortex Generators," *AIAA Science and Technology Forum and Exposition, AIAA SciTech Forum 2022*, 2022, pp. 1–12.

11 Brown, G. L., and Roshko, A., "On density effects and large structure in turbulent mixing layers," *Journal of Fluid Mechanics*, vol. 64, 1974, pp. 775–816.

12 Winant, C. D., and Browand, F. K., "Vortex pairing : The mechanism of turbulent mixing-layer growth at moderate Reynolds number," *Journal of Fluid Mechanics*, vol. 63, 1974, pp. 237–255.

13 Papamoschou, D., "Structure of the compressible turbulent shear layer," *AIAA Journal*, vol. 29, 1991, pp. 680–681.

14 In, M. E., and Shear, S. F., "MIXING ENHANCEMENT IN," 1995, pp. 375–417.

15 Thurow, B., Samimy, M., and Lempert, W., "Compressibility effects on turbulence structures of axisymmetric mixing layers," *Physics of Fluids*, vol. 15, 2003, pp. 1755–1765.

16 Tam, C. K. W., "Supersonic jet noise," *Annual Review of Fluid Mechanics*, vol. 27, 1995, pp. 17–43.

[17] Norum, T. D., and Seiner, J. M., "Broadband shock noise from supersonic jets," *AIAA Journal*, vol. 20, 1982, pp. 68–73.

[18] Pao, S. P., and Seiner, J. M., "Shock-associated noise in supersonic jets," *AIAA Journal*, vol. 21, 1983, pp. 687–693.

[19] Powell, A., "On the mechanism of choked jet noise," *Proceedings of the Physical Society. Section B*, vol. 66, 1953, pp. 1039–1056.

[20] Edgington-Mitchell, D., "Aeroacoustic resonance and self-excitation in screeching and impinging supersonic jets – A review," *International Journal of Aeroacoustics*, vol. 18, 2019, pp. 118–188.

[21] Tarn, C. K. W., Golebiowski, M., and Seiner, J. M., "On the two components of turbulent mixing noise from supersonic jets," *2nd AIAA/CEAS Aeroacoustics Conference*, 1996.

[22] Seiner, J. M., Ponton, M. K., Jansen, B. J., and Lagen, N. T., "The effects of temperature on supersonic jet noise emission," *92-02-046*, 1992, pp. 295–307.

[23] Oertel Sen, H., Seiler, F., Srulijes, J., and Hruschka, R., "Mach waves produced in the supersonic jet mixing layer by shock/vortex interaction," *Shock Waves*, vol. 26, 2016, pp. 231–240.

[24] Tam, C. K. W., and Hu, F. Q., *On the three families of instability waves of high-speed jets*, 1989.

[25] Yu, K., Gutmark, E., and Schadow, K. C., "On Coherent Vortex Formation in Axisymmetric Compressible Shear Layers BT - Turbulent Shear Flows 9," F. Durst, N. Kasagi, B.E. Launder, F.W. Schmidt, K. Suzuki, and J.H. Whitelaw, eds., Berlin, Heidelberg: Springer Berlin Heidelberg, 1995, pp. 207–218.

[26] Jordan, P., and Colonius, T., "Wave packets and turbulent jet noise," *Annual Review of Fluid Mechanics*, vol. 45, 2013, pp. 173–195.

[27] Taira, K., Brunton, S. L., Dawson, S. T. M., Rowley, C. W., Colonius, T., McKeon, B. J., Schmidt, O. T., Gordeyev, S., Theofilis, V., and Ukeiley, L. S., "Modal analysis of fluid flows: An overview," *AIAA Journal*, vol. 55, 2017, pp. 4013–4041.

[28] Schmidt, O. T., Towne, A., Colonius, T., Cavalieri, A. V. G., Jordan, P., and Brès, G. A., "Wavepackets and trapped acoustic modes in a turbulent jet: Coherent structure eduction and global stability," *Journal of Fluid Mechanics*, vol. 825, 2017, pp. 1153–1181.

[29] Schmidt, O. T., Towne, A., Rigas, G., Colonius, T., and Brès, G. A., "Spectral analysis of jet turbulence," *Journal of Fluid Mechanics*, vol. 855, 2018, pp. 953–982.

[30] Tam, C. K. W., "Mach wave radiation from high-speed jets," *AIAA Journal*, vol. 47, 2009, pp. 2440–2448.

[31] Bogey, C., Marsden, O., and Bailly, C., "A computational study of the effects of nozzle-exit turbulence level on the flow and acoustic fields of a subsonic jet," *17th AIAA/CEAS Aeroacoustics Conference 2011 (32nd AIAA Aeroacoustics Conference)*, 2011, pp. 5–8.

[32] Colonius, T., and Lele, S. K., "Computational aeroacoustics: Progress on nonlinear

problems of sound generation," *Progress in Aerospace Sciences*, vol. 40, 2004, pp. 345–416.

33 Zhang, Z., and Wu, X., "Nonlinear evolution and acoustic radiation of coherent structures in subsonic turbulent free shear layers," *Journal of Fluid Mechanics*, vol. 884, 2019.

34 Cavalieri, A. V. G., Rodríguez, D., Jordan, P., Colonius, T., and Gervais, Y., "Wavepackets in the velocity field of turbulent jets," *Journal of Fluid Mechanics*, vol. 730, 2013, pp. 559–592.

35 Ho, C. M., "Dynamics of an impinging jet. part 1. the feedback phenomenon," *Journal of Fluid Mechanics*, vol. 105, 1981, pp. 119–142.

36 Burton, D. A. L. E. E., "Two-dimensional mixing layers," vol. 138, 1984.

37 Tam, C. K. W., and Burton, D. E., "Sound generated by instability waves of supersonic flows. Part 2. Axisymmetric jets," *Journal of Fluid Mechanics*, vol. 138, 1984, pp. 273–295.

38 Tam, C. K. W., Seiner, J. M., and Yu, J. C., "Proposed relationship between broadband shock associated noise and screech tones," *Journal of Sound and Vibration*, vol. 110, 1986, pp. 309–321.

39 Tam, C. K. W., Seiner, J. M., and Yu, J. C., "on the Relationship Between Broadband Shock Associated Noise and Screech Tones.," *AIAA Paper*, 1984.

40 Tam, C. K. W., and Tanna, H. K., "Shock associated noise of supersonic jets from convergent-divergent nozzles," *Journal of Sound and Vibration*, vol. 81, 1982, pp. 337–358.

41 Fisher, M. J., Lush, P. A., and Harper Bourne, M., "Jet noise," *Journal of Sound and Vibration*, vol. 28, 1973, pp. 563–585.

42 Panda, J., Raman, G., and Zaman, K. B. M. Q., "Underexpanded screeching jets from circular, rectangular and elliptic nozzles," *3rd AIAA/CEAS Aeroacoustics Conference*, 1997, pp. 275–285.

43 Panda, J., "An experimental investigation of screech noise generation," *2nd AIAA/CEAS Aeroacoustics Conference*, vol. 378, 1996, pp. 71–96.

44 Panda, J., and Seasholtz, R. G., "Measurement of shock structure and shock-vortex interaction in underexpanded jets using Rayleigh scattering," *Physics of Fluids*, vol. 11, 1999, pp. 3761–3777.

45 Karami, S., Edgington-Mitchell, D., Theofilis, V., and Soria, J., "Characteristics of acoustic and hydrodynamic waves in under-expanded supersonic impinging jets," *Journal of Fluid Mechanics*, 2020.

46 Edgington-Mitchell, D., Weightman, J., Lock, S., Kirby, R., Nair, V., Soria, J., and Honnery, D., "The generation of screech tones by shock leakage," *Journal of Fluid Mechanics*, 2020.

47 Li, X., Wu, X., Liu, L., Zhang, X., Hao, P., and He, F., "Acoustic resonance mechanism for axisymmetric screech modes of underexpanded jets impinging on an inclined plate," *Journal of Fluid Mechanics*, vol. 956, 2023, pp. 1–28.

48 Liang, L. L., Wan, Z. H., Ye, C. C., Zhang, P. J. Y., Sun, D. J., and Lu, X. Y., "Flow dynamics and noise generation mechanisms in supersonic underexpanded

rectangular and planar jets," *AIP Advances*, vol. 13, 2023.
49 Edgington-Mitchell, D., Wang, T., Nogueira, P., Schmidt, O., Jaunet, V., Duke, D., Jordan, P., and Towne, A., "Waves in screeching jets," *arXiv*, 2020.
50 Suzuki, T., and Lele, S. K., "Shock leakage through an unsteady vortex-laden mixing layer: application to jet screech," *Journal of Fluid Mechanics*, vol. 490, Sep. 2003, pp. 139–167.
51 Edgington-Mitchell, D. M., Weightman, J. L., Soria, J., and Honnery, D. R., "Sound production by shock leakage in supersonic jet screech," *2018 AIAA/CEAS Aeroacoustics Conference*, 2018.
52 Semlitsch, B., Semlitsch, B., Malla, B., Gutmark, E. J., and Mihăescu, M., "The generation mechanism of higher screech tone harmonics in supersonic jets," *Journal of Fluid Mechanics*, vol. 893, 2020.
53 Oertel, H., "Mach wave radiation of hot supersonic jets investigated by means of a shock tube and new optical techniques," *Proceedings of the 12th International Symposium on Shock-Tubes and Waves, Israel*, 1980.
54 Oertel, H., Seiler, F., and Srulijes, J., "30th International Symposium on Shock Waves 1," *30th International Symposium on Shock Waves 1*, 2017, pp. 4–9.
55 Oertel Sen, H., Seiler, F., and Srulijes, J., "Vortex Induced Mach Waves in Supersonic Jets," *28th International Symposium on Shock Waves*, 2012, pp. 657–663.
56 Zaman, K. B. M. Q., Fagan, A. F., and Upadhyay, P., "Pressure fluctuations due to 'trapped waves' in the initial region of compressible jets," *Journal of Fluid Mechanics*, vol. 931, 2022, pp. 1–24.
57 Manning, T. A., and Lele, S. K., "Numerical simulations of shock-vortex interactions in supersonic jet screech," *36th AIAA Aerospace Sciences Meeting and Exhibit*, 1998.
58 Lele, S. K., "Phased array models of shock-cell noise sources," *Collection of Technical Papers - 11th AIAA/CEAS Aeroacoustics Conference*, vol. 1, 2005, pp. 536–555.
59 Wong, M. H., Jordan, P., Honnery, D. R., and Edgington-Mitchell, D., "Impact of coherence decay on wavepacket models for broadband shock-associated noise in supersonic jets," *Journal of Fluid Mechanics*, vol. 863, 2019, pp. 969–993.
60 Norum, T. D., "Screech suppression in supersonic jets," *AIAA Journal*, vol. 21, 1983, pp. 235–240.
61 Norum, T. D., and Seiner, J. M., "Broadband shock noise from supersonic jets," *AIAA Journal*, vol. 20, 1982, pp. 68–73.
62 Lui, C., and Lele, S. K., "A numerical investigation of broad-band shock noise," *40th AIAA Aerospace Sciences Meeting and Exhibit*, 2002.
63 Schaupp, C., Sesterhenn, J., and Friedrich, R., "On a method for direct numerical simulation of shear layer/compression wave interaction for aeroacoustic investigations," *Computers and Fluids*, vol. 37, 2008, pp. 463–474.
64 Shi, F., Gao, Z., Jiang, C., and Lee, C. H., "Numerical investigation of shock-turbulent mixing layer interaction and shock-associated noise," *Physics of Fluids*,

vol. 33, 2021.
65 Ren, Z., Wang, B., and Zheng, L., "Numerical analysis on interactions of vortex, shock wave, and exothermal reaction in a supersonic planar shear layer laden with droplets," *Physics of Fluids*, vol. 30, 2018.
66 Dcsanjh, D. S., and Weeks, T. M., "Interaction of a starting vortex as well as a vortex street with a traveling shock wave," *AIAA Journal*, vol. 3, 1965, pp. 216–223.
67 INOUE O., H. Y., "Sound generation by shock-vortex interaction," *Journal of Fluid Mechanics*, vol. 5, 1967, pp. 660–669.
68 Ribner, H. S., "Cylindrical sound wave generated by shock-vortex interaction," *AIAA Journal*, vol. 23, 1985, pp. 1708–1715.
69 New, T. H., Long, J., Zang, B., and Shi, S., "Collision of vortex rings upon V-walls," *Journal of Fluid Mechanics*, 2020.
70 Chatterjee, A., and Vijayaraj, S., "Multiple sound generation in interaction of shock wave with strong vortex," *AIAA Journal*, vol. 46, 2008, pp. 2558–2567.
71 Aravindh Kumar, S. M., and Rathakrishnan, E., "Elliptic jet control with triangular tab," *Proceedings of the Institution of Mechanical Engineers, Part G: Journal of Aerospace Engineering*, vol. 231, 2017, pp. 1460–1477.
72 Tinney, C. E., Valdez, J., and Murray, N., "Aerodynamic performance of augmented supersonic nozzles," *Experiments in Fluids*, vol. 61, 2020, pp. 1–15.
73 Gutmark, E. J., Callender, W., and Martens, S., "Aeroacoustics of turbulent jets: Flow structure noise sources, and control," *JSME International Journal, Series B: Fluids and Thermal Engineering*, vol. 49, 2007, pp. 1078–1085.
74 Alkislar, M. B., Krothapalli, A., and Butler, G. W., *The effect of streamwise vortices on the aeroacoustics of a Mach 0.9 jet*, 2007.
75 Munday, D., Gutmark, E., Liu, J., and Kailasanath, K., "Flow structure and acoustics of supersonic jets from conical convergent-divergent nozzles," *Physics of Fluids*, vol. 23, 2011.
76 Henderson, B. S., "Fifty years of fluidic injection," *Aeroacoustics*, vol. 9, 2010, pp. 91–122.
77 Powers, R. W., McLaughlin, D. K., and Morris, P. J., "Noise reduction in supersonic jets from rectangular convergent-divergent nozzles," *53rd AIAA Aerospace Sciences Meeting*, 2015.
78 Cuppoletti, D., Gutmark, E., Hafsteinsson, H., and Eriksson, L. E., "Elimination of shock associated noise in supersonic jets by destructive wave interference," *AIAA Aerospace Sciences Meeting, 2018*, vol. 0, 2018.
79 Martens, S., and Spyropoulos, J. T., "Practical jet noise reduction for tactical aircraft," *Proceedings of the ASME Turbo Expo*, vol. 1, 2010, pp. 389–399.
80 Godard, G., and Stanislas, M., "Control of a decelerating boundary layer. Part 1: Optimization of passive vortex generators," *Aerospace Science and Technology*, vol. 10, 2006, pp. 181–191.
81 Velte, C. M., Hansen, M. O. L., and Okulov, V. L., "Multiple vortex structures in the wake of a rectangular winglet in ground effect," *Experimental Thermal and*

Fluid Science, vol. 72, 2016, pp. 31–39.
82 Panaras, A. G., and Lu, F. K., "Progress in Aerospace Sciences Micro-vortex generators for shock wave / boundary layer interactions," *Progress in Aerospace Sciences*, vol. 74, 2015, pp. 16–47.
83 Li, Q., Yan, Y., Wang, X., and Liu, C., "The Interaction between Vortex Rings and Oblique Shocks by the MVG Controlled Ramp Flow at M=2.5," 2011, pp. 1–20.
84 Lopez Rodriguez, O., Saleem, M., Gutmark, E. J., and Liu, J., "Study of temperature effect on flow and acoustic behavior of supersonic jet emanating from a faceted nozzle," 2021, pp. 3–15.
85 Liu, J., Khine, Y. Y., Saleem, M., Rodriguez, O. L., and Gutmark, E., "Effect of Axial Location of Micro Vortex Generators on Supersonic Jet Noise Reduction," *AIAA Science and Technology Forum and Exposition, AIAA SciTech Forum 2022*, 2022, pp. 1–24.
86 Hileman, J. I., Thurow, B. S., Caraballo, E. J., and Samimy, M., "Large-scale structure evolution and sound emission in high-speed jets: Real-time visualization with simultaneous acoustic measurements," *Journal of Fluid Mechanics*, vol. 544, 2005, pp. 277–307.
87 Tam, C. K. W., Viswanathan, K., Ahuja, K. K., and Panda, J., "The sources of jet noise: Experimental evidence," *Journal of Fluid Mechanics*, vol. 615, 2008, pp. 253–292.
88 Gojon, R., Bogey, C., and Marsden, O., "Investigation of tone generation in ideally expanded supersonic planar impinging jets using large-eddy simulation," 2016, pp. 90–115.
89 Bogey, C., and Gojon, R., "Feedback loop and upwind-propagating waves in ideally expanded supersonic impinging round jets," *Journal of Fluid Mechanics*, vol. 823, 2017, pp. 562–591.
90 Karnam, A., Saleem, M., and Gutmark, E., "Influence of nozzle geometry on screech instability closure," *Physics of Fluids*, vol. 35, 2023.
91 Callender, B., Gutmark, E., and Dimicco, R., "The design and validation of a coaxial nozzle acoustic test facility," *40th AIAA Aerospace Sciences Meeting & Exhibit*, 2002.
92 Samimy, M., and Lele, S. K., "Motion of particles with inertia in a compressible free shear layer," *Physics of Fluids A*, vol. 3, 1991, pp. 1915–1923.
93 Tavoularis, S., "Measurement in Fluid Mechanics by Stavros Tavoularis," 2005.
94 Settles, G. S., *Schlieren und shadowgraph techniques: visualizing phenomena in transparent media - Experimental Fluid Mechanics*, 2001.
95 Zuckerwar, A. J. , Bass, H., "Atmospheric absorption of sound: Update," *Journal of the Acoustical Society of America*, vol. 88, 1990, pp. 2019–2021.
96 Bass, et. al, "Atmospheric Absorption of Sound- Further Developments," 2016, p. 41.
97 Liu, J., Corrigan, A., and Kailasanath, K., "Equilibrium Wall Model Implementation in a Nodal Finite Element Flow Solver {JENRE} for Large Eddy Simulations," *NRL Memo Report, NRL/MR/6040-17-9760.*, 2017.

98 Liu, J., Corrigan, A. T., and Ramamurti, R., "Large-eddy simulations of supersonic jet noise generation using wall modeling," *2018 AIAA/CEAS Aeroacoustics Conference*, 2018, pp. 1–20.

99 Liu, J., and Khine, Y. Y., "Nozzle Boundary-Layer Separation Near the Nozzle Exit in Highly Overexpanded Jets," 2020, pp. 1–23.

100 Saleem, M., Lopez Rodriguez, O., Liu, J., Khine, Y., and Gutmark, E., "Acoustics of Over Expanded and Fully Expanded Supersonic Jets from Circular and Faceted Nozzles," 2021, pp. 1–13.

101 ENNIX, K., BURCHAM, JR., F., and WEBB, L., "Flight-determined engine exhaust characteristics of an F404 engine in an F-18 airplane," 1993.

102 Tanna, H. K., Tester, B. J., and Lau, J. C., "The Noise and Flow Characteristics . NASA CR-158 995," 1979.

103 Tanna, H. K., "Coannular jets—Are they really quiet and why?," *Journal of Sound and Vibration*, vol. 72, 1980, pp. 97–118.

104 Viswanathan, K., "Does a model-scale nozzle emit the same jet noise as a jet engine?," *AIAA Journal*, vol. 46, 2008, pp. 336–355.

105 Saleem, M., Karnam, A., Rodriguez, O., Liu, J., and Gutmark, E., "Flow and acoustic fields investigation of noise reduction by micro vortex generators in supersonic nozzles," *Physics of Fluids*, vol. 35, 2023.

Appendix

```
%% DESCRIPTION: Code computes wavenumber spectra from Schlieren data
% % % close all
% % % clc;   clearvars;   set(0,'defaultfigurecolor',[1 1 1])
% driveIn ='D:\SyncSchlierenZ\saved\';
% driveIn ='E:\SyncSchlierenZ\saved\';
%
% driveIn ='C:\Documents\Schlieren practice\saved\'
% driveOut = driveIn + "plots Fourrier";
% set(0,'DefaultAxesFontName', 'Times New Roman');
set(0,'defaultfigurecolor','w');
set(0,'DefaultAxesFontSize', 20);
set(0,'defaultlinelinewidth',2);
set(0,'DefaultLineMarkerSize', 10);
% set(0,'defaultAxesFontWeight','bold');
%% Loading nozzle data
close all
driveIn = ["C:\TMX Schlieren"]


%  Loading nozzle data
tests = ["NPR2p7" , "NPR3p0" , "NPR3p5"];   nozType = ["Faceted" , "MVGb36" ,
"2ArrayT", "Faceted_Dropped"]; %nozType = ["Faceted" , "MVGa90b36" ,
"2ArrayT"];
fAcq = 204800 % 78000
g=1.4
T0=300 %( PIV heated to about 50 C )
Rgas=286
NPRg=(g-1)/g
g_12=(g-1)/2





% St=ffi*(De_small/u_j)


%% Saved variables name and location



folderName='Wavenumber Cropped no fluc large font'
folderNameSave=[driveInSchlSave + "\" + folderName]
```

```
LoadName=([num2str(driveInSchlSave),num2str("\")  ,
num2str("TMXSchlieren.mat")]) % construct save name
load(LoadName)

% tests = ["NPR2p7" , "NPR3p0" , "NPR3p5"];   nozType = ["Faceted" , "MVGb36"
, "2ArrayT"]; %nozType = ["Faceted" , "MVGa90b36" , "2ArrayT"];
%
% nprSelect=1
% nozSelect=1
%%
save_switch=1
acoustic_speed_switch=1

frqPlotIn=6000                                % <<------------------------------
input frequency value for analysis ------------------------------ <<


condition = tests(nprSelect);   config = nozType(nozSelect);



% condition = tests(2);   config = nozType(1);
De=36.5133 % Diameter in [mm] seal to seal height

%  Image Acquisition
% fAcq = 78000;
dt = 1/fAcq;

%------------

N_t=size(imgMatrix,3) %23000 %5000%1000%40000%1000
% dt=1/204800 %145690%110000%1/15000

% fftwindow=ones(1,256)
fftwindow=1024*4 %1024*4%2%400%2*1024%300
 nOvlp = 0.5%0.75;

N_blk=(N_t-(fftwindow*nOvlp))/(fftwindow-(fftwindow*nOvlp))
% nSamples = 1*1024;   nOvlp = 0.5;   N_blks = (imgNos -
(nSamples*nOvlp))/(nSamples-(nSamples*nOvlp));


Df=(1/dt)/fftwindow

%-----------------------

% load(driveIn + "KE 205kHz 1us 105mm " + config + " " + condition );
%  Image dimensions
% % % imgMeanB=imgMean-Background;
% % % I=size(imgMatrix,1); J=size(imgMatrix,2);
% % % rowNo = I;   colNo = J;
```

```
imgNos = size(imgMatrix,3);

%load data and define X,Y
% % % X=I; Y=J;

nozzleName=["Faceted" "MVG" "2 Array T"];
nozzle=nozzleName(nozSelect)
nprRange=[2.7 3.0 3.5]
npr=nprRange(nprSelect)

M_j=((2/(g-1))*(npr^(NPRg)-1))^0.5
T_j=T0/(1+g_12*M_j^2 )
u_j=M_j*(g*Rgas*T_j)^0.5

% %  Image & axes reshape
% imgMatrix = reshape(M_I,[rowNo,colNo,imgNos]);
% imgMatrix = rot90(imgMatrix);   imgMatrix   = fliplr(imgMatrix);
% % X = reshape(M_x,rowNo,colNo);   Y = reshape(M_y,rowNo,colNo);
% X = X(:,1)';   Y = flipud(Y(1,:)');   clear M_I M_x M_y;
figure; pcolor(imgMatrix(:,:,1));  shading interp; axis equal
%  Nozzle Lip
% xStrt = 9;   X = X - X(xStrt);   %Y = Y - Y(1);   Y = Y - Y(1);
%  Mean Schlieren

%  X zero location & start point away from nozzle exit(xShift)
% xZero = find(X > 0);   xZero = xZero(1);   xShift = 3 + xZero;
%  Limits for 400k image case




% dx=8*25.4/(488-58)
% x=(0:size(imgMatrix,2)-1)*dx-4.72558
% y=(0:size(imgMatrix,1)-1)*dx-39.6949-De/2
% zero location x=43, y=373
%----------------------------------------------
% dx=9*25.4/(740-83)
% x=(0:size(imgMatrix,2)-1)*dx %-4.72558
% y=(0:size(imgMatrix,1)-1)*dx %-39.6949-De/2
% x=x-x(43);
% y=y-y(373) ;
%
%
De2=dx/De;
%
%
% axial_De=x/De;
% radial_De=y/De;
%-------------------------------------------------
```

```
xLim = [axial_De(1) axial_De(end)];   yLim = [radial_De(1) radial_De(end)];
xlim(xLim);   ylim(yLim);

meanSch = mean(imgMatrix,3);
meanSTD = std(imgMatrix,0,3);
meanSTD2=log10(meanSTD);
imgAvg = mean(imgMatrix,3);

imgMatrix=imgMatrix-imgAvg(50,120);


fig1 = figure;   set(fig1,"Position",[3.1943e+03 143.6667 412 368])%[2029 148
912 368])
pcolor(axial_De,radial_De,meanSch);   shading interp;   colormap gray;
axis equal;   xlim(xLim);   ylim(yLim);      box off;
ax = gca;   ax.FontSize = 12;   xlabel('X/D','Interpreter','latex');
ylabel('Y/D','Interpreter','latex');
title(["Mean, " + nozzle + " , NPR = " + npr],'Interpreter','latex')
xline(axial_De(locLs),'--r','linewidth',2)
    yline([-0.5 0.5],'--k','linewidth',2)


fig1 = figure;   set(fig1,"Position", [3.1943e+03 331.6667 412
180.0000])%[2029 148 912 368])
pcolor(axial_De,radial_De,meanSch);   shading interp;   colormap gray;
axis equal;   xlim(xLim);   ylim([0 yLim(2)]);      box off;
ax = gca;   ax.FontSize = 12;   xlabel('X/D','Interpreter','latex');
ylabel('Y/D','Interpreter','latex');
title(["Mean, " + nozzle + " , NPR = " + npr],'Interpreter','latex')
xline(axial_De(locLs),'--r','linewidth',2)
    yline([-0.5 0.5],'--k','linewidth',2)

figName=([driveOut + nozzle + "_NPR=" + npr + ", Mean flow2" ] )
saveas(fig1,[figName + ".tiff"])

fig1 = figure;   set(fig1,"Position",[3.1943e+03 143.6667 412 368])%[2029 148
912 368])
pcolor(axial_De,radial_De,meanSch);   shading interp;   colormap gray;
axis equal;   xlim(xLim);   ylim(yLim);      box off;
ax = gca;   ax.FontSize = 12;   xlabel('X/D','Interpreter','latex');
ylabel('Y/D','Interpreter','latex');
title(["Mean, " + nozzle + " , NPR = " + npr],'Interpreter','latex')


figName=([driveOut + nozzle + "_NPR=" + npr + ", Mean flow3" ] )
saveas(fig1,[figName + ".tiff"])


fig1a = figure;   set(fig1a,"Position",[3.1943e+03 143.6667 412
368])%[3.1943e+03 143.6667 412 368])%[2029 148 912 368])
pcolor(axial_De,radial_De,meanSTD);   shading interp;   colormap jet; colorbar
```

```
axis equal;   xlim(xLim);   ylim(yLim);      box off;
ax = gca;   ax.FontSize = 12;   xlabel('X/D','Interpreter','latex');
ylabel('Y/D','Interpreter','latex');
title(["STD, " + nozzle + " , NPR = " + npr],'Interpreter','latex')


figName=([driveOut + nozzle + "_NPR=" + npr + ", STD flow" ] )
saveas(fig1a,[figName + ".tiff"])

fig1a = figure;   set(fig1a,"Position",[3.1943e+03 331.6667 412
180.0000])%[3.1943e+03 143.6667 412 368])%[2029 148 912 368])
pcolor(axial_De,radial_De,meanSTD);   shading interp;   colormap jet;
%colorbar
axis equal;   xlim(xLim);   ylim([0 yLim(2)]);      box off;
ax = gca;   ax.FontSize = 12;   xlabel('X/D','Interpreter','latex');
ylabel('Y/D','Interpreter','latex');
title(["STD, " + nozzle + " , NPR = " + npr],'Interpreter','latex')


figName=([driveOut + nozzle + "_NPR=" + npr + ", STD flow2" ] )
saveas(fig1a,[figName + ".tiff"])

%  set(gcf,'Position',[-1800 500 1100 340]);
%% time history radial location

De_find=-0.5  %------------------------------------<<<<<<<<<<<<<<<<<<

De_find2=0.0  % shock cell wavenumber (centrline)

r=0.25  % tukeywin parameter (0: 0.25: 1 (gaussian) )


% caxis([90 115])
%% Background image
% load('D:\Exp2Saved\41kHz_10us_Background.mat')
% imgMatrixBack = reshape(M_I_back,[X,Y]);

%% organize image matrix per chamber use
%
% chamber=2  % 1-small , 2-large
% % dt=1/41000 %1/211912 %41000
% % Matrix reshape
% imgNos = size(M_I,2);      % Number of images
% imgMatrix = reshape(M_I,[X,Y,imgNos]);  %imgX=reshape(M_x,I,J);
imgY=reshape(M_y,I,J);
% %
% % %Matrix normalize with background
% for i=1:imgNos
% imgMatrix2(:,:,i)=imgMatrix(:,:,i)./imgMatrixBack;
% end
```

```
%%%%%% Normalize image matrix %%%%%%%
for i=1:imgNos
    imgMatrix(:,:,i)=imgMatrix(:,:,i)/ max(max(imgMatrix(:,:,i)));
end

figure; mesh(imgMatrix(:,:,1));shading interp; axis equal
figure; pcolor(axial_De,radial_De,imgMatrix(:,:,1));shading interp
% figure; pcolor(x,y,imgMatrix(:,:,1));shading interp; axis equal


% cut image ????
% cutY1=137;
% cutY2=409;
% cutX1=19;
% cutX2=570;
% %small Chamber pre-cut
% imgMatrix=imgMatrix(cutY1:cutY2,cutX1:cutX2,:);
% imgX=imgX(cutY1:cutY2,cutX1:cutX2);
% imgY=imgY(cutY1:cutY2,cutX1:cutX2);
% [Y X imgNos]=size(imgMatrix)

% Averaging & fluctuating component
imgAvg = mean(imgMatrix,3);     %flucComp = imgMatrix - imgAvg;

[x1 x2 x3]=size(imgMatrix);

% make axial domain Odd numbered pixels

if mod(x2,2)==0
    imgMatrix(:,end,:)=[];

    x(end)=[];
    axial_De(end)=[]
else
end

if mod(x3,2)==0
    imgMatrix(:,:,end)=[];

else
end

imgAvg = mean(imgMatrix,3);     flucComp = imgMatrix;% - imgAvg;

[x1 x2 x3]=size(imgMatrix);


% r=1
winx=tukeywin(x1,r);
winy=tukeywin(x2,r);
```

```
winxy=winy'.*winx;

% figure; mesh(imgAvg.*winxy); shading interp
% imgMaster=imgMatrix;
imgMatrix=imgMatrix.*winxy;

% figure; pcolor(imgMatrix(:,:,1)); shading interp
% figure; mesh(mean(imgMatrix,3)); shading interp
% figure; mesh(flucComp(:,:,1)); shading interp


imgAvg = mean(imgMatrix,3);     flucComp = imgMatrix;% - imgAvg;
imgSTD = std(imgMatrix,0,3);



%%  Time histories
CL=373;



figure; pcolor(axial_De,radial_De,imgMatrix(:,:,1));shading interp; axis equal

% find radial location
Y_loc_in=find(radial_De<De_find+De2/2 & radial_De>De_find-De2/2);

% De2=mean(diff(radial_De))
% Y_loc_in=find(radial_De<De_find+De2/2 & radial_De>De_find-De2/2);

figCo=figure; set(gcf,'Position',[755 217 560 420]);
pcolor(axial_De,radial_De,imgAvg);shading interp
axis equal
h = drawcrosshair('Position',[-6 De_find],'LineWidth',3,'Color','w');
h.StripeColor = 'black';
xlim(xLim)
ylim(yLim)
xlabel('X/De')
ylabel('Y/De')
title(["Mean, " + nozzle + " , NPR = " + npr])


figCo=figure; set(gcf,'Position',[393.6667 81 587.3333 790.6667]);
subplot(211)

pcolor(axial_De,radial_De,imgSTD);shading interp; colormap hot
axis equal
h = drawcrosshair('Position',[-6 De_find],'LineWidth',3,'Color','w');
h.StripeColor = 'black';
xlim([xLim])
ylim(yLim)
xlabel('X/De')
```

```
ylabel('Y/De')
title(["STD, " + nozzle + " , NPR = " + npr])

Meanaxial=imgAvg(Y_loc_in,:);
% figCo=figure; set(gcf,'Position',[755 217 560 420]);
subplot(212)
plot(axial_De,Meanaxial-mean(Meanaxial));shading interp
xlim([xLim])
title(["intensity profile at Y/D = " + De_find ])
xlabel('X/De')
ylabel('normalized intensity')
grid on


figName=([driveOut + nozzle + "_NPR=" + npr + ", STD and shock profile2" ] )
saveas(figCo,[figName + ".tiff"])


timesteps=x3%2000%100
pp_history=mean(imgMatrix(Y_loc_in,:,1:timesteps),1); % mean if Y-loc lip is
more than 1
%     pp_history=mean(dwnstrComp(Y_loc_in,:,1:timesteps),1);
%     pp_history=mean(upstrComp(Y_loc_in,:,1:timesteps),1);
pp_history=permute(pp_history,[3 2 1]); %[3 2 1]
% % % % %      pp_history=pp_history.*hnmask';
%

pp_history_normalized=pp_history;%-mean(pp_history,1); %/max(max(pp_history));
pp_history_normalized=pp_history_normalized/max(max(pp_history_normalized));

figCo=figure;
set(gcf,'Position',[573 299 818.6667 564.6667])
    pcolor(axial_De,(1:
size(pp_history_normalized,1))*dt*1000,abs(pp_history_normalized)); shading
interp
    ylim2=80*dt
    ylim([1 2*80]*dt*1000)
    xlim(xLim)
    xlabel("X/D");  ylabel("t [ms]")
        title(["Time history, " + nozzle + " , NPR = " + npr + " , Y/D = " +
De_find])
        view(0,90)
        colormap gray
        caxis([0.0 0.75])
        % caxis([0.35 1.5])
        % colorbar
                ax=gca; ax.ColorScale='log' ;


figName=([driveOut + nozzle + "_NPR=" + npr + ", time hidtory YD gooood2 = " +
De_find] )
```

```
saveas(figCo,[figName + ".tiff"])


%% Spectral averaging k-f analysis at Y/D = ### new add-on


Ntime=fftwindow %1024*1 %820 %1024*0.25

De_find3=[0 0.25 0.5 1 ]'
% De_find3=[-1 -.75 -.5 -0.25 ]'

[tes1 Y_loc_in3]=find(radial_De<De_find3+De2/2 & radial_De>De_find3-De2/2)


% frequency range:
Fs=1/dt
Fr=Fs/Ntime
ffi=-Fs/2:Fr:Fs/2-Fr;

% wavenumber range:
% dx=(imgY(1,2)-imgY(1,1))/De
npts=size(flucComp,2)
f=fftfreq(npts,(dx/De)/(2*pi));

f1=fftshift(f);

% Blocking
Ntime
Cyc=1
Rov=nOvlp %0.75 % Overlap 25%
k_count=floor((size(flucComp,3)-Rov*Ntime*Cyc)/((1-Rov)*Ntime*Cyc))
hn=hann(Ntime*Cyc);      % applying hanning window temporal

onesize=ones(size(flucComp,[1 2]));

clear hn_time R_c2 GRR mGRR
for h=1:length(hn)
    hn_time(:,:,h)=onesize*hn(h);
end


hn_w=hn_time(Y_loc_in3,:,:);
hn_w=permute(hn_w,[2 3 1]);
% figure;mesh(hn_w)
n=Ntime;


% rp1=flucComp(Y_loc_in3,:,:);
rp1=flucComp(:,:,:);
rp1=permute(rp1,[2 3 1]);
rp1m=mean(rp1,1);
```

```
% rp1=rp1-rp1m;
% figure;plot(rp1(:,10))

clear R_c2 R_c3


R_c2=zeros(size(rp1,1),n);
R_c3=R_c2;

for c=1:k_count  % number of measurments r
    index=(c-1)*(1-Rov)*Ntime*Cyc+1:c*(1-Rov)*Ntime*Cyc+Rov*Ntime*Cyc;

    rp2=rp1(:,index,:);%.*hn_w;%.*hn_time;
    for rr=1:Cyc
        index2=(rr-1)*Ntime+1:rr*Ntime;
        %         Y2=abs(fftn(rp2(:,index2)))/(Ntime*Cyc);
        %         Y2=Y2.^2;   R_c2(:,:,c)=Y2;
        % Y2=abs(fft2(rp2(:,index2,:)));
        Y2=(fft2(rp2(:,index2,:)));
        Y2abs=abs(Y2);

        R_c2=Y2abs.^2 + R_c2;
        R_c3=Y2 ; %+ R_c3;

    end
end

% R_c2=mean(R_c2,3);
%     PSD=(1/Fr)*R_c2;
%         spectra=10*log10(((2*Fr)/(Pref^2))*PSD);


R_c2=R_c2/(Fs*Ntime*Cyc*k_count);
R_c3=R_c3/(Fs*Ntime*Cyc*k_count);

% Pref=10^-6;
Pref=mean(R_c2,3);
Pref=mean(Pref,1);
Pref=std(Pref,0)

spectra=10*log10( (Fr*R_c2) / (Pref^2) );   %%%%%%

   spectra =permute(spectra,[3 1 2]);

    spectra=fftshift(spectra,3);
spectra=fftshift(spectra,2);

spectra=fliplr(spectra);
size(spectra)

%
```

```
spectra2 =permute(R_c3,[3 1 2]);

    spectra2=fftshift(spectra2,3);
spectra2=fftshift(spectra2,2);

spectra2=fliplr(spectra2);
size(spectra2)


%^^^^^^^^^^^^^^^^^

freqtable={[1500 1800 2000 3000 4000 7550 8150 8600 9600 10300 11300 13300
15750 20750 25250 27050 28950];
[1500 1800 2000 3000 3900 4000 5900 6000 7300 7900 8100 8500 10000 11300 13800
20000 24300 25800 ];
[1500 1800 2000 3000 3800 4000  4500 5100 5350 5850 6550 6900 7750 8600 10150
13650 18650 21550 23300 ]}
```